POLITECNICO DI TORINO
Corso di Laurea in Ingegneria Energetica e Nucleare

Tesi di Laurea Magistrale

Numerical simulation of PCM-based storage units to be integrated into commercial hot water storage tanks

Relatori
Prof. Eliodoro Chiavazzo
Ing. Luigi Mongibello

Candidato
Manfredi Neri

Anno Accademico 2018/2019

Abstract

In future energy systems, storage will have a primary role, allowing smaller generation units and a separation of the energy production from the consumption. What is more for intermittent renewable energy sources such as solar and wind, storage is strictly necessary. The cost of electrical batteries is still very high, so one of the preferred storage technologies is the thermal one. In fact, thermal energy is used both as it is and as a source to be converted into other forms. Thermal energy storage can increase the efficiency of industrial plants by exploiting waste heat and the efficiency of co-generation plants by making the generation independent from the demand curve. Among thermal energy storage, phase change materials (PCM) represent an opportunity thanks to their large latent heat that can reduce the size of storages. The main purpose of this thesis is the modelling of phase change material units macro-encapsulated in commercial hot water storage tanks. These hybrid PCM-water systems are studied mostly for the possibility of enhancing the thermal capacity of a water tank storage by integrating it with PCM. The thesis starts with a literature review about the different phase change materials for latent heat storage applications and the numerical methods to model them. These methods are tested by launching different simulations of a study case on Comsol. The numerical results are compared to each others and to the experimental results in order to verify which of the methods better models the real case. The best one is then used to model the charge and discharge of a PCM unit in a climatic chamber. The results are then compared with the experimental ones to validate the model and a study on the effects of the different empirical parameters on the solution is done. The water tank storage is firstly modelled on Matlab to simulate its behaviour without the PCM. After the model has been tested, it has been coupled with the one simulating the single modules of PCM. Therefore a third model that simulates the whole PCM-water storage is obtained and has been validated experimentally.

Contents

List of Tables

List of Figures

Chapter 1

Introduction

It is well-known the importance of renewable energy sources and their contribute to reduce greenhouse emissions. However, due to their highly variable and unpredictable behaviour, especially solar and wind energy sources should be coupled with storage technologies. In the case of solar power, storage technologies allow to mismatch the energy production from its consumption. In this way the excess of solar energy produced during the day can be stored and used during the night. What is more, storage technologies can also be projected to let save money to the consumers, by buying energy and storing it when the general demand is low and the cost as well. This energy is then reused or sold during the demand peaks, when it usually costs more. Storage technologies are grouped into: mechanical, electrical, chemical and thermal energy storages. At the moment there is a strong interest in thermal storage, since it is applicable to all scales. It is very common in residential applications like heating, cooling, air conditioning and domestic hot water. Furthermore, large tanks containing molten salts at temperature varying between 200°C and 560° C are often installed in concentrated solar power plants, being one of the keys of the success of this technology. Thermal storage technologies are divided into sensible heat thermal energy storage (SHTES) , latent heat thermal energy storage (LHTES) and thermochemical energy storage. The sensible heat is stored thanks to the variation of energy due to a temperature difference in the storage material, which usually is either liquid or solid. Packed beds of rocks are widely used for sensible thermal storage when the heat fluid is air, because the high thermal conductivity of the rocks is needed to balance the poor thermal properties of air. In most of the other applications hot water storage is preferred because of its larger specific heat. Latent heat storage includes a portion of sensible heat, but the rest is represented by heat stored at a constant or quasi-constant temperature thanks to the latent heat coming from a phase change.

This thesis work is about numerical modelling of phase change materials for latent heat thermal energy storage. It includes also the experimental validation of the results. The whole work has been carried on in collaboration with the ENEA research center of Portici. The second chapter is an introduction to the different technologies of latent heat thermal energy storage. It provides a classification of the various types of phase change materials and explains their main advantages, the weak points and the possible techniques to overcome the most common problems, such as subcooling, segregation and low thermal conductivity. In fact, in order to be interesting, PCM should have kinetic, chemical and economical requirements. The chapter includes also a classification of the different materials and lists their characteristics. Chapter 3 is a literature review on the numerical methods that model phase transition. It starts with the Stefan's mathematical formulation of solid-liquid phase change, however the analytical solution exists only for very simple cases, so the chapter continues with a description of the different numerical methods commonly implemented to approximate phase change. They are classified in: fixed grid and variable grid

methods. The firsts use an enthalpy formulation of the phase change, considering a non-isothermal release of the latent heat, but assuming the presence of a "mushy zone". The variable grid methods do not change the Stefan problem assumption of isothermal phase change, but track the interface at every time instant. One method largely implemented with this intent and mentioned in the thesis, is the arbitrary Lagrangian-Eulerian. A sort of hybrid method, called phase field method is also described. This method tracks the interface, but it does not change necessarily the grid. What is more it is based on a modified Stefan condition, in which the interface is not isothermal and is characterized by a finite thickness. The chapter ends with a brief analysis of the numerical models for packed beds of PCM spheres. They are mainly classified in four groups: single phase , Schuman models, concentric dispersions models and continuous solid phase models. Chapter 4 is a case study based on an article about the numerical modelling and experimental validation of a phase change material with a melting temperature of about $15°C$, hence used for cooling energy storage. The experiment was conducted with a climatic chamber and included both charge and discharge, while the simulations were launched using the apparent heat capacity method. Following the procedure of the paper, three other methods are tested, using the FEM software "Comsol Multiphysics" and the results are compared with the experimental data, provided by the author of the paper. Two of these methods are implemented with a fixed grid, but the main difference between them is the way velocity in solid cells is forced to zero. The third method is an arbitrary Lagrangian-Eulerian, in which the phase transition interface is assumed to have a zero thickness and a homogeneous temperature. The implementation of this method required some numerical artifices, because it does not allow topology changes to the geometry, but it is only able to model its deformation. The results obtained with the three methods are then compared with the experimental data and the one that provided the best accuracy, is the enthalpy porosity method with the apparent viscosity. Finally, the results obtained from the different models are compared to each others, by plotting on the same graph the curves relative to the total energy stored and released during the charge and discharge. Chapter 5 presents the experiment, conducted with a phase change material with a melting temperature of 68 $°C$. It is performed in the thermal energy storage laboratory of the ENEA research center of Portici. This material stayed in a climatic chamber for more than 70 hours, completing a full cycle of charge-discharge and two thermocouples measured the temperature of the air and inside the PCM. The measures are transferred in real-time to a laptop through a LabVIEW application and saved in a csv file. A Differential scanning calorimetry analysis of the material has also been conducted, in order to obtain the accurate values of melting and solidification temperatures. Finally, the enthalpy porosity method, already implemented in chapter 4 is used to model the behaviour. Chapter 6 presents the numerical results and the comparison with the experimental data through plots and statistical analysis. Chapter 7 is dedicated to the modelling of water tanks for thermal storage: firstly model of a tank with an immersed coil is studied thanks also to previous works present in literature, while in the second part of the chapter it is presented the model for a tank with two separate immersed coils for charge and discharge. Both models are built by means of Matlab and can be coupled with the PCM model in chapter 5 to simulate the behaviour of encapsulated PCM inside water tanks for thermal energy storage applications. In Chapter 8 in fact, a study is done on the performance of a hybrid PCM-water thermal storage, characterised by a water tank integrated with PCM modules. The model implemented by coupling the tank and the PCM models is validated with the experimental results. All the conclusions and the prospective studies that will follow to this thesis are presented in Chapter 9.

Chapter 2

Latent heat thermal storage

2.1 Introduction

Phase transition can be solid-solid(variation of the crystalline structure), liquid-gas and solid-liquid. In general in storage applications the solid-liquid phase change is the most suitable, since it offers the best latent heat per unit of volume and little density variations. One common application is the ice storage used for cooling needs. The material used for latent heat storage are called phase change materials (PCM). Latent heat storage is interesting in all the cases where the available temperature difference is not very large. In fact the presence of a latent heat share allows smaller storage sizes if compared to SHTES .

2.2 Properties of PCM

Different PCMs are studied for many temperature ranges (Fig. 2.1). Water, aqueous salt solutions have low melting temperatures, as a consequence they can be used for cooling applications, while paraffins, salt hydrates and fatty acids change phase at medium temperatures, so they can be used for domestic heating where the required temperature is below 100 $°C$. Finally, fluorides, chlorides and carbonades have large latent heat and high melting points, which make them be applicable in high temperatures applications, such as concentrated solar power. In order to be attractive, PCMs should satisfy some requirements under the thermal, physical, kinetic and chemical point of view [4].

Thermophysical requirements

- Suitable phase change temperature
- High value of latent heat
- High value of specific heat
- Good thermal conductivity
- Absence of segregation during phase transition
- Little volume changes during phase change

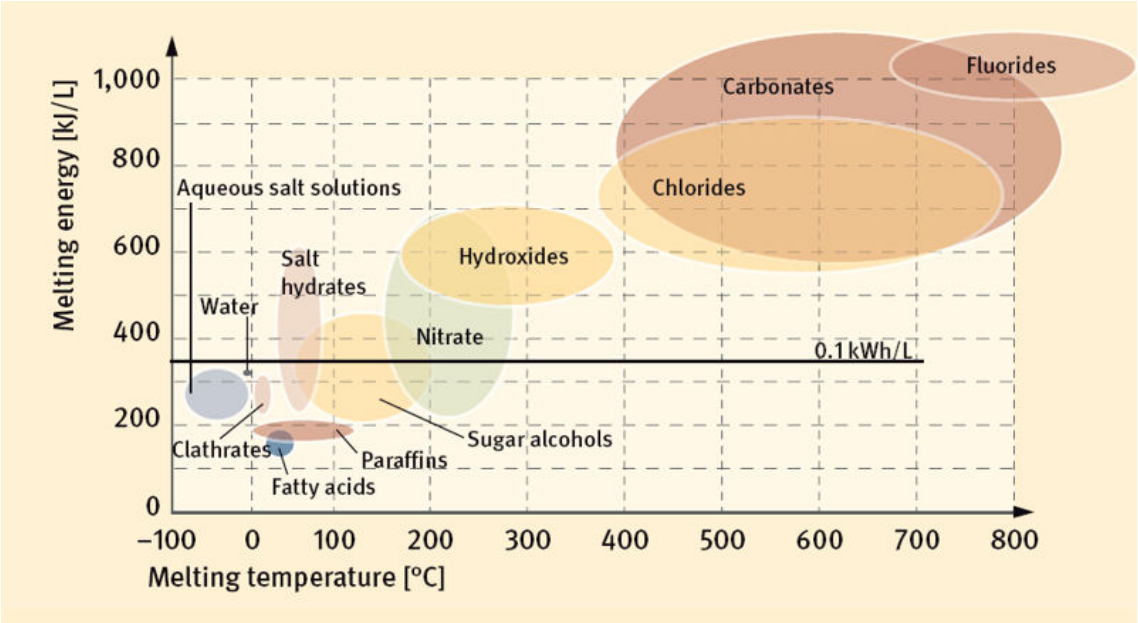

Figure 2.1. Melting temperature and latent heat for different classes of PCMs. [ZAE Bayern]

Larger values of specific and latent heat reduce the volume and mass of the storage, while a better conductivity increases the thermal power that the storage can absorb or release. The phase change temperature is an important parameter, since it should be as close as possible to the temperature of the specific application. Regarding the presence of phase segregation during solidification, it can decrease the life-cycle of the storage, therefore it is preferred to avoid this phenomenon.

Kinetic requirements

- Limited supercooling
- Sufficient nucleation velocity

Supercooling is the phenomenon occurring when the temperature of the liquid goes below the freezing point, without crystallizing. It should be avoided because it makes the discharge process much slower. It is a common problem in salt hydrates and depends on the nucleation rate.

Chemical requirements

- Long term chemical stability
- No toxicity
- No fire-hazard
- No corrosiveness

Economical requirements

- Easily accessible
- Low cost

Unfortunately a material with all these properties does not exist, but there is a trade-off to consider on a case-by-case basis. Depending on the application some of these requirements are prioritized and for the others some adjustments have to be considered in the project of the storage. As an example metallic fins can be used to partially solve the problem of low conductivities of most commercial phase change materials or nucleating agents can be introduced to accelerate the crystallization.

2.3 PCM classification

Phase change materials are classified into three main groups depending on the nature of the material. These categories are: organic, inorganic and eutectics.

2.3.1 Organic PCM

Organic phase change materials can be either paraffins or non-paraffins. They have good kinetic and chemical properties, since they can freeze and melt multiple times without segregation and usually they do not to supercool.

Paraffins

Paraffins are waxes whose chemical structure is characterised by alkane chains $CH_3-(CH_2)_nCH_3$, where the latent heat and the melting point depend on the length of the chain. Commercial paraffins are one of the most common PCM in LTHES applications thanks to their moderate cost, availability, and large values of latent heat. What is more they are chemically stable under $500°C$ [5] and are not affected by segregation. Their main disadvantages are the flammability, low thermal conductivity and corrosiveness against plastic, which leads to higher costs of containment cases.

Non- paraffins

Organic non-paraffins used for latent heat storage can be fatty acids, esters, alcohols or glycols. Some of the characteristics of these materials are: large heat of fusion, toxicity, absence of segregation, almost no deterioration with cycling, no supercooling and low thermal conductivity. Fatty acids represent the alternative to paraffins thanks to their larger heat of fusion, on the other hand, they are twice more expensive. Their general formula is $CH_3(CH2)_2n \cdot COOH$. [5]

2.3.2 Inorganic PCM

Inorganic phase change materials can be either salt hydrates or metallics.

Salt hydrates

Some salts can combine with water and form a unique molecule, whose chemical formula is $M \cdot nH_2O$. Salt hydrates can melt in two ways: by forming a hydrate with less moles of water (2.1) or by completely dehydrating and forming the anhydrous form (2.2)

$$M \cdot nH_2O \rightarrow M \cdot m(H_2O) + (n-m)H_2O \tag{2.1}$$

$$M \cdot nH_2O \rightarrow M + nH_2O \tag{2.2}$$

Usually salt hydrates have large latent heat per unit of volume, good thermal conductivity and are subjected to small density variations. Moreover, they are economically sustainable and not

corrosive. On the other hand, they usually have an incongruent melting behaviour, caused by over-saturation of water at the phase change temperature, especially when a lower hydrate is formed. In this way the solid salt settles on the bottom of the recipient and does not recombine with water molecules during solidification. Hence the process of solidification-melting is characterized by a strong irreversibility, which causes a continuous reduction of salt hydrates, that means a decrease of the latent heat after every charge-discharge cycle. This problem can be partially solved by the following remedies:

- adding water to the solution to prevent its over-saturation;
- using encapsulated PCM to avoid the settling of solute on the bottom of the recipient;
- stirring the solution to prevent the permanent attachment of solute to the bottom of the recipient;
- using polymers to increase the viscosity of the solution reduces the phase separation.

Another disadvantage of these materials is the slow nucleation rate, which causes supercooling. This phenomenon occurs when the temperature of the liquid phase goes below the freezing point. It is not desirable, mainly because it makes the discharge process slower. This difficulty can be managed by adding some nucleating agents that act as initial nuclei. In this way the crystallization rate can be sensibly accelerated, resulting in a reduction of supercooling.

Metallics

Metallic phase change materials are rarely used for storage applications, due to their lower specific heat. However, if weight is not an issue they are interesting in terms of latent heat per unit of volume. What is more they have excellent thermal conductivity and some of them have high melting temperature that can make them suitable for storage in CSP. Sandia National Laboratories are developing a Stirling dish coupled with a storage made of metallic PCM. In particular, CuMgSi seems to be the one of the best options thanks to its high point of fusion and latent heat [6].

2.3.3 Eutectics

Eutectics are organic-organic, organic-inorganic or inorganic-inorganic mixtures at minimum- melting composition (Point E in Fig 2.3.3). Usually they freeze and melt congruently without segregating, therefore their storage properties do not deteriorate with cycling.

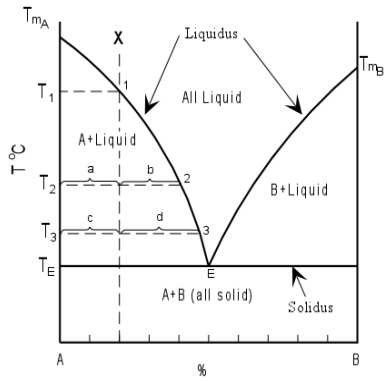

Figure 2.2. Phase diagram of eutectic mixture

2.4 Thermal improvements

One of the problems of PCMs, especially the paraffins, is the poor thermal conductivity, that weakens the heat transfer. Heat transfer ratio can be increased by either enhancing the heat exchange surface or by increasing the thermal conductivity of the storage unit. A common solution to the poor thermal conductivity consists in inserting the paraffin into metallic porous matrices. Aluminium and graphite have large conductivity, so they are used at this scope, but at the same time they reduce the volumetric heat release and makes the whole system heavier. Another possibility relies in dispersing small particles of these materials in the PCM or to produce composite materials. Concerning heat transfer surface, it can be enhanced by using finned tubes, as shown in Fig. 2.3.

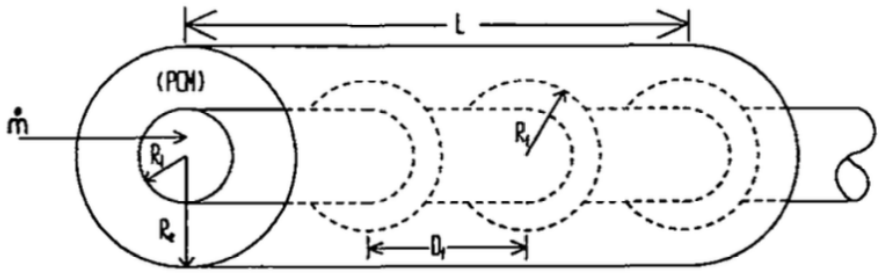

Figure 2.3. Latent heat storage unit with fins in the PCM side to increase heat transfer surface. [1]

Another popular solution is increasing the heat transfer area by using encapsulated PCM. According to the size, encapsulated PCM can be classified in : macro-encapsulated (>1 mm), micro-encapsulated(0.1 μm-1 mm) and nano-encapsulated(<0.1 μm). Macro-capsules contain significant amount of PCM and their shape can be cylindrical tubes, spheres or plates [7]. Microcapsules are spheres of PCM surrounded by a shell with a thickness that varies between 0.5 and 150 μm, usually made in metal or polymers such as PMMA or PEMA [8]. Nano-capsule have a huge potential, but they are still studied and actually available only at laboratory scale. The main advantage of encapsulation is the increase of heat transfer area, but it provides also secondary improvements such as:

- preventing the mixing of the heat transfer fluid with the fluid phase of the PCM;
- avoiding phase segregation;
- increased compatibility in case of corrosiveness or flammability of the PCM.

The thermal advantages of encapsulation can be even improved by using stratified packed bed of PCM with different melting temperature (Fig. 2.4). Thus, in single PCM storage units, the temperature gradient close to the phase change region is close to zero, which affects the heat transfer, while with stratified PCMs the thermal gradient increases and so does the heat transfer ratio. What is more they are also characterized by less irreversibility, which leads to faster charge/discharge and higher exergy efficiency. [2]. On the other hand, the optimization of these systems can be quite hard, since it is necessary to find the optimal melting temperatures, choose the PCMs and optimize the quantity for each of them.

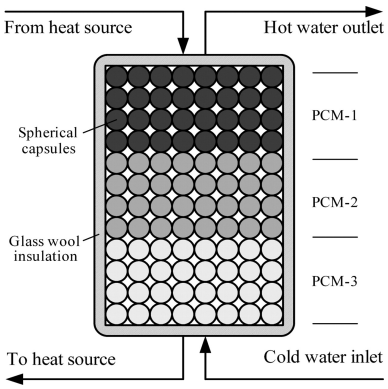

Figure 2.4. Stratified PCM packed bed [2]

Chapter 3

PCM modelling

3.1 The Stefan problem

In 1889 Josef Stefan formulated a class of 1D models for heat transfer applications with phase transitions [9]. In particular, he studied the freezing of water, but these models are applicable to almost any phase change material. The assumptions are zero-thickness of the solid-liquid interface, absence of supercooling and segregation. Moreover, diffusion is assumed to be the prevalent heat transfer mode in the liquid phase. As a consequence, the convective heat transfer is neglected and the temperature profile at the interface can be considered continuous. The simplest model of this kind, which admits an exact solution, is characterized by the presence of a semi-infinite conducting material that occupies the space $0 < x < \infty$ as shown in Figure 3.1. Here it is explained how the solidification model works, but the same is applicable to melting. At the initial time t=0 the domain is liquid at the uniform temperature $T_i > T_m$. At x=0 a Dirichlet boundary condition is applied: the material is kept constantly at the temperature $T_1 < T_m$, which causes the solidification of the semi-infinite domain. Therefore, the nterface is initially at x=0, but as the material solidifies, it moves to right. The model is described by the following system of equations for the solid and liquid phase and the interface.

Solid:

$$\begin{cases} \rho_s c_s \dfrac{\partial T_s}{\partial t} = \dfrac{\partial}{\partial x}(k_s \dfrac{\partial T_s}{\partial x}); \qquad x < s(t),\ t > 0 & (3.1) \\ T_s = T_1; \qquad x = 0, t > 0 & (3.2) \end{cases}$$

Liquid:

$$\begin{cases} \rho_l c_l \dfrac{\partial T_l}{\partial t} = \dfrac{\partial}{\partial x}(k_l \dfrac{\partial T_l}{\partial x}); \qquad x > s(t),\ t > 0 & (3.3) \\ \dfrac{\partial T_l}{\partial x} = 0 \qquad x \to \infty,\ t > 0 & (3.4) \\ T_l = T_i \qquad x > 0,\ t = 0 & (3.5) \end{cases}$$

Interface:

$$\rho L \frac{ds}{dt} = k_s \frac{\partial T_s}{\partial x} - k_l \frac{\partial T_l}{\partial x} \qquad x = s(t),\ t > 0 \tag{3.6}$$

Where L is the latent heat per unit of volume, k_s and k_l are the conductivities of solid and liquid phases, s(t) is the position of the interface,which moves continuously to the right as the freezing process goes on. The assumption of no-convection is related to the fact that the velocity of the liquid phase could be neglected, however it is still a strong hypothesis due to the low values of heat conductivity that phase change materials usually have.

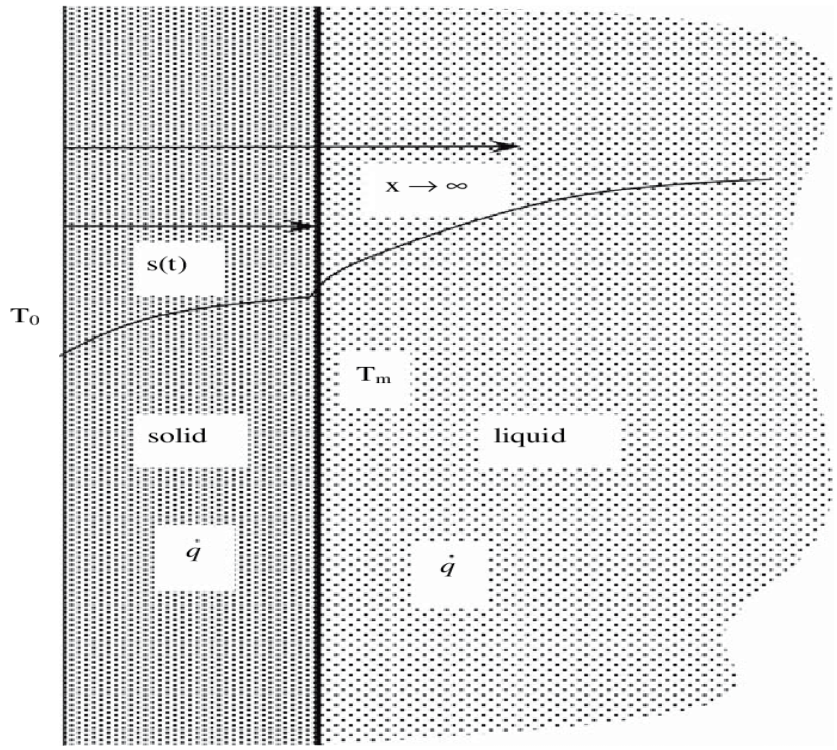

Figure 3.1. Schematic of semi-infinite slab, characterized by the moving interface between the two phases [3].

3.1.1 Analytical solution

Stefan problems can be solved with either analytical or numerical models. Exact analytical and approximated analytical methods are mostly limited to one dimensional situations and simple boundary conditions. In the case of a semi-infinite domain $0 < x < \infty$ initially in the liquid phase at $T_i > T_m$ and the Dirichlet boundary condition $T(x = 0, t > 0) = T_1$, with $T_1 < T_m$ the exact analytical solution is available and the procedure is shown below [10]. The general time law for the interface can be written as:

$$s(t) = 2\lambda\sqrt{\alpha_l t} \tag{3.7}$$

Where α_l is the liquid diffusivity and λ is the parameter that needs to be found in order to evaluate the time law of the interface.
The temperature profiles in solid and liquid phases can be written as:

$$T_s = T_1 + A \cdot erf(\frac{x}{2\sqrt{\alpha_s t}}) \tag{3.8}$$

$$T_l = T_i + B \cdot erfc(\frac{x}{2\sqrt{\alpha_l t}}) \tag{3.9}$$

Where erf and $erfc$ are respectively the error and complementary error functions. A and B are the constants that need to be found to solve the temperature profiles. Applying the condition of

temperature continuity at the interface, the following relations are obtained :

$$A = \frac{T_f - T1}{erf(\lambda)} \tag{3.10}$$

$$B = \frac{T_f - T_1}{erfc(\lambda\sqrt{\alpha_s/\alpha_l})} \tag{3.11}$$

Substituting the temperature profiles in the interface equation (3.6) leads to the transcendental equation, which requires an numerical non-linear method to be solved.

$$\frac{e^{-\lambda^2}}{erf(\lambda)} + \frac{k_l}{k_s}\sqrt{\frac{\alpha_s}{\alpha_l}}\frac{e^{-\lambda^2\frac{\alpha_s}{\alpha_l}}}{erfc(\lambda\sqrt{\frac{\alpha_s}{\alpha_l}})}\frac{T_f - T_i}{T_f - T_1} = \frac{\lambda L\sqrt{\pi}}{c_s(T_f - T_1)} \tag{3.12}$$

In the case of finite domain, the problem is much more complex and the exact solution does not exist, so the method used is an approximate one, which leads to the writing of a non-linear system of two equations and two unknowns.

3.2 Numerical methods

Solving the Stefan problem is difficult due to the non-linearity at the moving interface and the different thermophysical properties of the two phases, which cause discontinuities. Numerical methods can be a powerful tool to solve the moving-boundary problem even in the presence of strong convection, which was instead neglected in Stefan problems.[5] The main approaches used to model numerically phase change problems are the front-tracking methods and the fixed-grid methods [11]. The firsts offer better accuracy, but they are difficult to implement and, therefore, limited to simple applications and geometries. Their principle is to solve the governing equations at each time step by first evaluating the position of the moving interface. The seconds do not offer the information on the precise position of the moving boundary, but are faster and easier to implement.

3.2.1 Front-tracking methods

Three examples of front-tracking methods successfully employed to solve Stefan problem in plane geometry are the boundary immobilization method (BIM), the nodal integral method (NIM) and the variable space grid-method(VSGM). [12]. In the BIM and NIM the front is tracked at each time step, but the domain of the problem is transformed into a fix one, reducing the difficulties related to handling the moving interface. The BIM uses a finite difference approach, while NIM uses FEM. The VSGM is different from the other two methods, since the domain is not transformed into a fixed one. At each time step the moving boundary is fixed at the last point of the grid, by increasing the space width interval as the phase change process goes on.[13] In the case of melting of a half plane at an initial temperature equal to the one of phase change and a Dirichlet boundary condition $T(x = 0, t > 0) = T_1$, with $T_1 > T_m$, the procedure of BIM is [14]:

The domain transformation gives:

$$x^* = \frac{x}{s}, \quad T^*(x^*, t) = T(x, t) \tag{3.13}$$

The governing equations (3.4) and(3.6) in the solid and interface can be transformed into one in the fixed domain: $0 < x^* < 1$:

$$s^2\frac{\partial T^*}{\partial t} = \frac{\partial^2 T^*}{\partial x^{*2}} + x^* s\frac{ds}{dt}\frac{\partial T^*}{\partial x^*} \tag{3.14}$$

The boundary conditions are written as:

$$T^*(x^* = 0, t) = T_1, T^*(x = 1, t) = 0, \tag{3.15}$$

$$s\frac{ds}{dt} = -St\frac{\partial T^*}{\partial x^*}; \qquad x^* = 1 \tag{3.16}$$

Where the $St = \rho c_s \frac{T_m - T_1}{L}$ is the Stefan number. The central finite difference discretization of eq. (3.14) implicit in T^* and explicit in s is:

$$a_i^{(k+1)} T_{i-1}^{(k+1)} + b_i^{(k+1)} T_i^{(k+1)} + c_i^{(k+1)} T_{i+1}^{(k+1)} = (s^{(k)})^2 T_i^{(k)} \tag{3.17}$$

where

$$a_i^{(n+1)} = \frac{\Delta t}{(\Delta x)^2}\left[\frac{\Delta x}{2} x_i s^{(k)} \left(\frac{ds}{dt}\right)^{(k)} - 1\right] \tag{3.18}$$

$$b_i^{n+1} = (s^n + 2\frac{\Delta t}{(\Delta x)^2}) \tag{3.19}$$

$$c_i^{n+1} = -a_i^{k+1} - 2\frac{\Delta t}{(\Delta x)^2} \tag{3.20}$$

$$\left(\frac{ds}{dt}\right) = \frac{St}{s^{(n)}}\left(4T_{N-1}^{(n)} - T_{N-2}^{(n)}\right) \tag{3.21}$$

The temperature profile at each time step is calculated by solving eq. (3.17) and the position s of the moving interface is updated the following explicit equation:

$$s^{n+1} = s^n + \left(\frac{ds}{dt}\right)^{(n)} \Delta t \tag{3.22}$$

where the subscript i refers to the nodal point i, while $i+1$ and $i-1$ are its left and right neighbours, the upscripts $n+1$ and n respectively refer to the actual time-level and the old one. N is the last node of the modified grid,which corresponds to the interface, so $N-1$ and $N-1$ are the two previous nodes. This procedure is written for the simple case of one-phase Stefan Problem, but in the full article written by Crank [15] it is implemented also for the most general case with two phases. However ,the transformation of the domain causes a singularity at the first time step, when the phase change front is in the origin. For the semi-infinite wall the available exact analytical solution can be used as starting time law of the interface. On the other hand, in the case of more complex geometries, the exact solution does not exist and an approximate one is needed.

Arbitrary Lagrangian Eulerian method

In commercial softwares like Comsol or Ansys it is possible to use method that allow geometries to deform during a transient. As a consequence, these methods can be implemented to model solidification or melting if both phases exist at the initial time t=0 [16]. The whole geometry is, in fact, divided in two domains: a solid and a liquid one and as the PCM solidifies or melts these domains deform, due to a moving boundary that separates them. If volume variations are not taken into account, zero normal displacements are assigned to the outer boundaries, while the normal velocity of the moving boundary is computed according to the Stefan condition:

$$v_{n,\Omega} = (q_l - q_s)/(L * \rho) \tag{3.23}$$

where the subscript Ω refers tothe moving boundary, n stands for normal component, while q_l and q_s are respectively the heat fluxes through the internal boundary from the liquid ans solid domains.

The assigned displacements and the velocity of the interface are used to define deformations. The deformation can be computed by four smoothing approaches: Laplace,Winslow, Hyperelastic and Yeoh. The Laplace smoothing approach solves the following differential equation :

$$\frac{\partial^2 x}{\partial X^2} + \frac{\partial^2 y}{\partial Y^2} + \frac{\partial^2 z}{\partial Z^2} = 0 \tag{3.24}$$

where x, y and z are the deformed coordinates of the mesh, while X, Y and Z are the undeformed coordinates. Eulerian description does not allow to handle moving boundaries, because physical quantities are referred to fixed points in space. As a consequence an arbitrary Lagrangian Eulerian method shall be used in these situations. In fact, it allows to define two different coordinate system for the mesh and the space. In mesh coordinate system the domain boundaries are fixed and a map converts the mesh coordinates to spatial ones. Initially these systems of coordinates coincide, but as the domain starts to deform, the mesh coordinate system changes. The map from mesh to spatial coordinates can become ill-conditioned if the mesh is highly deformed, so in order to avoid numerical stability problems a proper remeshing is needed. When a certain condition is reached the mesh is rebuilt and the simulations is momentarily stopped. Two examples of condition for the remeshing could be the distortion of the mesh that reaches a relative large value or the quality of the mesh that becomes too small. After the remeshing, the new mesh coordinate system coincides again with the spatial system [17].

3.2.2 Fixed grid methods

In fixed grid methods it is assumed that the phase change does not occur at a zero-thickness front, instead a mushy zone is defined. This simplifies the problem, since the mushy zone between the phases deletes the discontinuities caused by the presence of the interface. In conduction/diffusion prevalent phase change, the energy equation can be written as follows [18]:

$$\frac{\partial H}{\partial t} = \nabla\Big(k\nabla T\Big) \tag{3.25}$$

where k is the conductivity and H is the total volumetric enthalpy defined as a sum of the contributions given by sensible and latent heat.:

$$H = h_0 + \int_{T_0}^{T} \rho c \, dT + fL \tag{3.26}$$

f is the fraction of liquid, defined with a piecewise function, which in the case of isothermal phase change is written as follows:

$$f = \begin{cases} 0 & T < T_m \\ ]0,1[& T = T_m \\ 1 & T > T_m \end{cases} \tag{3.27}$$

Fixed grid methods are then divided in three classes: source based, apparent heat capacity and enthalpy methods.

Enthalpy method

In the enthalpy method the temperature is solved indirectly, by first evaluating the enthalpy at each time-step. With Finite-Volumes eq. (3.25) is discretized as follows [19]:

$$H_p^{n+1} = H_p^n + \sum_{nb} a_{nb} T_{nb}^{n+1} + a_p T_p^{n+1} \tag{3.28}$$

where a's are the discretization coefficients, the subscripts p and nb refer to the node point p and to its neighbours, the upscripts $n+1$ and n, respectively refer to the actual and old time-steps. The equation (3.28) is therefore coupled with a temperature function of enthalpy, opportunely smoothed if the phase change is isothermal, in order to avoid discontinuities, such as eq. (3.29). As a consequence, the system is non-linear, since the enthalpy H_p^{n+1} depends on the temperature T_p^{n+1},so it should be solved with iterative algorithms, such as the Newton ones.

$$T_p = \begin{cases} H_p/C_s & T \leq T_m - \Delta T \\ \frac{H_p + [\frac{C_l - C_s}{2} + \frac{L}{2\Delta T}](T_m - \Delta T)}{\frac{C_l - C_s}{2} + \frac{L}{2\Delta T}} & T_m - \Delta T < T < T_m + \Delta T \\ \frac{H_p - (C_s - C_l)T_m - L}{C_l} & T \geq T_m \end{cases} \tag{3.29}$$

where ΔT is half of the phase change temperature interval. Enthalpy method is difficult to implement due to the non-linearity of the (3.28), but it is more stable than the others. [20, 21].

Source based method

In source based methods the latent heat release is considered as a heat source, so under the assumption of constant thermophysical properties eq. (4.1) can be rewritten as:

$$\rho c \frac{\partial T}{\partial t} = k\nabla^2 T - L\frac{\partial f}{\partial t} \tag{3.30}$$

When it is discretized with finite volumes method, it becomes [22]:

$$[a_p + (\rho cV)_p]T_p^{m+1} = (\rho cV)_p T_p^m + \sum_{nb} a_{nb} T_{nb}^{m+1} + (\rho LV)_p [f_p^{old} - f_p^m] \tag{3.31}$$

where the subscripts p and nb refer to the node point p and its neighbours, a_p,a_{nb} are the relative discretization coefficients, V is the volume of the cell associated to the node p and the upscripts m and *old* respectively refer to the actual and iteration level and to the previous time-step. So ,at each time-step, the temperature field is calculated iteratively and after each iteration the liquid fraction is updated as follows:

$$f_p^{m+1} = f_p^m + \lambda\Delta \tag{3.32}$$

where λ is an under-relaxation factor and Δ is a correction term. After the liquid fraction is updated an undershoot/overshoot correction is applied to it in order restrict the possible values in the range [0,1]. When convergence is reached, the same iterative calculation starts for the next time step, starting from $f_p^0 = f_p^{old}$. [23]. Different authors implemented many ways of calculating the correction term. As an example Cross et al proposed to calculate it directly from the liquid fraction function of temperature [24]:

$$\Delta = F(T_p^{m+1}) - f_p^m \tag{3.33}$$

where F(T) is the liquid fraction function of temperature, which can have many shapes, but in the case of isothermal phase change, it should be approximated and smoothed to avoid discontinuities, similarly to the enthalpy method. The main difficulty linked to this method is finding the optimal value of the under-relaxation parameter.

Apparent heat capacity method

In apparent heat capacity method, eq. (4.1) is instead rewritten as:

$$C_{app}\frac{\partial T}{\partial t} = \nabla[k\nabla T] \tag{3.34}$$

where C_{app} is the apparent heat capacity of the phase-change material, defined as the time derivative of total volumetric enthalpy :

$$C_{app} = \frac{\partial H}{\partial T} = C(T) + L * \delta(T - T_m) \tag{3.35}$$

where δ is the Dirac-delta and represents the temperature derivative of the liquid fraction. Bonacina et al. [25] showed that it is possible to get rid of the difficulties related to the presence of the Dirac function, by replacing it with a smoothed one, which assumes finite values larger than zero in the interval $T_m - \Delta T < T < T_m + \Delta T$. Where ΔT, as in the enthalpy method, represents half of the mushy zone temperature range. When it tends to zero, the solution of the smoothed problem tends to the original one. On the other hand, under a numerical point of view, it should not be too small, otherwise it leads to convergence errors. Approximated heat capacity is defined as:

$$C^*(T) = \begin{cases} C_s(T), & T < T_m - \Delta T \\ C_l(T), & T > T_m + \Delta T \end{cases} \tag{3.36}$$

While for $T_m - \Delta T < T < T_m + \Delta T$ it is unknown, but its integral is defined as follows:

$$\int_{T_m-\Delta T}^{T_m+\Delta T} C^*(T)\,dT = L + \int_{T_m-\Delta T}^{T_m} C_s(T)\,dT + \int_{T_m}^{T_m+\Delta T} C_l(T)\,dT \tag{3.37}$$

Heat capacity in the mushy zone may be approximated with different functions, but they have to be defined in such a way that eq. (3.37) is verified. Under the assumption that C_s and C_l are independent by temperature, a possible linear function of the approximated apparent heat capacity in this interval can be:

$$C^*(T) = \frac{L}{2\Delta T} + \frac{C_s + C_l}{2} \tag{3.38}$$

This is equivalent to say that the liquid fraction f varies linearly within the mushy zone [26]. Total Enthalpy is then a piecewise-linear function,while the Dirac-delta and consequently the apparent heat capacity are approximated by step functions. Another approximation often present in literature consists in defining the liquid fraction as a function of temperature through an error function. In that case the Dirac delta is approximated by a normal distribution over the mushy zone [27, 28]:

$$\frac{\partial f}{\partial t} = \frac{\sigma}{\sqrt{\pi}\Delta T} e^{-[\sigma^2(T-T_m)^2/\Delta T^2]} \tag{3.39}$$

where σ is chosen so that $erf(\sigma) = 1-\lambda$. Where λ is a sufficiently small number. If heat capacity is equal for liquid and solid phase $C_s = C_l = C_{sl}$, in the mushy zone according to normal distribution approximation, is defined as follows:

$$C^*(T) = C_{sl} + L\frac{\sigma}{\sqrt{\pi}\Delta T} e^{-[\sigma^2(T-T_m)^2/\Delta T^2]} \tag{3.40}$$

Apparent heat capacity may also be evaluated numerically by spatial and temporal averaging, as Lemmon [29] and Morgan et al [30] proposed in 1978 and 1979. Both methods consist in evaluating the apparent heat capacity by a numerical average of the enthalpy time-derivative $\partial H/\partial t$.

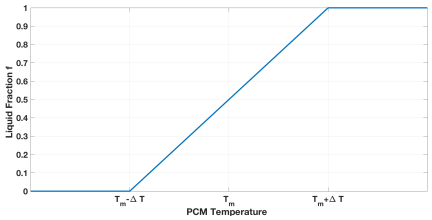

(a) Liquid fraction linear with temperature

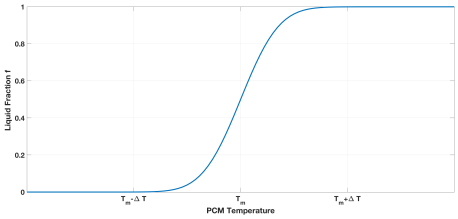

(b) Liquid fraction as error function of temperature

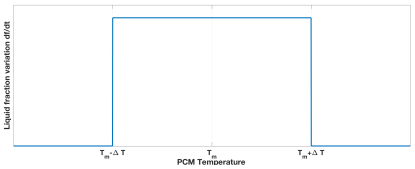

(c) Dirac Delta Approximation with step function

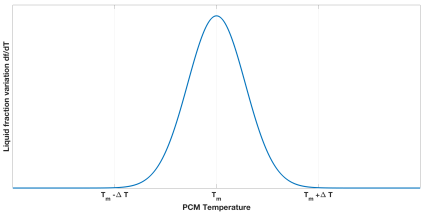

(d) Dirac Delta approximation with normal distribution

Figure 3.2. Approximations of liquid fraction and its derivative in the mushy zone.

Spatial averaging

$$C^*(T) = \sqrt{\frac{\nabla H \nabla H}{\nabla T \nabla T}} \tag{3.41}$$

where the spatial derivatives are evaluated all at the same time-step. It can be implemented both with implicit and explicit time schemes.

Time averaging The formulation of time-averaging depends on the time-scheme. For a 2 time-level explicit scheme the formulation is :

$$C^*(T^{(k)}) = \frac{H^{(k)} - H^{(k-1)}}{T^{(k)} - T^{(k-1)}} \tag{3.42}$$

A smoothed conductivity must be introduced as well to avoid the discontinuities. Usually a linear variation of k^* is assumed in the interval $T_m - \Delta T < T < T_m + \Delta T$. If k_s and k_l do not depend on the temperature, then the smoothed conductivity may be defined as:

$$k^* = \begin{cases} k_s & T \leq T_m - \Delta T \\ k_s + \frac{k_l - k_s}{2\Delta T}[T - (T_m - \Delta T)] & T_m - \Delta T < T < T_m + \Delta T \\ k_l & T \geq T_m + \Delta T \end{cases} \tag{3.43}$$

After the approximations, eq. (3.34) becomes :

$$C^*(T)\frac{\partial T}{\partial t} = \nabla\Big[k^*(T)\nabla T\Big] \tag{3.44}$$

3.2.3 Enthalpy porosity method

In the case of non-negligible convection heat transfer, it is needed to solve the velocity field in the liquid phase as well. As a consequence, Navier-Stokes equations have to be included in the model and the energy equation in liquid phase must take into account both diffusive and convective terms. As a result the model becomes much more complex and the computational time is subjected to a substantial increase. The mushy zone can be modelled as a porous medium, where porosity ϵ ranges from 0 to 1 and it is equal to the liquid fraction f. The governing equations are written in terms of superficial velocity $\mathbf{u}$, which is function of porosity ϵ and fluid velocity $\mathbf{u_l}$ [31].

$$\mathbf{u} = \epsilon \cdot \mathbf{u_l} \tag{3.45}$$

With the assumption of incompressible, Newtonian and laminar flow, the governing equations can be written as follows:

Continuity

$$\mathrm{div}(\mathbf{u}) = 0 \tag{3.46}$$

Momentum

$$\frac{\partial(\rho u)}{\partial t} + \mathrm{div}(\rho \mathbf{u} u) = \mathrm{div}(\mu \nabla u) - \frac{\partial p}{\partial x} + Au \tag{3.47}$$

$$\frac{\partial(\rho \nu)}{\partial t} + \mathrm{div}(\rho \mathbf{u} \nu) = \mathrm{div}(\mu \nabla \nu) - \frac{\partial p}{\partial y} + A\nu \tag{3.48}$$

$$\frac{\partial(\rho \nu)}{\partial t} + \mathrm{div}(\rho \mathbf{u} w) = \mathrm{div}(\mu \nabla w) - \frac{\partial p}{\partial z} + Aw + S_b \tag{3.49}$$

Where u, ν and w are the velocity components along x, y and z, p is pressure and S_b is the buoyancy source term, defined as:

$$S_b = \frac{\rho_{ref} \mathrm{g} \beta (h - h_{ref})}{c} \tag{3.50}$$

where β is the thermal expansion coefficient, ρ_{ref} and h_{ref} are reference values for density and sensible enthalpy, g is gravitational acceleration and c is the specific heat. A is a function of porosity, which comes from the Carman-Koseny equation (3.51), describing flows into porous media.

$$\nabla p = -\frac{C(1-\epsilon)^2}{\epsilon^3}\mathbf{u} \tag{3.51}$$

As a consequence A is defines as follows:

$$A = -\frac{C(1-\epsilon)^2}{\epsilon^3 + \lambda} \tag{3.52}$$

where C is a constant, that takes into account the mushy zone morphology and its kinetics, while λ is a constant introduced to avoid the division by zero. In solid cells, zero-porosity leads to a large value of A that prevails in momentum equation and forces velocity to zero. In liquid cells, A is zero, so the governing equations become the regular Navier-Stokes. The energy equation is expressed in terms of sensible enthalpy as follows [32]:

$$\frac{\partial \rho h}{\partial t} + \mathrm{div}(\rho \mathbf{u}) h = \mathrm{div}(k \nabla T) + S_h \tag{3.53}$$

where S_h is the source term related to the latent heat:

$$S_h = L\frac{\partial \rho f}{\partial t} + L\ \mathrm{div}(\rho \mathbf{u} f) \tag{3.54}$$

3.3 Phase field method

The phase field approximates the sharp interface to a finite thickness. To do this, an ordered parameter ϕ is introduced to distinguish the two phases. ϕ is equal to -1 in the solid and to 1 in the liquid, while in the interface region ϕ is comprised between -1 and 1. As a consequence, this model is a sort of a hybrid between mushy zone methods and sharp interface ones. The phase field method, however is based on a modified Stefan problem, which admits a non-isothermal interface. The boundary conditions on the interface, according to the modified Stefan problem are the following:

$$\rho L v_n = q_l - q_s \tag{3.55}$$

$$\rho s(T - T_m) = -\sigma(\kappa - \alpha v_n) \tag{3.56}$$

where q_l and q_s are the heat fluxes through the interface respectively in the liquid and solid domains, s is the specific entropy difference between solid and liquid phases ($Jkg^{-1}K^{-1}$), α is a kinetic coefficient (sm^{-1}) , κ is the curvature of the interface, σ is the surface tension and v_n is the normal component of the interface velocity. In the phase field method the Navier Stokes equation are modelled with an effective viscosity that is a function of the ordered parameter ϕ and assumes large values in the solid region in order to force zero velocity there :

$$\mu_{eff} = \frac{2\mu}{\phi + 1} \tag{3.57}$$

The latent heat in the energy equation is taken into account through a source term, function of the time derivative ϕ:

$$\frac{\partial \rho c_p T}{\partial t} + \mathrm{div}(\mathbf{u})(\rho c_p T) = \mathrm{div}(k \nabla T) + \frac{\rho L}{2}\frac{\partial \phi}{\partial t} \tag{3.58}$$

The phase field method needs an additional equation to solve the ϕ field and it is written as follows:

$$\alpha \xi^2 \frac{\partial \phi}{\partial t} = -\frac{\delta F(\phi, T)}{\delta \phi} \tag{3.59}$$

where ξ is a of characteristic length and $F(\phi, T)$ is the free energy functional, which is defined as :

$$F(\phi, T) = \int_\Omega \frac{1}{2}\xi^2 |\nabla \phi|^2 + f(\phi, T) dV \tag{3.60}$$

The first term represents the interfacial free energy, while the second is the bulk free energy. The free energy is the sum of a double-well potential and an interpolating function. Caginalp [33, 34] proposed the following phase field equation, however in literature there are other works in which the authors choose different forms:

$$\alpha \epsilon^2 \frac{\partial \phi}{\partial t} = \epsilon^2 \nabla^2 \phi - g'(\phi) + \frac{5\epsilon \rho s (T - T_m)}{8\sigma} f'(\phi) \tag{3.61}$$

where $g(\phi) = 1/8(\phi^2 - 1)^2$, $f(\phi) = 1/5\phi^5 - 2/3\phi^3 + \phi$ t and ϵ is the interface thickness. This equation is solved together with the energy equation and the Navier Stokes at every timestep.

3.4 Modelling of PCM packed beds

One of the biggest issues of these materials is their poor thermodynamic properties, especially the conductivity. Packed beds of macro or micro encapsulated spheres of PCMs are actively studied with this concern as it was mentioned in section 2.4 . Since they are not a continuous medium, but single spheres, the modelling approach should be different. De Gracia and Cabeza published a review about the models for this kind of systems [35] classifying them in two groups: single phase and two phase models. The firsts consider the fluid and the PCM as a single phase, while in the seconds they are modelled separately, so more equations have to be solved simultaneously.

Single phase models Single phase models are characterized by the strong hypothesis of equal instantaneous temperature between PCM and heat transfer fluid. This assumption is justified only for large thermal conductivities or small capsule dimensions. For a packed bed inside a cylinder the energy equation can be written as follows [36] :

$$\epsilon c_f \rho_f \frac{\partial T}{\partial t} + (1 - \epsilon)\rho_{PCM}\frac{\partial H^*}{\partial t} + c_f \rho_f u \frac{\partial T}{\partial y} = k_{eff,y}\frac{\partial^2 T}{\partial x^2} + k_{eff,r}\left(\frac{\partial^2 T}{\partial r^2} + \frac{\partial T}{2\partial r}\right) \tag{3.62}$$

where ϵ is the void fraction of the packed bed, the subscript f refers to the heat transfer fluid and $k_{eff,r}$,$k_{eff,y}$ are effective conductivities along axial and radial directions and H_m is the specific total enthalpy. According to this model, heat transfer fluid and PCM exchange heat through convection only along the axial direction. The effective conductivities present in the terms in right hand side of the equation consider also the natural convection of the liquid phase of the PCM.

Schumann model Schumann's model is a 1D two-phase model that considers heat transfer only on the axial direction and neglects heat conduction in both solid and liquid phases. The energy equations are written separately for the heat transfer fluid and phase change material:

$$\epsilon c_f \rho_f \Big(\frac{\partial T_f}{\partial t} + u \frac{\partial T_f}{\partial y} \Big) = h_{PCM-f}(T_{PCM} - T_f) - U_L(T_f - T_{ENV}) \tag{3.63}$$

$$(1-\epsilon) c_{PCM} \rho_{PCM} \frac{\partial T_{PCM}}{\partial t} = h_{PCM-f}(T_f - T_{PCM}) \tag{3.64}$$

where U_L and h_{PCM-f} are respectively the thermal transmittance between the fluid and the environment and the heat transfer coefficient between PCM spheres and the heat transfer fluid. The biggest limitation of this model is the absence of heat conduction,which leads to zero-thermal gradient into the spheres. The accuracy is compromised especially for large values of Biot number.

Concentric dispersion model In this model the liquid temperature is assumed to be uniform on the radial direction. It differs from the Schumann's model since it considers heat conduction within the PCM and heat transfer fluid. This means that thermal gradient inside PCM spheres is taken into account. The energy balance is written with three energy equations. Two describe the heat transfer between the heat transfer fluid and the PCM, while the other describes the heat conduction within the spheres, where convection of the liquid PCM is taken into account through an effective thermal conductivity.

$$\epsilon c_f \rho_f \Big(\frac{\partial T_f}{\partial t} + u \frac{\partial T_f}{\partial y} \Big) = \epsilon k_f \frac{\partial^2 T}{\partial y^2} + h_{PCM-f}(T_{PCM} - T_f) - U_L(T_f - T_{ENV}) \tag{3.65}$$

$$(1-\epsilon) c_{PCM} \rho_{PCM} \frac{\partial H}{\partial t} = (1-\epsilon) k_{PMC} \frac{\partial^2 T}{\partial y^2} h_{PCM-f}(T_f - T_{PCM}) \tag{3.66}$$

$$\rho_{PCM} \frac{\partial H}{\partial t} = \frac{1}{r^2} \frac{\partial}{\partial r} \Big(k_{PCM}\ r^2 \frac{\partial T}{\partial r} \Big) \tag{3.67}$$

Continuous solid phase models In continuous solid phase models, PCM packed beds are modelled as continuous porous mediums and not as single spheres. As a consequence thermal gradient is not modelled inside the PCM spheres and heat conduction within the PCM occurs on both directions. However, the problem can be simplified keeping a good accuracy by neglecting the heat conduction on the radial direction. The energy equations are two and are written as follows:

$$\begin{aligned} \epsilon c_f \rho_f \Big(\frac{\partial T_f}{\partial t} + u \frac{\partial T_f}{\partial y} \Big) = k_{f,y} \frac{\partial^2 T_f}{\partial y^2} + k_{f,r} \Big(\frac{\partial^2 T}{\partial r^2} + \frac{\partial T}{r \partial r} \Big) \\ + h_{PCM-f}(T_{PCM} - T_f) - U_L(T_f - T_{ENV}) \end{aligned} \tag{3.68}$$

$$\begin{aligned} (1-\epsilon) c_{PCM} \rho_{PCM} \frac{\partial H}{\partial t} = k_{PCM,y} \frac{\partial^2 T_{PCM}}{\partial y^2} + k_{PCM,r} \Big(\frac{\partial^2 T}{\partial r^2} + \frac{\partial T}{r \partial r} \Big) \\ + h_{PCM-f}(T_f - T_{PCM}) \end{aligned} \tag{3.69}$$

Additionally Navier-Stokes equations equation are needed in order to solve the velocity field.

Chapter 4

Numerical modelling of a PCM cylinder for cooling energy storage

4.1 Introduction

In a previous work Mongibello et al. [37] simulated the charge and discharge of cooling energy with 2.4 kg of PCM encapsulated in an aluminium cylinder. They implemented two models in Comsol using the apparent heat capacity method. The first is conduction-based, so it neglects convective phenomena, while the second is a conduction-convection-based model, where the viscosity in the momentum equations is modified, using an enthalpy-porosity approach, to force zero-velocity in the solid elements. The authors compared the numerical results with the experimental ones obtained with a climatic chamber. The conduction-convection-based model was validated, while the conduction-based was proved to be inaccurate due to the non deniable free convection during the phase change, especially during melting. In this chapter, the same procedure is followed to test three other methods. Two variants of the enthalpy method and a moving boundary method have been implemented in Comsol Multiphysics.

4.1.1 Description of the case study

In the experiment conducted by Mongibello et al., the PCM is encapsulated in an aluminium bottle with a radius of 6.9 cm and a height of 25.0 cm. The material is a paraffin used for cooling applications thanks to its low melting temperature. Its thermophysical properties are summarized in Table 4.1.

Property	**Value**
Melting temperature	15° C
Latent heat	182 kJ/kg
Thermal conducitvity	0.25-0.15 $WK^{-1}m^{-1}$
Density	950-860 kg/m^3
Specific heat	2250-2560 $Jkg^{-1}K^{-1}$
Viscosity	0.00365 $Pa \cdot s$
Isobaric expansion coefficient	0.0003085 $1/K$

Table 4.1. Thermophysiscal properties of the PCM

The experiment consists of two phases: charge and discharge. During the charge, the temperature

of the air in the climatic chamber is initially equal to the ambient temperature $T_a = 23.8°C$, but with one hour-ramp it is taken down to $7°C$. Then, it stays at this temperature for the rest of the whole transient. The PCM is kept inside the chamber for a total of 72h. When the charge is completed, the discharge begins, but another hour ramp is necessary to bring the the climatic chamber to the discharge temperature $T_d = 23°$ C. Then, the climatic chamber is kept at this temperature for about 14 h. The initial one hour ramps are also simulated and can be advantageous in terms of numerical stability, because they imply a smooth variation from the initial values to the boundary conditions. The top and bottom surfaces of the cylinder are kept insulated during the whole experiment, while the lateral surface is characterised by convective heat transfer with the air inside the climatic chamber. During charge, the empirical correlations give a heat transfer coefficient $h_l = 30.2W/m^2/K$, while during discharge it is $h_l = 29.1W/m^2/K$. The temperature is measured in different points with five thermocouples forming a cross, placed at a distance of 9 cm from the bottom: one on the axis, while the others at a distance of 3.45 cm from it. In all the three models, thermophysical properties are considered to be constant with temperature. As a consequence, the average values between the solid and liquid are considered . What is more, the material is assumed to be homogeneous and isotropic and volume variations are not taken into account. Hence, the average density used in the three models is $\rho = 905kg/m^3$ and the height of the PCM cylinder is considered to be equal to 17.73 cm, instead of 24 cm.

4.2 Enthalpy method

Thanks to the axial-symmetry of the cylinder it is possible to consider a 2D domain, saving precious computational time. The mesh(Figure 4.1) is built using the physics-controlled meshing tool in Comsol. The enthalpy-method is implemented to simulate both charge and discharge, but two different approaches are proposed: a conduction-based model and a conduction-convection one. Therefore, two or three physics, depending on the model, are added to the Comsol application. For the conduction based method they are heat transfer solids and an algebraic equation to couple the enthalpy function of temperature to the heat transfer equation, while for the second model there is heat transfer in fluids, laminar flow and the enthalpy algebraic equation. The non-linear equations are solved with the automatic Newton solver, with 1e-3 of tolerance and a maximum of 10 iterations, because with the default tolerance of 1e-2 there are numerical stability problems. The minimum step is set to 1e-4 s, while the maximum time-step to 100 s.

4.2.1 Conduction-based model

Although it was already proved that a conduction-based model is too inaccurate, it was decided to implement it again with the enthalpy method as starting point for the conduction-convection-based model. The main assumptions of this model are : (i) homogeneous and isotropic material; (ii) constant thermophysical properties equal to the average between solid and liquid values; (iii) the phase change is not isothermal, but it occurs over a finite temperature range; (iv) convective heat transfer is neglected. The enthalpy formulation, under which the model is based, can be written as:

$$\rho_{PCM}\frac{\partial H}{\partial t} = k_{PCM}\nabla^2 T \tag{4.1}$$

where ρ_{PCM} is the average density of the PCM ,k_{PCM} is the thermal conductivity and H is the total specific enthalpy, sum of the contributions given by latent heat and sensible enthalpy.

$$H = f(T)L + h_{ref} + c_p(T - T_{ref}) \tag{4.2}$$

where $f(T)$ is the liquid fraction function of temperature, c_p is the average specific heat, h_{ref} is the reference value of sensible enthalpy and T_{ref} is the reference temperature. Since, only enthalpy

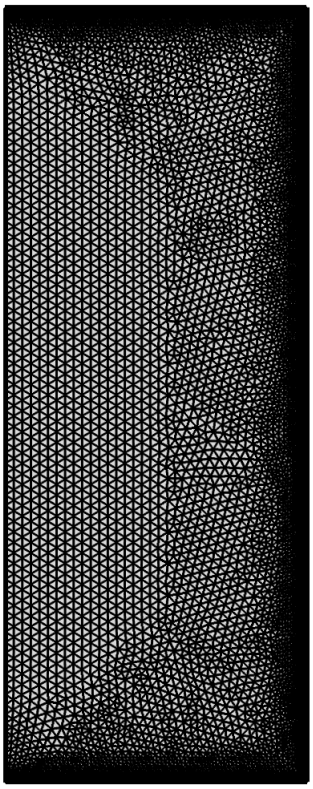

Figure 4.1. The mesh used for the simulation. It consists of 11969 elements.

variations and gradients are relevant, the results do not depend on the arbitrary reference values. In this case, they are set to $T_{ref} = 0K$ and $h_{ref} = 0Jkg^{-1}K^{-1}$. The liquid fraction is assumed to vary linearly with temperature as follows:

$$f(T) = \begin{cases} 0 & T \leq T_m - \Delta T \\ \frac{T - T_m + \Delta T}{2 * \Delta T} & T_m - \Delta T < T < T_m + \Delta T \\ 1 & T \geq T_m + \Delta T \end{cases} \tag{4.3}$$

4.2.2 Conduction-convection-based model

In the second model, convection is taken into account, so the Navier-Stokes need to be solved. The flow is assumed to be Newtonian, laminar and incompressible. With the enthalpy porosity method the phase change material is modelled as a porous media, where the porosity varies with time and space and it is equal to the liquid fraction. Under these assumptions, the Navier-Stokes equations can be written as follows:

$$\frac{\partial u}{\partial r} + \frac{\partial w}{\partial z} = 0 \tag{4.4}$$

$$\rho_{PCM}\Big(\frac{\partial u}{\partial t} + u\frac{\partial u}{\partial r} + w\frac{\partial u}{\partial z}\Big) = -\frac{\partial p}{\partial x} + \mu'\Big(\frac{\partial^2 u}{\partial r^2} + \frac{1}{r}\frac{\partial u}{\partial r} + \frac{\partial^2 u}{\partial z}\Big) \tag{4.5}$$

$$\rho_{PCM}\Big(\frac{\partial w}{\partial t}+u\frac{\partial w}{\partial r}+w\frac{\partial w}{\partial z}\Big)=-\frac{\partial p}{\partial z}+\mu'\Big(\frac{\partial^2 w}{\partial r^2}+\frac{1}{r}\frac{\partial w}{\partial r}+\frac{\partial^2 w}{\partial z}\Big)+S_b \tag{4.6}$$

where u and w are the velocity components along radial and axial directions, while S_b is the buoyancy force according to the Boussinesq approximation:

$$S_b=\beta\rho g(T-T_m) \tag{4.7}$$

in which β is the isobaric expansion coefficient and g is the gravity acceleration. The modified viscosity μ' comes from Carman-Koseny equation and forces velocity to zero in the solid elements.

$$\mu'=\mu(1+A(T)) \tag{4.8}$$

where A(T) is defined as:

$$A(T)=C\frac{(1-f(T))^2}{f(T)^3+\delta} \tag{4.9}$$

C is a constant, typically between 10^3 and 10^{10}, while δ is only a numerical constant needed in order to avoid division by zero. In this case it is fixed to 10^{-3}. The energy equation in terms of total enthalpy is written as follows:

$$\rho\Big(\frac{\partial H}{\partial t}+u\frac{\partial H}{\partial r}+w\frac{\partial H}{\partial z}\Big)=k\Big(\frac{\partial^2 T}{\partial r}+\frac{1}{r}\frac{\partial T}{\partial r}+\frac{\partial^2 T}{\partial z}\Big) \tag{4.10}$$

4.2.3 Initial and boundary conditions

During charge, the PCM is at an initial temperature of 23.8° C. The lateral surface of the cylinder is characterised by a convective heat flux between the PCM and air. The heat transfer coefficient h_l is $30.2W/m^2/K$, while the air is initially at the same temperature of the PCM, but in the first hour of the transient it is brought down to 7° C. On the axis, a symmetry boundary condition is applied, while the top and bottom surfaces of the cylinder are adiabatic. Concerning the discharge, the initial temperature of air and PCM is set to 7.5 $°C$. In the first hour the air is heated up to the discharge temperature $T_d = 23°$. During the discharge, the heat transfer coefficient is slightly smaller: $h_l = 29.1W/m^2/K$. In the conduction-convection model the no-slip condition is applied to all boundaries except for the axis, where, instead, a symmetry boundary condition is defined. Furthermore, a pressure point condition is set in one of the four points defining the domain and the initial velocity values are set equal to zero.

4.2.4 Results

Firstly different simulations were run, in order to perform a parametric sweep and obtain the optimal sets of parameters that give the most accurate results. The parameters that fit better with the experimental results are listed in the Table 4.2.

Parameter	Charge	Discharge
C	$10^{3.7}$	$10^{3.7}$
$\Delta T[K]$	1	4
$T_m[°C]$	12.5	15

Table 4.2. Sets of parameters for the two cases

Figure 4.2 shows the comparison between the temporal variation of the experimental and numerical temperatures during the charge. Although the theoretical solidification temperature is 15° C,

the experimental results show a non-negligible sub-cooling and is the reason for which the phase change temperature is set to 12.5° in the simulations, instead than 15°C. The conduction-based model underestimates the heat transfer ratio within the PCM, since it does not consider natural convection. According to this model, the temperature decreases much slower at the beginning and at the end of the transient. What is more, in the conduction-based model the absence of free convection neglects the fluid-mixing, which leads to a radial temperature profile. On the other hand, the estimated time to complete solidification is very close to the experimental one, which is about 60 h. The numerical results obtained by the conduction-convection-based model show a quite good agreement with the experimental data. In particular, the curve describing the temporal variation of the temperature at the mid-radius point is almost overlapped with the experimental one. Free convection is dominant in the first hours of the transient, before the inner layers start to crystallize, thanks to the continuous mixing of the fluid in the inner part. After that, conduction becomes the dominant heat transfer mode, because of the continuous decrease of liquid fraction.

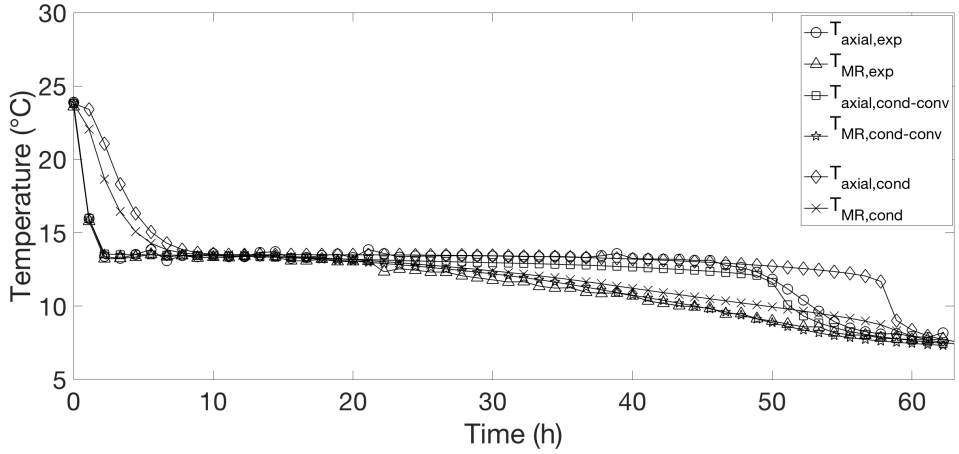

Figure 4.2. Temporal variation of temperatures according to the experiment and to the numerical simulations during the charge

Figure 4.3 represents the numerical curves obtained for the discharge. The transient in this case is much faster: the phase change material melts almost completely in about 14 h. At the beginning, the material is fully solid, so convection is prevalent and, in fact, the conduction-based method is quite accurate in the first 4 hours. After, free convection starts to play an important role and the conduction-based method underestimates the heat transfer ratio, since the thickness of the melted layer increases. Indeed, after 14 h there is a difference of more than 10 degrees between the measured temperatures and the numerical ones obtained by the conduction-based model. Figure 4.4 shows the evolution of the temperature profile during the charge, according to the conduction-convection model. Concerning the conduction-convection-based method, as it was already mentioned, it was necessary to perform a parametric sweep in order to obtain curves more similar to the experimental ones. With this set of parameters, the simulated temperature variation on the axis, is in good agreement with the experimental one, but it still underestimates the final temperature of about 1-2 ° C. On the other hand, the curve relative to the mid-radius point is distant from the experimental one, especially after the inflection point. Figure 4.5 shows the temperature profile at four different time instants. At the beginning, the profile is radial, because conduction is the prevalent heat transfer mode, since at t=0 all the PCM is solid. As the thickness of the melted layer increases, the mixing effects start to be more relevant and, therefore

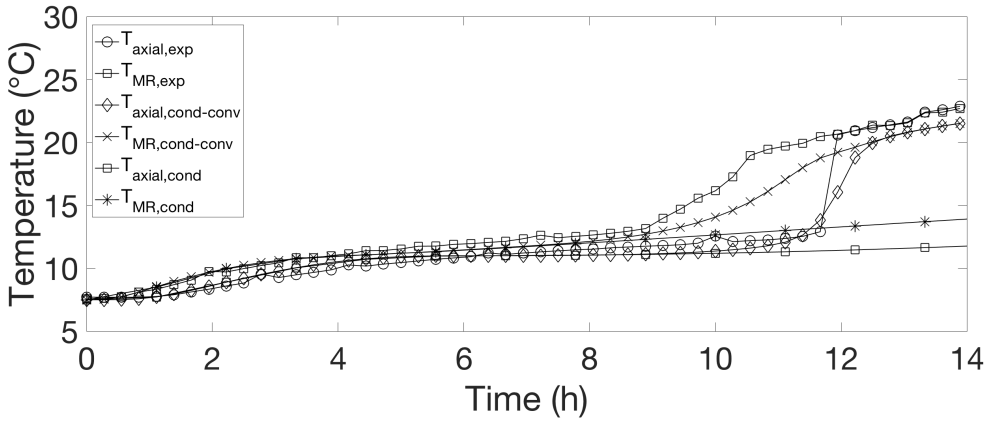

Figure 4.3. Temporal variation of temperatures according to the experiment and to the numerical simulations during the discharge

heat transfer ratio increases in the upper part and the temperature profile becomes bi-dimensional.

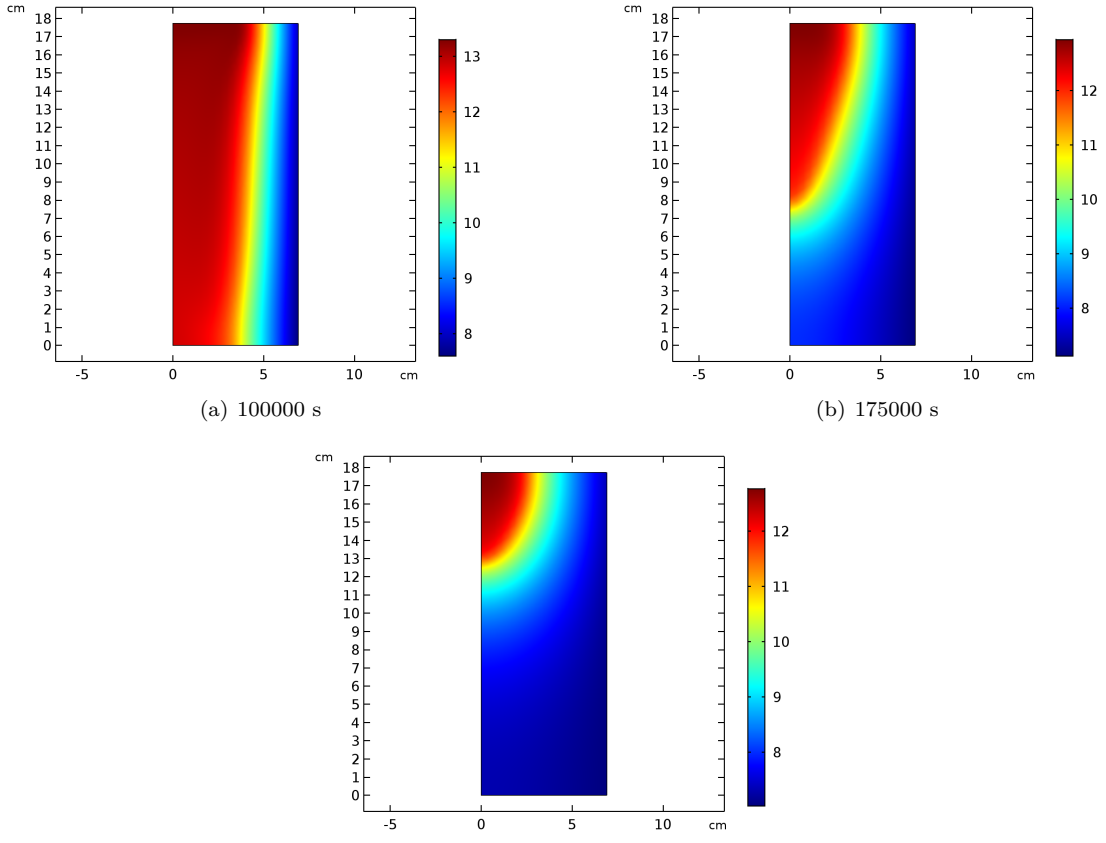

(a) 100000 s

(b) 175000 s

(c) 200000 s

Figure 4.4. Enthalpy porosity method: temperature profile evolution during charge

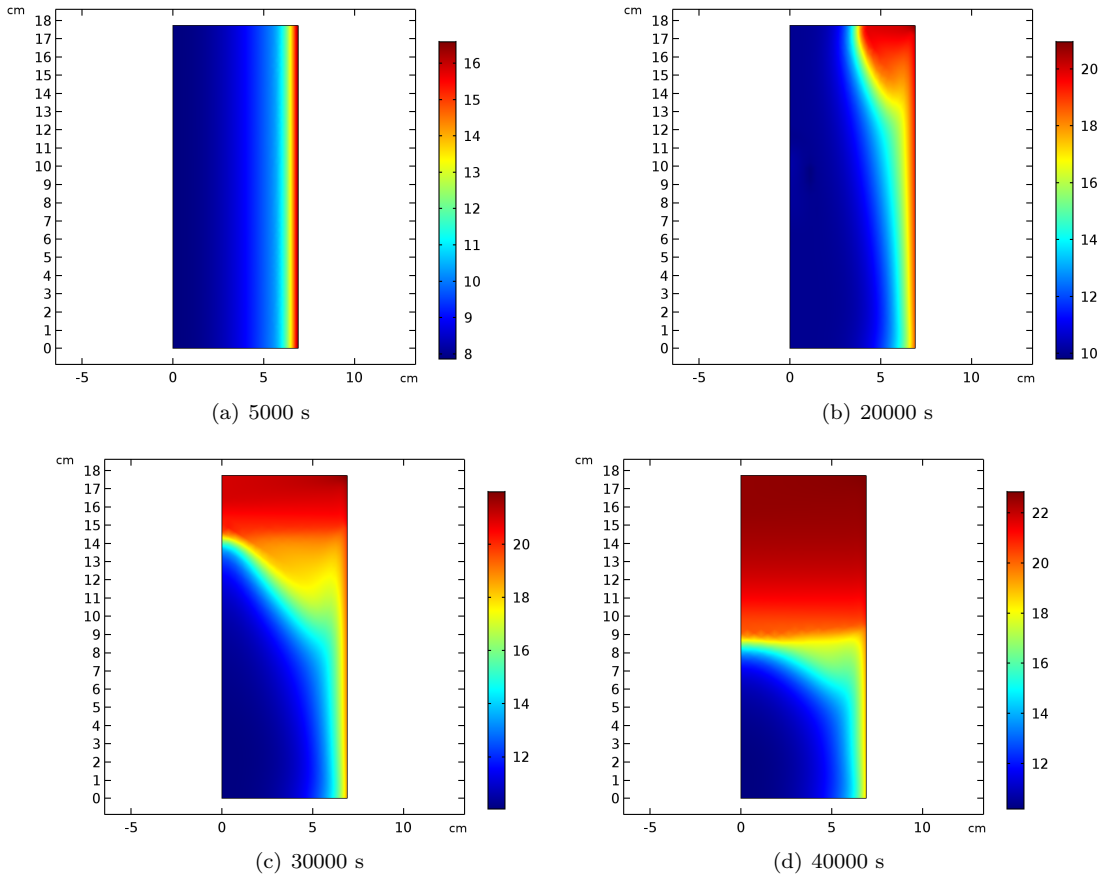

(a) 5000 s

(b) 20000 s

(c) 30000 s

(d) 40000 s

Figure 4.5. Enthalpy porosity method: temperature profile evolution during discharge

4.2.5 Improvements to the discharge model

The parametric sweep found the best set of parameters for the discharge modelling, however the results coming from these simulations matched only partially with the experimental data. There is a difficulty in fitting the results both on the axis and on the mid-radius points . With this set of parameters, the experimental and numerical curves related to the axial point are very similar, but there are sensible differences between the temperature curves relative to the mid-radius point, especially after the inflection point. Slightly better results can be obtained with a different function for the liquid fraction. In other simulations f(T) is chosen with an error function behaviour, by using the step function tool in Comsol. In Figures 4.6, 4.7 and 4.8 the three most accurate results according to three different sets of parameters are shown. Although the numerical curves show a better agreement with the experimental ones, it is still impossible, with any set of parameters to match accurately both experimental curves. In figure 4.6 and 4.7 the results concerning the mid-radius point are very close to experimental ones, but there are some differences for the axial point results, especially in the time range comprised between 11 and 12 h. In figure 4.8 the results have a medium accuracy for both points, because it was tried to find a trade-off and to obtain numerical curves not too distant from the experimental ones in both axial and mid-radius points.

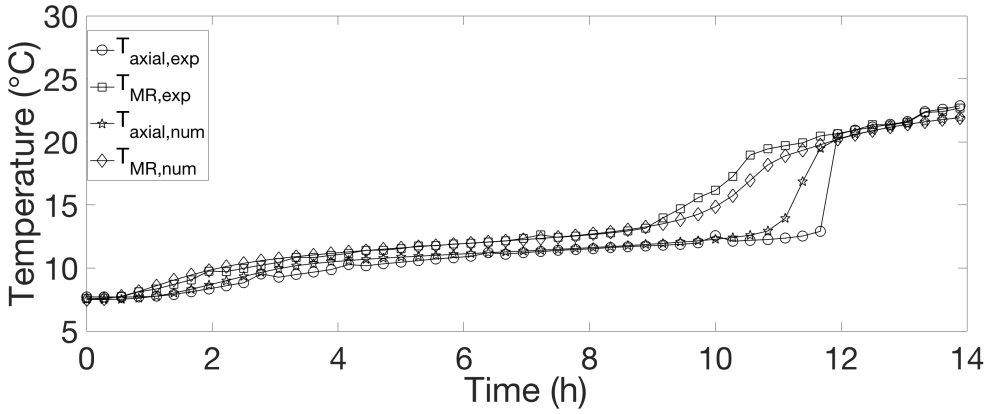

Figure 4.6. Discharge numerical results obtained with error function liquid fraction, $\Delta T = 5K$and C=$10^{3.58}$

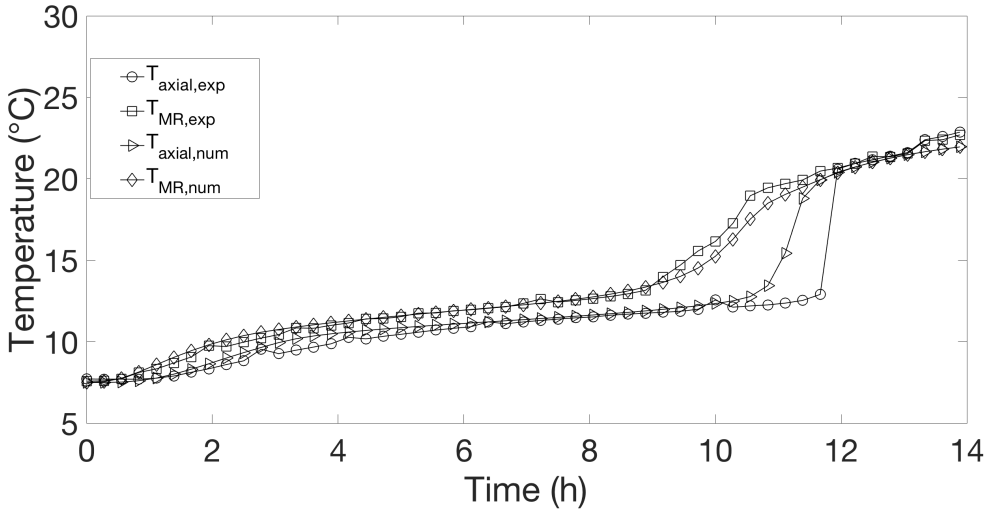

Figure 4.7. Discharge numerical results obtained with error function liquid fraction, $\Delta T = 5K$and C=$10^{3.55}$

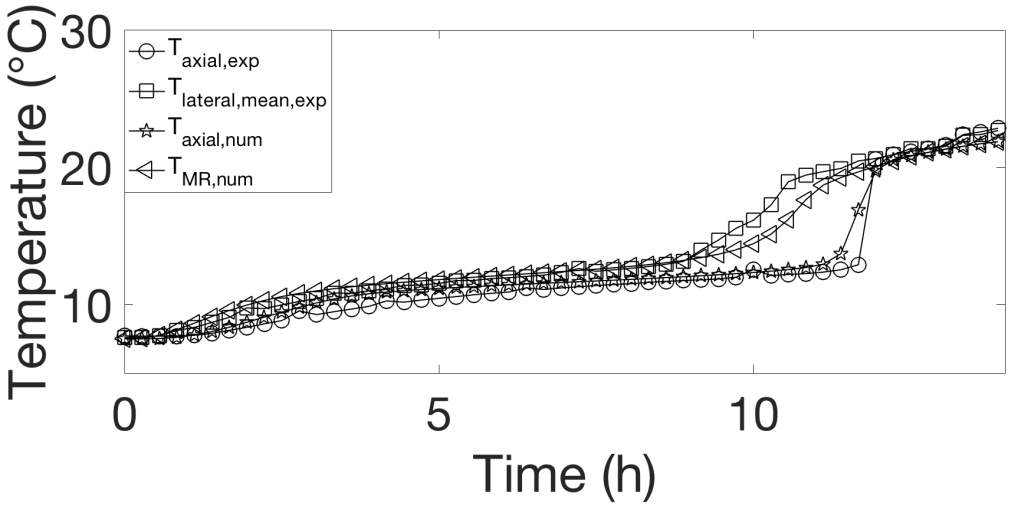

Figure 4.8. Discharge numerical results obtained with error function liquid fraction, $\Delta T = 4.5K$and C=$10^{3.6}$

4.3 3D Enthalpy porosity method

In this section a variant of the enthalpy porosity method is tested. It is very similar to the model implemented in the previous section, but the difference relies in the way the velocity is forced to zero in solid elements. In this model a Darcy source term is added to the momentum equations. Unfortunately, with this method it is not possible to exploit the axial-symmetry, because the Darcy source term must be included in all the three components of the momentum equations. As a consequence a 3D model is implemented in COMSOL, but the boundary conditions and the initial values are the same ones described in the previous section. Because of the highly non-linearity of

these source terms, it is necessary to include the Carman-Koseny function also in the viscosity, in order to guarantee numerical convergence. Since, the geometry is 3D and the equations are highly non-linear, the simulations are largely computational expensive. For this reason, it was preferred to use the apparent heat capacity approach to model the phase change, rather adding the additional equation for the enthalpy. The mesh of Figure 4.9 is built using the physics-controlled meshing tool in Comsol. The main assumptions, the boundary and initial conditions are the same of the 2D enthalpy model, therefore the flow is considered as incompressible, Newtonian and laminar, therefore the modified Navier Stokes equations are written as follows:

$$\frac{\partial(\rho u)}{\partial t} + \mathrm{div}(\rho \mathbf{u} u) = \mathrm{div}(\mu' \nabla u) - \frac{\partial p}{\partial x} + A(T)u \tag{4.11}$$

$$\frac{\partial(\rho v)}{\partial t} + \mathrm{div}(\rho \mathbf{u} v) = \mathrm{div}(\mu' \nabla v) - \frac{\partial p}{\partial y} + A(T)v \tag{4.12}$$

$$\frac{\partial(\rho w)}{\partial t} + \mathrm{div}(\rho \mathbf{u} w) = \mathrm{div}(\mu' \nabla w) - \frac{\partial p}{\partial z} + A(T)w + S_b \tag{4.13}$$

4.3.1 Charge

For the charge model, different mushy zone constants were tested, fixing a medium melting temperature $T_m = 12.5°C$ and half temperature range $\Delta T = 1K$. The value for the constant C that provided the best numerical results compared with the experimental ones is $C = 10^{4.1}$. Figure 4.10 shows the numerical results obtained by this simulation. There is good agreement between the numerical and experimental results for the whole transient. In the first part, when natural convection is dominant, the curves are practically overlapped, they start to slightly deviate from the experimental ones only after 20 h. However the error is still very small and, therefore, acceptable . Figure 4.11 shows the evolution of the temperature profile during charge according to the 3D enthalpy porosity method. The results are very similar with the one of Figure 4.4.

4.3.2 Discharge

Concerning the melting, firstly some simulations were run trying different mushy zone constants, but the results were too far from the expected ones. After that, the idea was to try with two different constants: one for the apparent viscosity definition and one for the source term. The results ameliorated, but they are still very far from the experimental ones. The best ones are obtained with the parameters of Table 4.3:

Parameter	Value
C_μ	$10^{1.5}$
C_u	10^6
$\Delta T[K]$	5
$T_m[°C]$	15

Table 4.3. Set of parameters

where C_u and C_μ respectively are the mushy zone constants for the source term and the apparent viscosity. Figure 4.12 shows the comparison of the results. The curves relative to the axial and mid-radius points are too close to each others, especially after the second point starts to melt. As a consequence, the first variant of the enthalpy method, without the source term has proven to predict better the behaviour of the PCM during the melting. The difference between the models, can be noticed also from Figure 4.13, which shows the temperature profile at four different time instants.

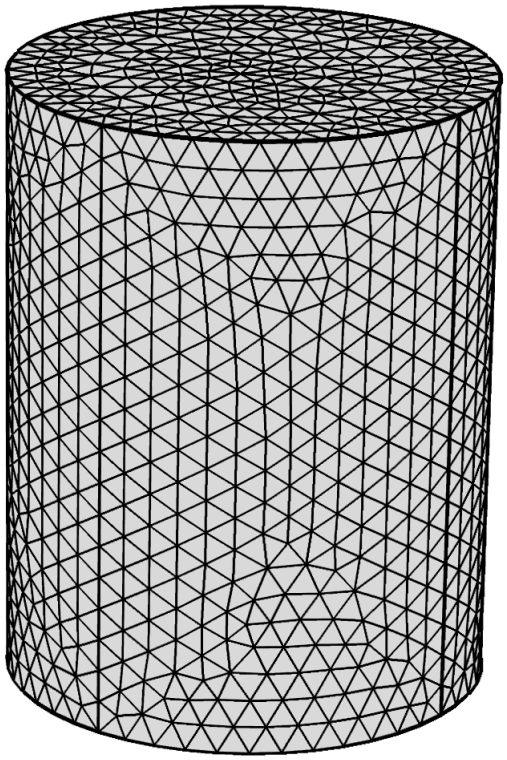

Figure 4.9. 3D Mesh used for the simulations of charge and discharge

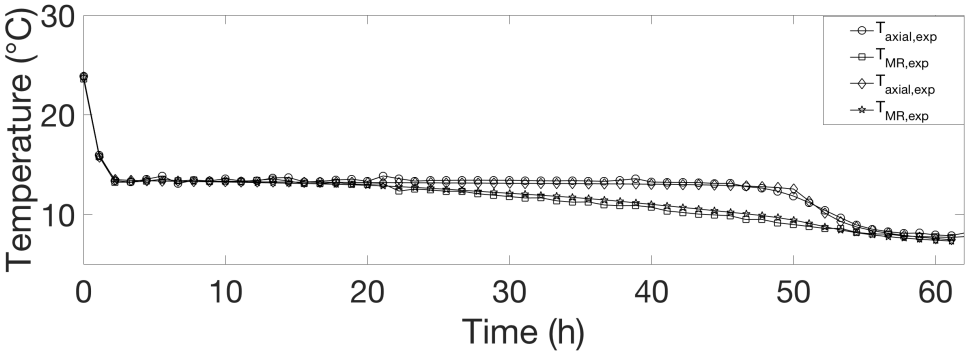

Figure 4.10. Time variation of temperatures: experimental vs. numerical results

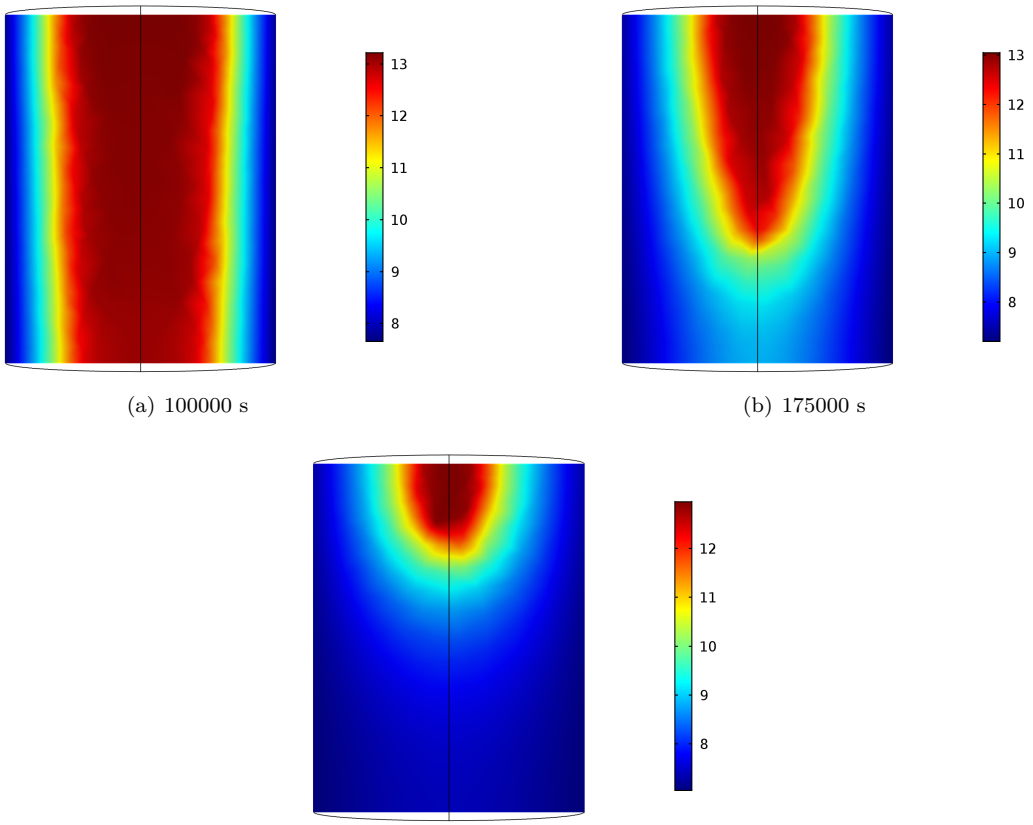

(a) 100000 s

(b) 175000 s

(c) 200000 s

Figure 4.11. Enthalpy porosity method 3D model: temperature profile evolution during charge

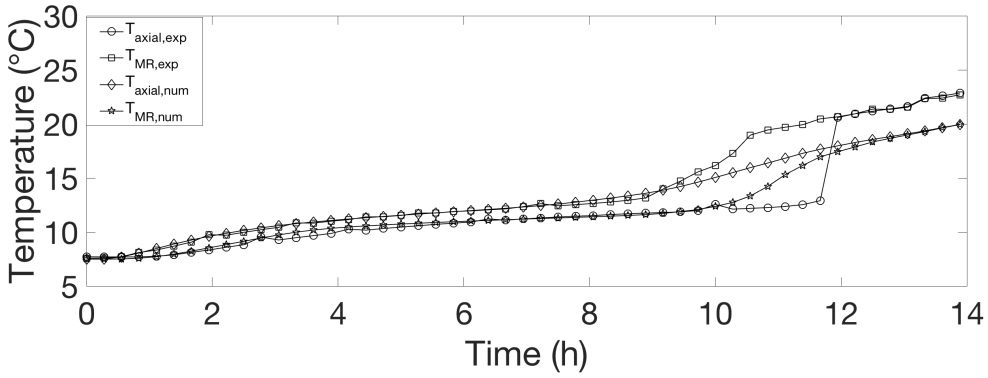

Figure 4.12. Comparison between the numerical and experimental results

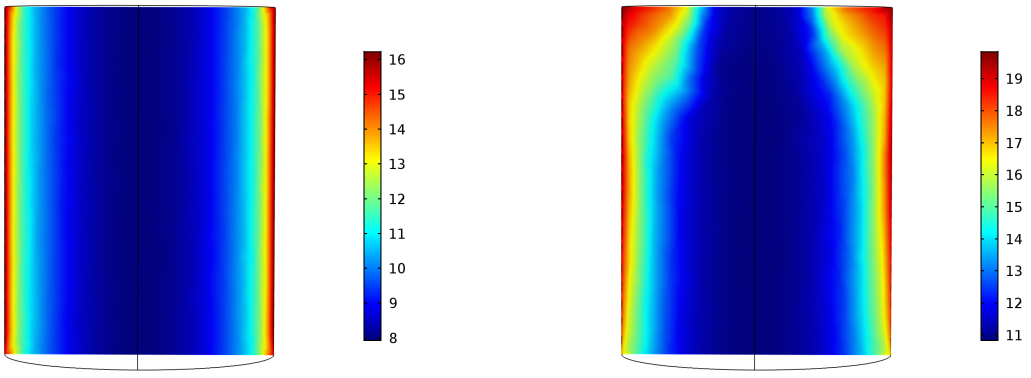

(a) 5000 s

(b) 20000 s

(c) 30000 s

(d) 40000 s

Figure 4.13. Enthalpy porosity method 3D model: temperature profile evolution during discharge

4.4 Moving boundary method

A moving boundary method has been implemented too, using the deformed geometry physics in Comsol, which allows to deform geometries or domains during a transient. In this case, at time t=0 the geometry is characterised by two inner domains, a fluid and a solid one. The phase front is an internal interface, characterised by a Dirichlet boundary condition and a normal velocity that has to satisfy the Stefan condition. Navier Stokes equations are solved only in the liquid domain, where $T > T_m$, but since the interface moves, the liquid domain increases or decreases depending on weather the PCM is melting or solidifying. Neither the deformed geometry or the ale method are able to model topology changes in the geometry. This means that a domain or a boundary, initially associated to solid or liquid elements, can get smaller or bigger, but it can not be created from zero or vanish completely. For this reason , the first part of the transient, both for charge and discharge are simulated with the enthalpy porosity method, until a part of material has changed its phase. Since the mesh gets deformed during the transient, an automatic remeshing is needed: when the mesh elements reach a certain distortion the mesh is automatically rebuilt. Without the remeshing, the elements would get too distorted and there would be numerical convergence issues.

4.4.1 Charge

The first four hours are simulated with the enthalpy porosity method. The resulting temperature and velocity profiles are saved and taken as initial condition for the new model. The melting temperature is fixed to $T_m = 13°C$. As it was mentioned before, the deformed-geometry method can not model topology changes, so it is not possible to simulate in one step the whole transient, because as the interface gets closer to the axis, the mesh is rebuilt continuously without allowing a complete vanishing of the liquid domain. Therefore the simulation is stopped once the liquid domain becomes really small(radial thickness of the order of μm). A new simulation from this time-step starts assuming that the domain is fully solidified so in this last simulation only the heat diffusion equation is solved.

4.4.2 Discharge

The first hour is simulated with the enthalpy porosity method and the resulting temperature profile is set as initial condition for the moving boundary model of discharge. Initially a first test was done with a melting temperature $T_m = 15°C$, but the numerical results start to differ from the experimental ones already after five thousand seconds. The problem is that by setting this melting temperature, the solid region gets heated too quickly and after few thousand of seconds it reaches temperature values close to the phase change one. As a consequence, it was tried to use a $T_m = 13°C$ and the situation slightly got better. On the other hand the temperature profile in the solid region tends to become more homogeneous with a smaller melting temperature. What is more, it appears that the phase front moves too quickly, if compared with the experimental results. In any case, as it was already mentioned, the deformed-geometry physics has the problem of not allowing topology changes, so the simulations can not continue once the interface gets very close to the axis. This issue can be solved by mean of an artifice: the simulation can be stopped once the phase front reaches a very small distance from the axis, then the mesh is saved and a translation of 0.1 mm is applied to the whole geometry in the direction of the axis and finally every point with negative radial coordinate is deleted. As consequence, in the new domain the interface is moved to the axis, but the whole geometry is a 0.1 mm thinner than the original one. After the geometry is modified successfully, a new simulation starts, assuming as initial values the results from the last time-step of the previous simulation.

4.4.3 Results

Concerning the charge, Figure 4.14 shows the comparison between the experimental and numerical results obtained with the deformed geometry model. The numerical and experimental curves relative to the mid-radius point are very similar and almost overlapped for the whole transient. On the other hand, concerning the axial point, the experimental curve shows a sensible delay in completing the phase transition. Apart from this problem, the curves present the same behaviour and this delay is probably due to the fact that the initial part of the transient was simulated with the enthalpy porosity method. In fact the first part is the most crucial, since it is the time lapse in which natural convection plays a dominant role. The difference in the results could be also related to the fact that the material does not present a sharp isothermal interface, but it changes its phase within a finite temperature range. In fact the experimental results show a much smoother variation of temperature after the material has completed the solidification. What is more, the temperature profile tends to evolve in a completely different way, if compared to the other methods. In fact Figure 4.15 shows the temperature profile at 4 time instants and although at the beginning of the transient the profile is bidimensional, later it becomes almost radial. The

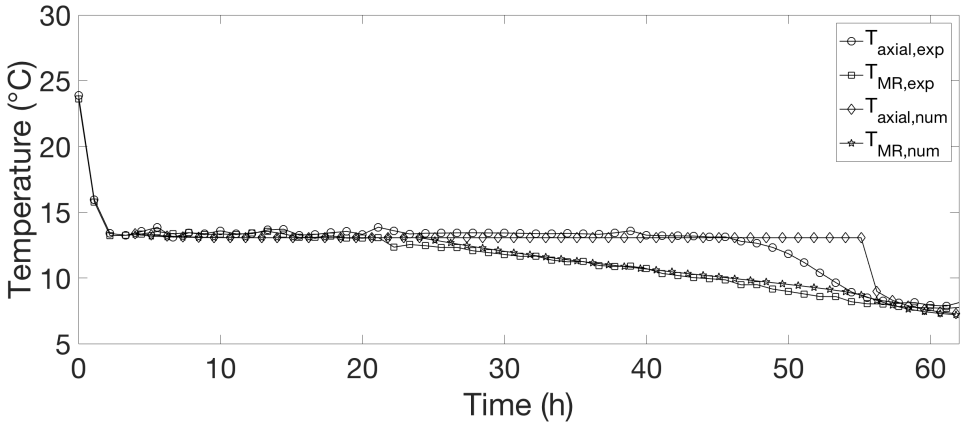

Figure 4.14. Solidifcation numerical results vs. experimental ones: moving boundary method

results regarding the discharge are completely different from the experimental ones. The solid part tends to reach a homogeneous temperature, because of the moving Dirchlet boundary condition. For this reason the numerical curves relative to the axial and mid-radius points tend to be much closer to each other. This distance between the two curves decreases even more if a lower melting temperature is assumed. On the other hand with a T_m of 15 $°C$, the temperature in the solid domain increases too rapidly, especially in the first part of the transient. With a temperature of $T_m = 13°C$ this problem is reduced, but the numerical temperatures calculated both on the axial and on the mid radius points are still larger than the experimental ones as it shown in Figure 4.16. What is more the whole discharge process according to this model is much faster than what experimented, since in the simulation the axial point melts after only 8 hours, while in the real experiment it took about 12 hours. These problems are probably related to the fact that the given material changes its phase over a larger temperature range rather than having an isothermal phase change. The only strength point that this model presents, is the relative large time difference between the inflection points of the two curves. This time difference depends on the shape and the motion of the phase interface. If it moves radially, the time difference is maximum, while if it moves axially the points at the same height melt at the same instant. With the enthalpy methods, this time difference was smaller and made it impossible to perfectly match both experimental

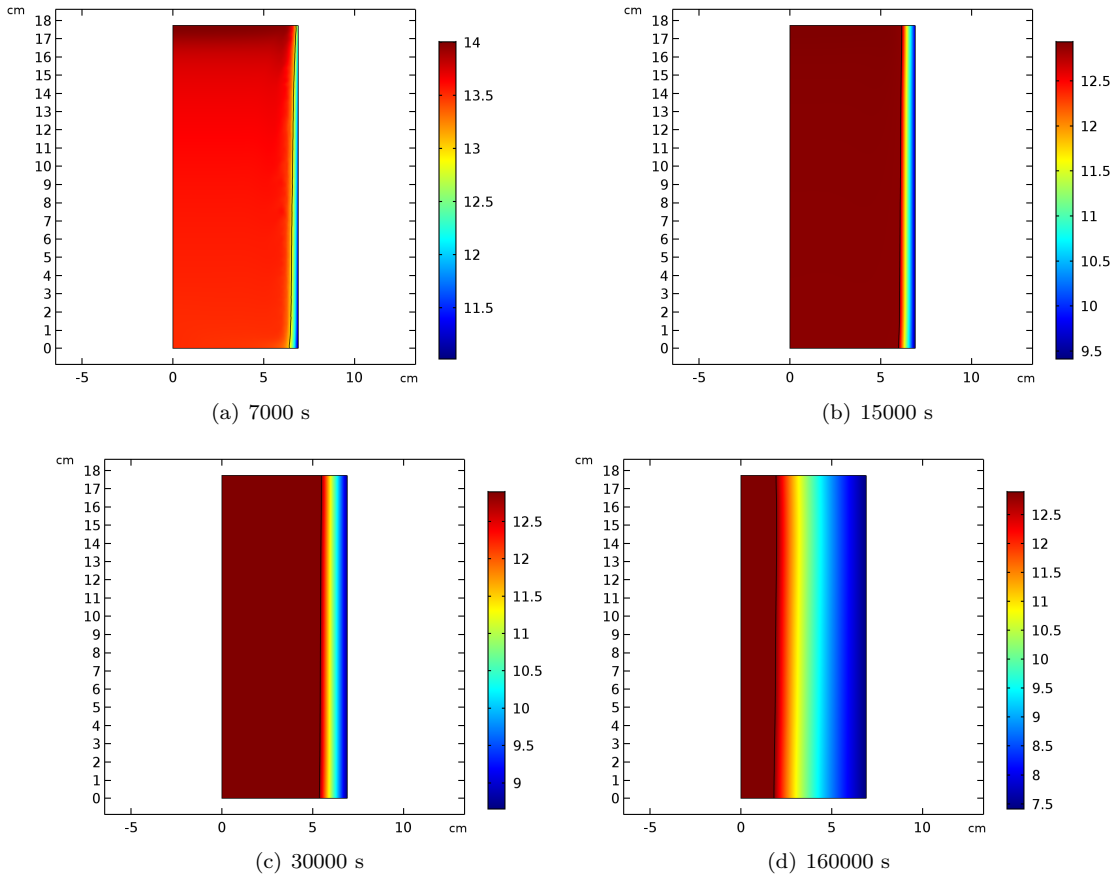

(a) 7000 s

(b) 15000 s

(c) 30000 s

(d) 160000 s

Figure 4.15. Moving boundary method: temperature profile evolution during charge

curves even with the best set of parameters. In this case, there is no parameter sweep that can be performed, since all the physical properties are certified and neither the mushy zone or the melting temperature range are present in the model. Figure 4.17 shows the temperature profile

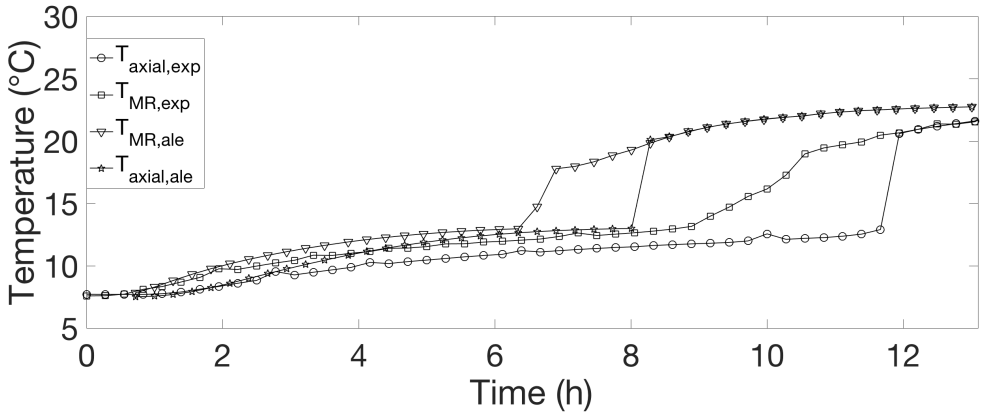

Figure 4.16. Melting numerical vs. experimental results : moving boundary method

of a half section at four different timesteps. From this figure it is even clearer that this model overestimates the heat transfer ratio. In fact, the interface takes about 10000 seconds to reach axis, while according to enthalpy methods it takes more than 20000 seconds. As the PCM melts, the solid part tends to reach a homogenous temperature equal to the phase change one. What is more, as the solid domain decreases, the melted PCM starts to stratification, which makes the natural convection heat transfer slower, because the fluid flow tends to become steady, since the mixing and, consequently, the recirculation diminish.

4.5 Conclusions

Figures 4.18 and 4.19 show an ulterior comparison between the three models. Figure 4.18 represents the cooling energy stored and released with time during charge and discharge according to three models. Concerning the charge, the three curves have the same behaviour and are very similar. On the other hand, the discharge plot shows no relation at all between the three curves: the three models model free convection in different ways, so after 2 h, when it starts to play a relevant role, the curves detach from each other. Figure 4.19 shows how the fraction of liquid volume changes over the two transients according to the models. In the charge plot, the 3D enthalpy porosity and the moving boundary methods have a similar behaviour, while the curve relative to the 2D enthalpy porosity model differs from them. Regarding the discharge, the three curves do not show any kind of agreement. Since the moving boundary method takes as initial values the results from the 2D enthalpy porosity method at a certain time-step, the liquid fraction is different already from the beginning, because it is defined in different ways in the two models. Among the three different method implemented in Comsol for the solidification and melting of a cylinder of PCM for cooling applications, the one that fitted as much as a possible with the experimental results, is the 2D enthalpy porosity method. What is more, this method is also less computational expensive than the other two, but it requires multiple attempts in order to obtain the optimal set of parameters that gives the best results. The 3D enthalpy porosity model is highly non-linear and it does not allow to exploit the axial-symmetry, therefore it results being too computational expensive, requiring also multiple runs to find the best combination of parameters. Furthermore its

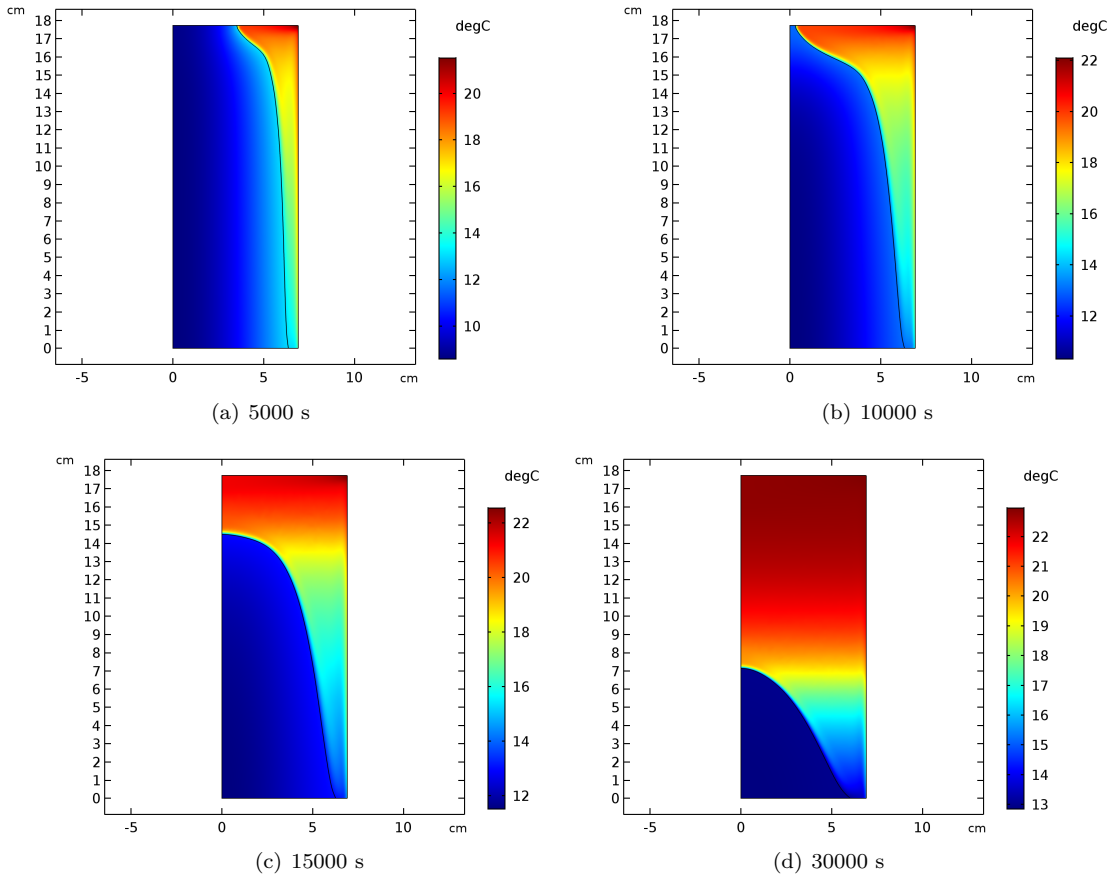

Figure 4.17. Moving boundary method: temperature profile evolution during discharge

non-linearity forces to use an apparent viscosity, otherwise it would not converge. Concerning the moving boundary method, it presents many difficulties. The most relevant is that it does not allow topological changes, so some numerical tricks are necessary to complete the simulations. Moreover this method didn't provide the expected results, probably because the material melts or crystallize over a larger temperature range. In a future work, it would be a good idea to try a hybrid model: divide the latent heat in two parts and modelling one with the enthalpy method and the other one with the moving boundary method.

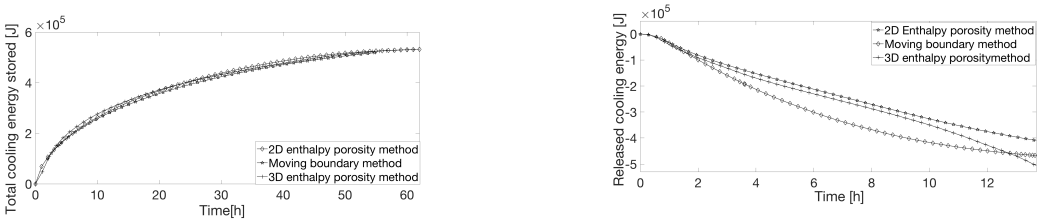

(a) Charge (b) Discharge

Figure 4.18. Cooling energy stored and released during charge and discharge according to three models

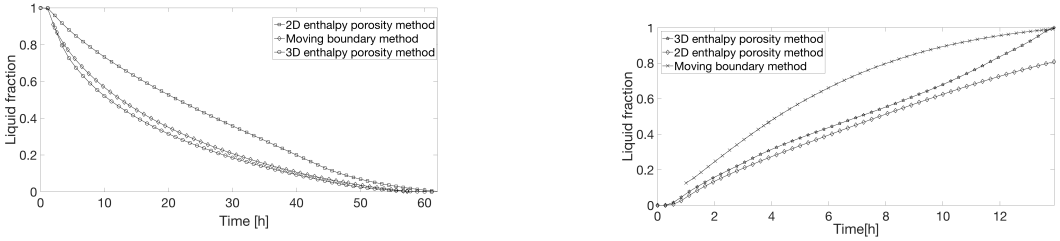

(a) Charge (b) Discharge

Figure 4.19. Evolution of the fraction of liquid volume during charge and discharge according to three models

Chapter 5

Experimental test and numerical model of a fatty acid PCM

5.1 Description

This chapter reports an experimental test carried on in a climatic chamber, with a PCM having a melting temperature of $68°C$. This material is therefore interesting for solar thermal applications, thanks to its phase change temperature, attractive especially for heating and domestic hot water systems. The PCM is a commercial fatty acid, white when it is solid and colourless when liquid. Figure 5.1 shows how the solid flakes of this material look like.

Figure 5.1. Aspect of the material at the solid state

5.2 DSC Analysis

Firstly, a differential scanning calorimetry (DSC) analysis is performed, in order to obtain some preliminary data about the melting temperature and the subcooling rate. Figure 5.2 shows the DSC measurement instrument. The analysis is firstly carried on with only the alumina pot, then it is performed also with the PCM inside of it. Therefore two DSC curves are obtained, but the corresponding one relative to the PCM is the difference between the second and the first one. This

operation is necessary, otherwise the results would be compromised by the presence of the alumina melting pot.

Figure 5.2. DSC analysis set up

Starting from $50°C$ the DSC analysis is characterized by eight phases, four are relative to the melting, while the last four regard the solidification.

- heat the material from $50°C$ up to $60°C$ with a temperature rise of $1°C$ per minute
- keep the material at $60°C$ for 5 minutes
- heat the material up to $85°C$ with a temperature rise of $1°C$ per minute
- keep the material at $85°C$ for 5 minutes
- cool the material down to $60°C$, with a temperature variation of $1°C$ per minute
- keep the material at $60°C$ for 5 minutes
- cool the material down to $50°C$, with a temperature variation of $1°C$ per minute
- keep the material at $50°C$ for 5 minutes

The tool measures continuously the temperature and the net thermal power absorbed or released by the material. Figure 5.3 shows the curve relative to the DSC analysis , from which is possible to extract some important informations about the material. Firstly, the melting temperature is slightly higher than $68°C$, it is about $70°C$ indeed. On the other hand, the solidification temperature is about $66°C$, which means that there is a subcooling of 4 degrees. All the physical properties are now known and are summarized in Table 5.1.

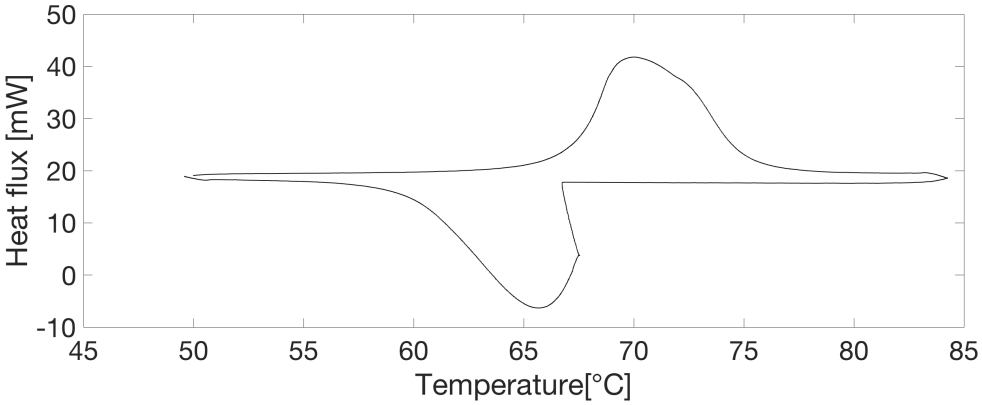

Figure 5.3. DSC analysis

Property	Value
Melting temperature	70° C
Solidification temperature	$66°C$
Latent heat	213kJ/kg
Thermal conductivity	0.25-0.15 $WK^{-1}m^{-1}$
Density	960-870 kg/m^3
Specific heat	1850-1910 $Jkg^{-1}K^{-1}$
Viscosity	0.00365 $Pa \cdot s$
Isobaric expansion coefficient	0.0003085 $1/K$

Table 5.1. Properties of the tested PCM

5.3 Climatic chamber experiment

5.3.1 Setup of the experiment

A cylindrical aluminium bottle with an outer diameter of 9 cm and a thickness of 1 mm is partially filled with the PCM and subjected to a complete charge/discharge cycle. The PCM was first in form of flakes, so before the experiment, it was necessary to melt it down and to solidify it, in order to let it become a continuous medium. The amount of PCM chosen for the experiment is a result from the analysis of the maximum pressure that the air in the cylinder would reach. In fact, firstly, the PCM is solid, but then it melts and the volume occupied by it increases, while the air volume decreases. For this reason, the air gets compressed. The maximum air pressure is obtained from the law of perfect gases:

$$P_{max} = \frac{P_{min} V_{max} T_{max}}{V_{min} T_{min}} \tag{5.1}$$

where P_{min} is the minimum air pressure during the experiment, which is the atmospheric one, V_{max} and V_{min} are respectively the maximum and minimum volumes of air inside the bottle,while T_{max} and T_{min} are the maximum and minimum temperatures. The air volume depends on the mass of PCM and on the volume of the entire bottle.

$$V_{min} = V_{bott} - \frac{m_{PCM}}{\rho_l} \tag{5.2}$$

$$V_{max} = V_{bott} - \frac{m_{PCM}}{\rho_s} \tag{5.3}$$

where ρ_s and ρ_l are the solid and liquid densities,m_{PCM} is the mass of PCM and V_{bott} is the volume of the entire bottle. In order to avoid internal pressures too large in the practical applications of macro-encapsulated system, the maximum pressure was fixed to 1.7 bar. Since the bottle volume is 1.06 lt, the hypothesized maximum and minimum temperatures are 80 $°C$ and $20°C$, the resulting mass of the PCM that guarantees a maximum pressure of 1.7 bar is 764 g. This corresponds to a maximum liquid volume of 0.88 lt. Since the inner radius of the bottle is 4.4 cm, the maximum height of the PCM cylinder, when it is fully liquid, is equal to 14.4 cm. Although 1.7 bar is not a large pressure, the aluminium container is very thin, so it was decided to make a hole in the clug, to keep the bottle at the ambient pressure and avoid a possible break-down. A second hole was made to let the thermocouple inside the container. Its tip is fixed at 6 cm from the bottom of the bottle. Another thermocouple is put inside the climatic chamber to measure the air temperature. The thermocouples are controlled by the Real Time controller cRIO 9024. Through a Labview application,shown in Figure 5.5, the thermocouples are controlled and set to take one measure every second. The PCM must be firstly melted down to let it become a continuous medium. Once

the PCM is melted, the climatic chamber is programmed with its own controller, by setting six different steps:

- 30 min ramp from about $70°C$ to $80°C$
- 4 hours at $80°C$
- 1 hour ramp from $80°C$ to $50°C$
- 48 hours at $50°C$;
- 1 hour ramp from $50°C$ to a set-point temperature of $80°C$;
- 24 hours at $80°C$.

The first two steps are necessary only to bring the PCM at a uniform temperature, before the discharge process begins. As a consequence they will not simulated by the numerical model. In order to keep the bottom surface adiabatic, the bottle is leaned over a thick layer of insulant material, as shown in Figure 5.4(b).

(a) (b)

Figure 5.4. Climatic chamber

5.3.2 Results

The results of the experiment are presented in Figure 5.6 and 5.7. Charge is faster, due to a stronger natural convection, while the discharge is slower, because all the effects of natural convection are concentrated at the beginning of the transient. Concerning charge, the measurement point, takes

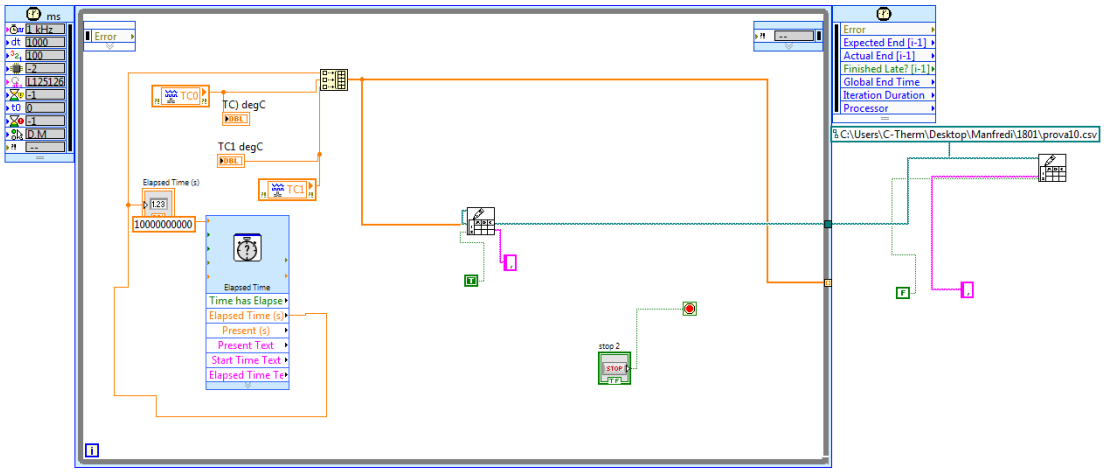

Figure 5.5. Block diagram of the Labview application

approximately 9 hours to reach the air temperature. As a consequence, the whole bottle will take slightly more time to reach thermal equilibrium. In the discharge, the PCM takes between 12 and 14 hours to reach thermal equilibrium. It must be said that there is a measurement error visible in Figure 5.6: according to the thermocouples, the PCM reaches a slightly higher temperature than air. On the other hand, the error is small and within the temperature accuracy range for this type of thermocouples. What is more the temperature reached by the air is higher than chosen the set-point, which is probably associated to a measurement error made by the climatic chamber sensors. The results of the discharge are different than what expected. In fact, the temperature of the measured point stays at $70°C$ for about 7 hours. This would let suggest that the solidification temperature is 70°, but the DSC analysis proved that it is instead equal to $66°C$.

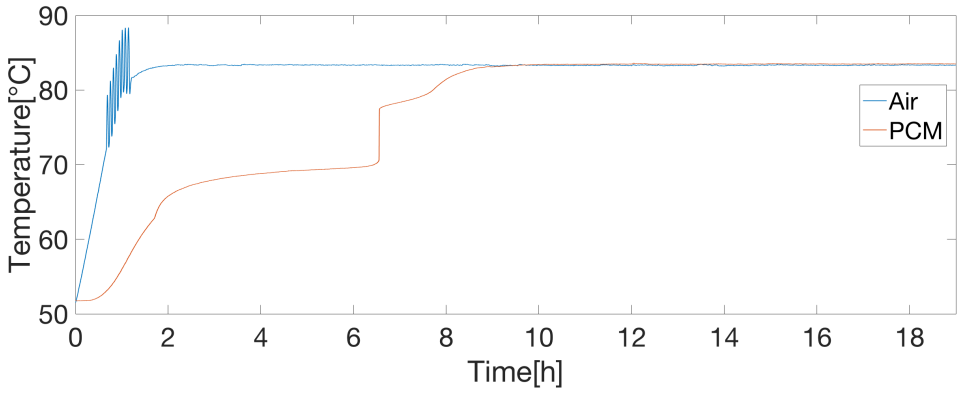

Figure 5.6. PCM temperature during charge

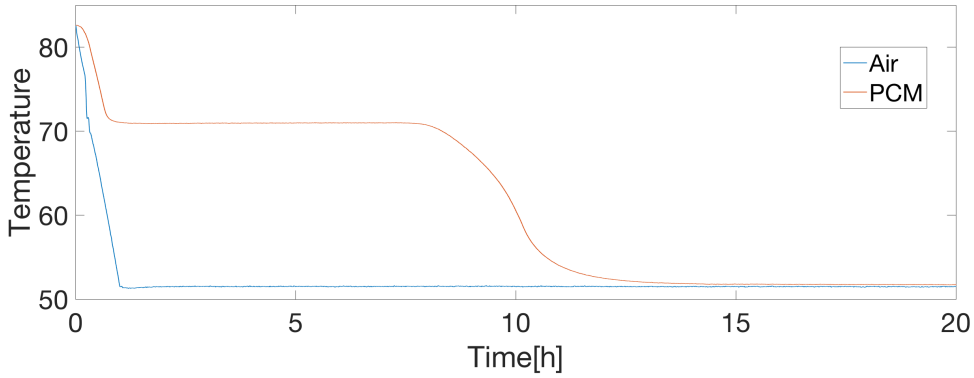

Figure 5.7. PCM and air temperature during discharge

5.4 Numerical model

Among the three methods tested in chapter 4, the most accurate to model phase change is the enthalpy method with the apparent viscosity. Therefore, it is again used to simulate the current experiment. The fluid flow is therefore considered as incompressible, laminar and Newtonian with a viscosity dependent on the mushy zone according to Eq. (4.8) and Eq. (4.9). Heat transfer equation is modelled with the enthalpy formulation and the liquid fraction is defined through a double derivable Heaviside function recalled in COMSOL by the command " flc2hs". Specific heat, thermal conductivity and density are considered constant and equal to the average value, which is still a good approximation, because the difference between the two phases is not too large. Consequently the geometrical quantities of the model are computed in such a way that the mass of PCM is the same of the real experiment. The geometrical parameters are then summarized in Table 5.2.

Volume[lt]	0.84
Radius [cm]	4.4
Height [cm]	13.7

Table 5.2. Geometrical values

5.4.1 Boundary conditions

On the axis there is a symmetry boundary condition for both heat transfer and laminar flow physics. On the lateral and bottom surfaces a no-slip condition is applied, since they are the physical walls of the aluminium recipient. The upper boundary is a free surface in contact with air, therefore it is modelled with zero velocity and zero shear stress. The bottom and the top surfaces are adiabatic, while the lateral one is invested by the air flux of the climatic chamber. As a consequence a Robin boundary condition is considered on the outer surface and the air temperature is the one measured by the thermocouple and imported in Comsol through a text file. The air velocity is 3.3 m/s, already measured in previous works [37]. This allows to obtain the heat transfer coefficient by the empirical correlation for cylinders in cross flow, where the characteristic length is the height of the cylinder, since it is in a vertical position [38]. The resulting heat transfer coefficient is 29 $W/m^2/K$. The initial condition for the charge is zero velocity everywhere and a homogeneous temperature of 51.7°C. For the discharge, velocity is also equal to zero, while the temperature is

homogeneous and equal to $82.57°C$, which is the measured temperature of PCM at the end of the charge. A physics-controlled mesh is built with normal size of the elements.

Chapter 6

Results

In this chapter, the results of the simulations are presented. Firstly, a tuning of the empirical parameters was needed in order to obtain numerical curves closer to the experimental results. These parameters are the melting temperature, the interval of the mushy zone and the mushy zone constant. They are different in the two cases of charge and discharge, therefore it is not possible to use a single model to simulate the whole experiment with the maximum accuracy. Instead two different simulations are needed. A trade-off set of parameters is needed if one wants to simulate with only one model both charge and discharge. The mushy zone was varied between 100 and 10000 for both charge and discharge, while the ΔT taken in consideration were between 1 and 5 K for the discharge and between 2 and 6 K for the charge. The best results are obtained with the set of parameters of Table 6.1.

Parameter	Charge	Discharge
$T_m[°C]$	72	70
$\Delta T[K]$	4	1
C	$10^{3.1}$	10^3

Table 6.1. Best set of parameters

6.1 Charge

Figure 6.1 shows the comparison between the experimental and numerical results for the charge case. The curves are very similar and the numerical model shows good agreement with the experimental results over the whole charge. The temperature profile and vorticity magnitude at four time instants are presented in Figures 6.2 and 6.3. The effects of natural convection are visible in both figures. In fact, as the PCM starts to melt, the liquid at higher temperature goes up and the phase front starts to move in two dimensions, while still keeping the axial-symmetry, which only depends on the geometry. The vorticity magnitude maps show higher values close to the outer surface. In fact, this area is in contact with the convective heat flux from the climatic chamber, therefore it is highly subjected to natural convection, because fluid particles on the bottom are heated and go to the top of the recipient, causing a strong mixing in this entire region. Smaller values of vorticity, but still larger than zero are present also close to the phase front, due to the large velocity and thermal gradients in the fluid domain close to it. As the material continues to melt, mixing decreases and the liquid starts to stratify, therefore heat transfer due to natural convection is stronger in the first hours. The amount of energy stored with time and the evolution

of volume liquid fraction are shown in Figures 6.4 and 6.5. The total amount of stored heat is about 0.21 MJ and it takes about twelve hours to completely melt the whole bottle of PCM.

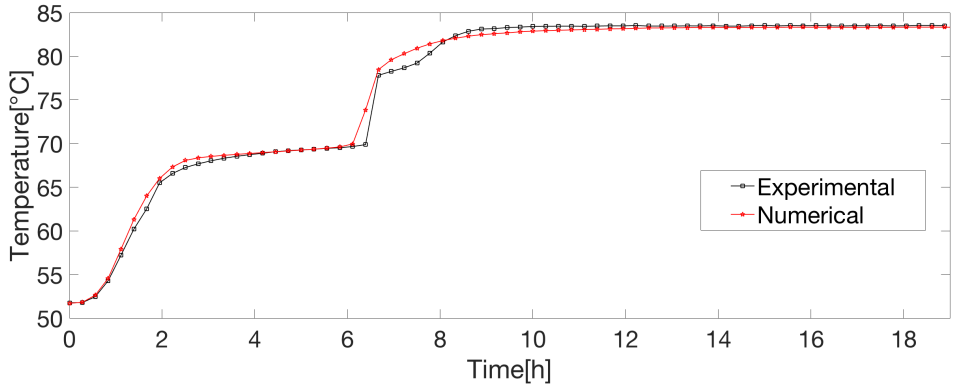

Figure 6.1. Temperature variation during charge on the axis at 6 cm from the bottom: experimental and numerical curves

6.2 Discharge

The experimental results showed an odd behaviour of the PCM during the solidification. The phase change temperature seems to be about $70°C$. This was totally unexpected, because usually the material presents a subcooling, due to the kinetics of the solidification, which was also visible in the DSC analysis. For the numerical model, therefore it was considered a $T_m = 70°C$. Figure 6.6 shows the comparison between numerical and experimental curves. They are very close and similar to each other. On the other hand, at the end of solidification, after 9 h there is a clear numerical error in the solution , since the temperature is larger than in the previous sampling time-step. The thermal profile and the vorticity magnitude evolution are showed in figures 6.7 and 6.8. Due to natural convection, the lower part is the first to solidify. Since, the PCM close to the outer surface is solid, vorticity is null in that region, instead the maximum values appear in the mushy zone. What is more, vorticity decreases rapidly, which is congruent with the heat transfer ratio, that is larger at the beginning, due to stronger natural convection caused by the continuous mixing of the liquid phase. As the material crystallizes, the resistance to the fluid flow increases, mixing decreases and consequently also vorticity and heat transfer.

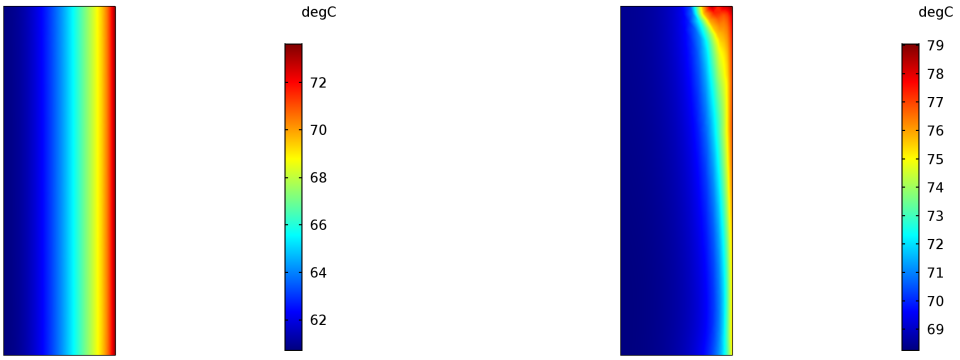

(a) 5000 s

(b) 10000 s

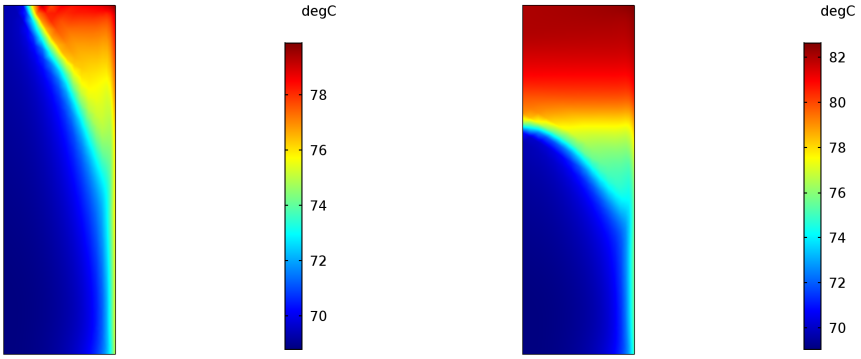

(c) 15000

(d) 20000 s

Figure 6.2. Evolution of the temperature profile during charge

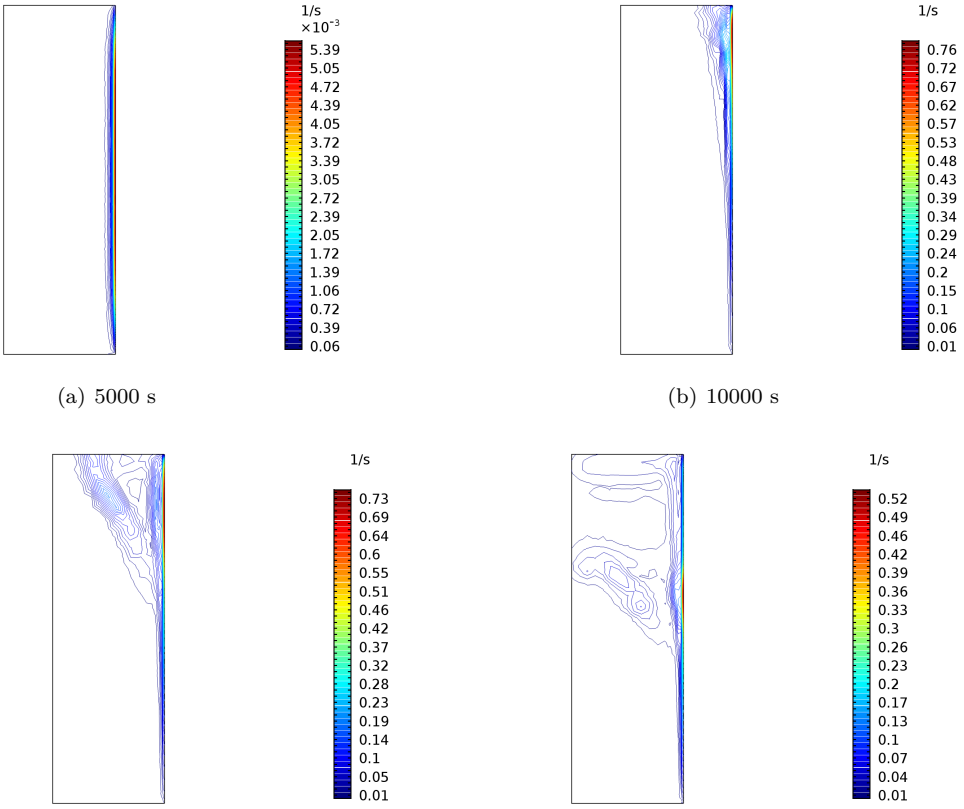

(a) 5000 s

(b) 10000 s

(c) 15000

(d) 20000 s

Figure 6.3. Evolution of vorticity[1/s] during charge

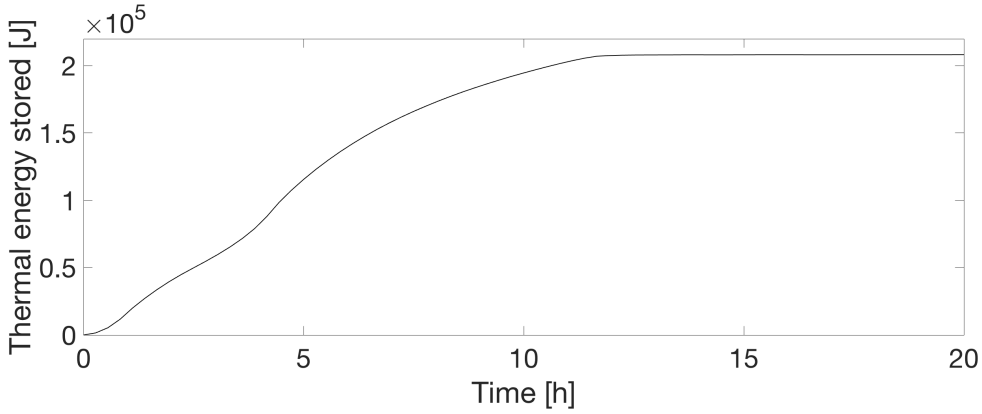

Figure 6.4. Thermal energy stored with time

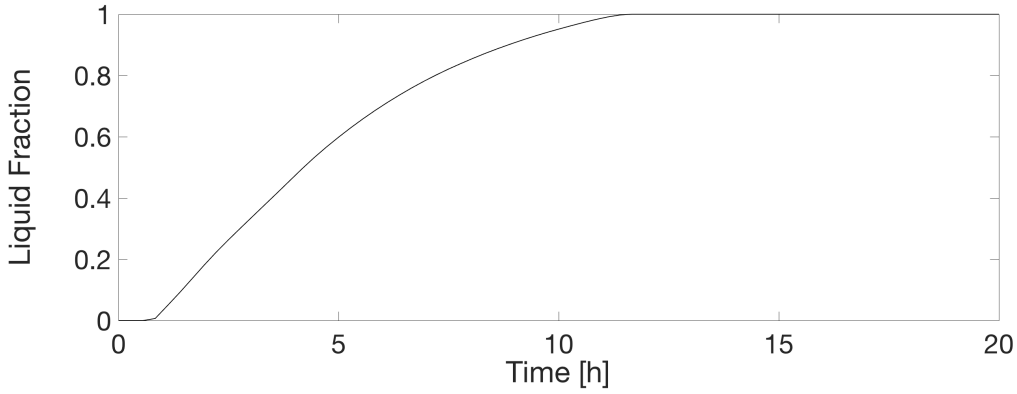

Figure 6.5. Evolution of liquid fraction with time during charge

Figures 6.9 and 6.10 show the heat released during the discharge and the evolution of the volume liquid fraction. The time to complete solidification and discharge is very similar and it is about 12 hours.

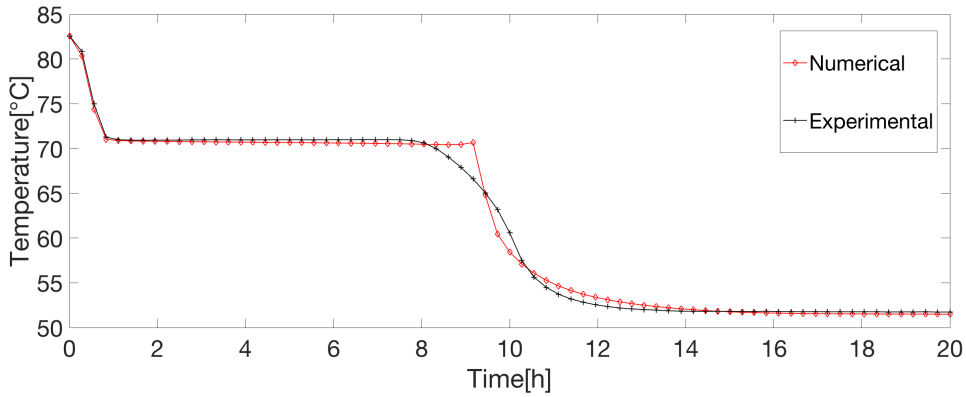

Figure 6.6. Temperature variation during discharge at the point of coordinates (0,6 cm): comparison between numerical and experimental results

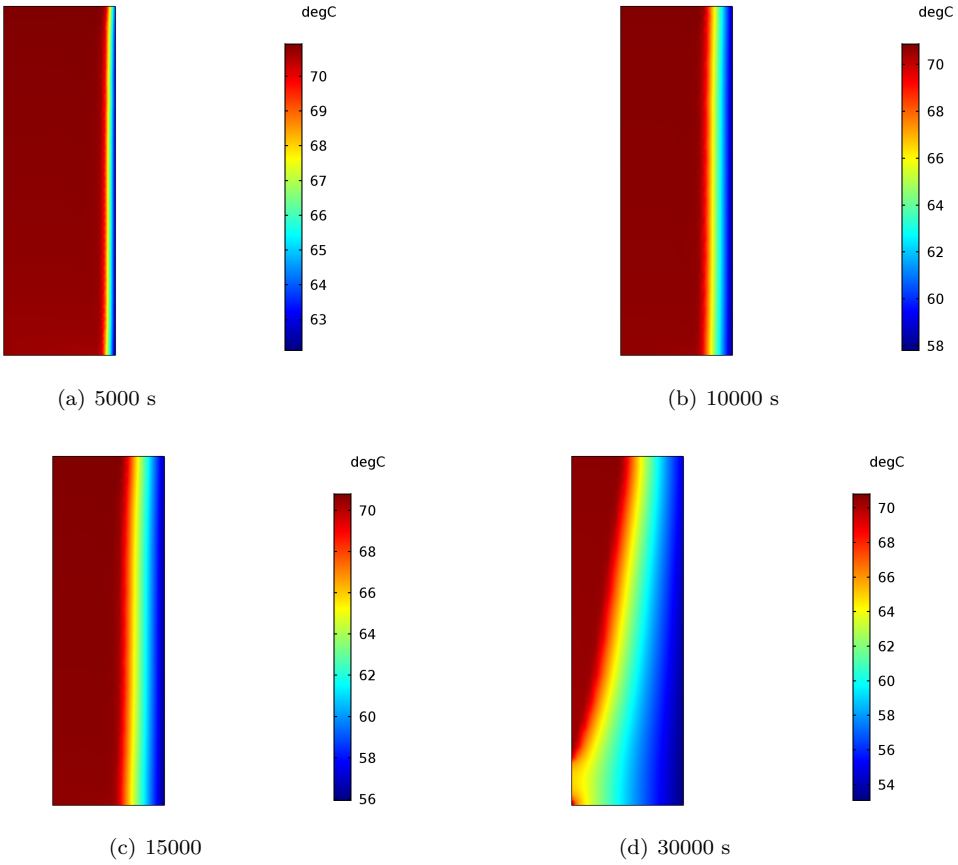

(a) 5000 s

(b) 10000 s

(c) 15000

(d) 30000 s

Figure 6.7. Evolution of the temperature profile during discharge

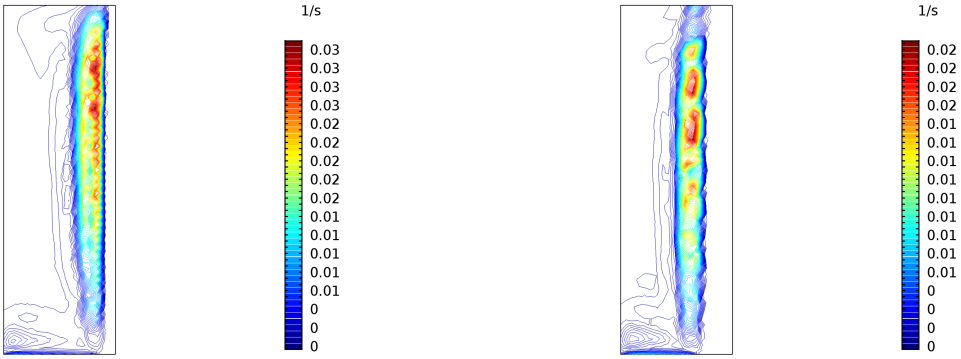

(a) 5000 s (b) 10000 s

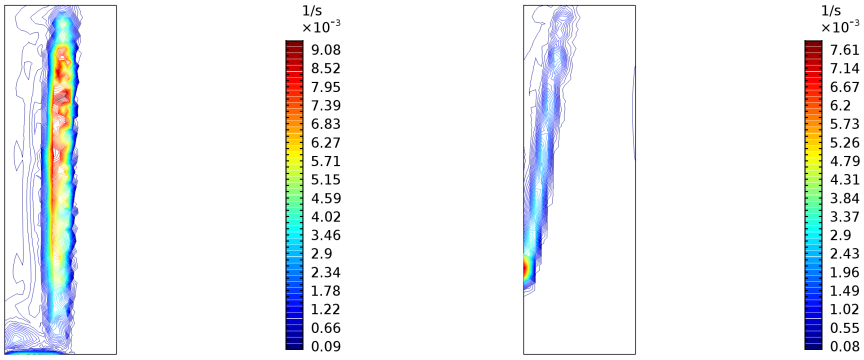

(c) 15000 (d) 30000 s

Figure 6.8. Evolution of vorticity[1/s] during discharge

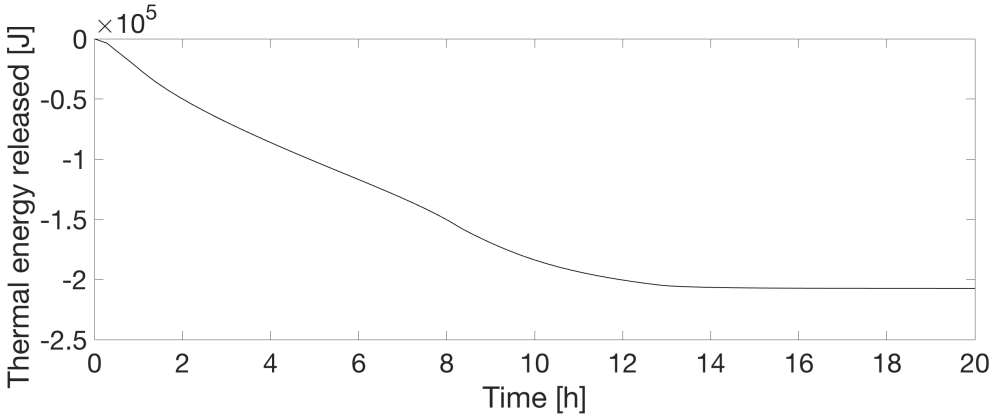

Figure 6.9. Heat released with time during discharge

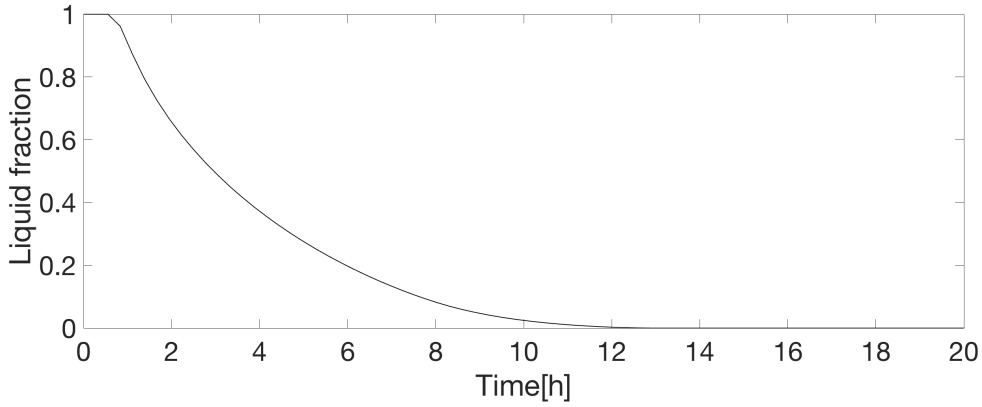

Figure 6.10. Evolution of liquid fraction during discharge

6.3 Statistical analysis

Three statistical parameters are calculated in order to judge the accuracy of the model. These are the mean bias error MBE, the mean absolute error MAE and the coefficient of determination R^2, calculated according to the following equations:

$$MBE = \frac{1}{N}\sum_{i=1}^{N}(T_{num}^{i} - T_{exp}^{i}) \tag{6.1}$$

$$MAE = \frac{1}{N}\sum_{i=1}^{N}\left|T_{exp}^{i} - T_{num}^{i}\right| \tag{6.2}$$

$$R^2 = 1 - \frac{\sum_{i=1}^{N}(T_{exp}^{i} - T_{num}^{i})^2}{\sum_{i=1}^{N}(T_{num}^{i} - T_{exp,mean})^2} \tag{6.3}$$

where T_{num}^{i}, T_{exp}^{i} are the numerical and experimental temperatures at the i_{th} time-step. $T_{exp,mean}$ is the average experimental temperature. The parameters are calculated and summarized in Table

6.2, which shows good agreement with the experimental results, as it was already observed in the previous plots.

Parameter	Charge	Discharge
MBE[K]	0.1048	-0.0099
MAE [K]	0.4363	0.4771
R^2	0.9939	0.9929

Table 6.2. Statistical parameters computed for the two best cases

6.4 Effects of the empirical parameters: sensitivity analysis

In this section, the effects of the empirical parameters on the numerical solution are analysed. The optimal set of parameters differs in charge and discharge and the effect of the variation of the parameters is different in the two cases. This is due to the fact that they are characterised by different kinetics phenomena. In fact, the DSC analysis showed two different curves for heating and cooling. As a consequence, it is not surprising that the mushy zone constant and the melting temperature interval differ from charge to discharge. The mushy zone temperature interval can not be too small, otherwise there would be numerical convergence issues. With a small ΔT, in fact, the enthalpy variation with temperature is too steep in the mushy zone and very small time-steps are needed to guarantee convergence, which leads to higher computational cost. Furthermore, with a small ΔT, the temporal temperature curves are sharper close to the flex points, which delimit the beginning and the end of phase transition, but at the same time the phase change is almost isothermal, therefore the curve is almost flat in correspondence of it. On the other hand, if the ΔT is too large, the results become inaccurate, because the phase change would be far from being isothermal and in the time-temperature curve, the phase transition region would present a certain inclination, while the curves would be softer close to the flex points. The effects of the ΔT width of the mushy zone are shown in Figures 6.11 and 6.12, where the melting temperature and the mushy zone constant are fixed, while the ΔT is kept constant. In Figure 6.11 a ΔT of 6 K anticipates too early the flex points. What is more, it tends to underestimate the temperature during phase transition in the time comprised between 2 and 5 hours of the transient. With a ΔT of 2 K, phase transition starts and ends later, while the temperature is overestimated over the whole phase change period. What is more, with this choice of the parameter, phase transition occurs almost isothermally, but the experimental results showed a certain inclination of the temporal temperature curve during the phase change. For these reasons a ΔT of 4 K is the one that better models the mushy zone of this material. The experimental results showed that the phase change for the discharge is almost isothermal, but with this numerical method it is impossible to reach a perfect isothermal phase change. Instead a mushy zone temperature interval must be defined. Since a too small ΔT would create numerical issues, it was decided to use a $\Delta T = 1K$ and the results obtained with it are really close to the experimental ones. With smaller mushy zones temperature intervals , the results would be probably more accurate, but the computational time would become too large. Instead, with higher values, for instance $\Delta T = 3K$ and $\Delta T = 5K$, the curves are much smoother and the phase transition begins and finishes earlier if compared with the experimental results.

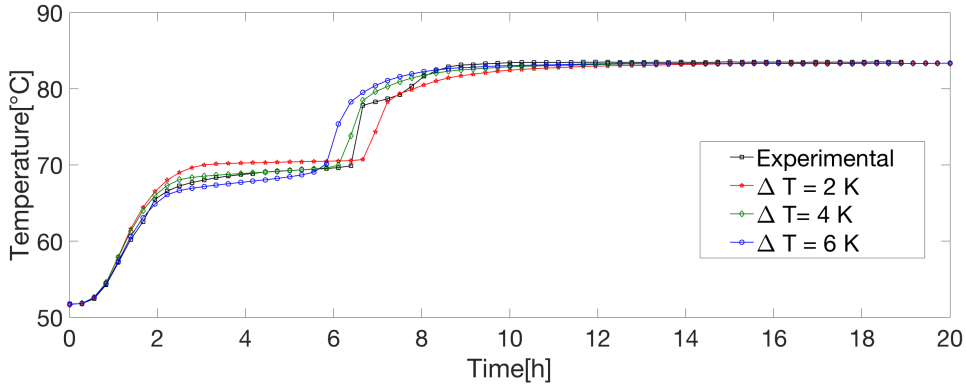

Figure 6.11. Charge: effects of the mushy zone temperature interval on the results

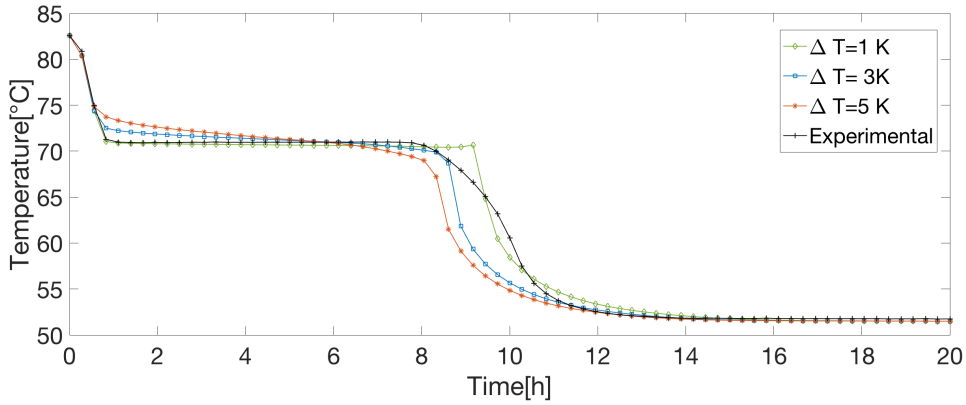

[h!]

Figure 6.12. Discharge: effects of the mushy zone temperature interval on the results

The effect of the mushy zone constant is to contrast or promote natural convection in the mushy zone. In fact, by increasing this constant, the apparent viscosity in the mushy zone increases. This means that the PCM is forced to extremely low velocities for small values of liquid fraction. From an energetic point of view, the material starts to change phase once it gets in the mushy zone, but the effects of natural convection appear later at higher temperatures, corresponding to liquid fractions closer to one. This is shown in Figures 6.13 and 6.14, which present the plots obtained by varying the mushy zone constant and keeping the ΔT and T_m constants. In both plots a larger C causes an increase of the time needed to complete the phase transition. On the other hand, in the charge simulations the results are more sensible to the value of this constant. In fact, with a $C = 10^4$ the time to complete the charge is about 4 hours longer than with a $C = 10^{2.6}$. During the cooling phase , the C influences the time to complete the phase transition, but the time to end the whole discharge is only slightly longer. In fact, with a larger C, the curve is sharper after the solidification is completed. The different influence of the mushy zone constant on the charge and discharge results is concordant with the stronger natural convection heat transfer during melting. In fact, during discharge most of the natural convection is concentrated in the first hours, when the PCM is fully liquid and therefore the mushy zone constant does not affect the results, because the apparent viscosity is equal to the real one of the liquid.

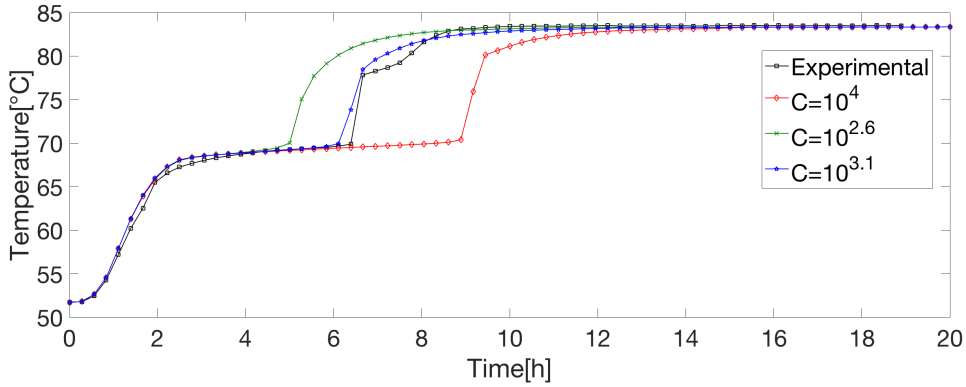

Figure 6.13. Charge: Effects of the mushy zone constant on the results

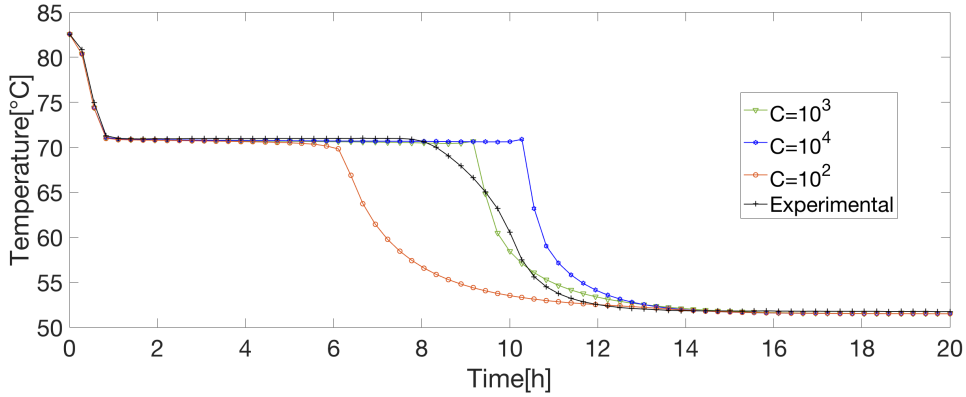

Figure 6.14. Discharge:Effects of the mushy zone constant on the results

6.5 Trade-off set of parameters

The best sets of parameters are different for charge and discharge. On the other hand, if it is requested to simulate a more complex system, it could be necessary to use only one set of parameters that is a trade-off for the two cases. It could happen, in fact, that a part of the PCM is subjected to solidification, while another one is melting. As a consequence, a new tuning is required to determine the set of parameters that better simulates both cases. The trade-off parameters are listed in Table 6.3. The results of the first 20 hours of the discharge and of the first

Parameter	Value
C	$10^{3.2}$
T_m	70
ΔT	2.5

Table 6.3. Trade-off set of parameters

19 hours of the charge are presented in Figures 6.15 and 6.16. The curves show some differences with the experimental results, but their behaviour is still similar. A statistical analysis has been

carried on as well and its results are summarized in Table 6.4. The computed statistical parameters demonstrate that the model is accurate even if the set of parameters is unique for both cases.

Parameter	Charge	Discharge
MBE	-0.2770	-0.0517
MAE	0.5182	0.5119
R^2	0.9942	0.9905

Table 6.4. Trade-off set of parameters

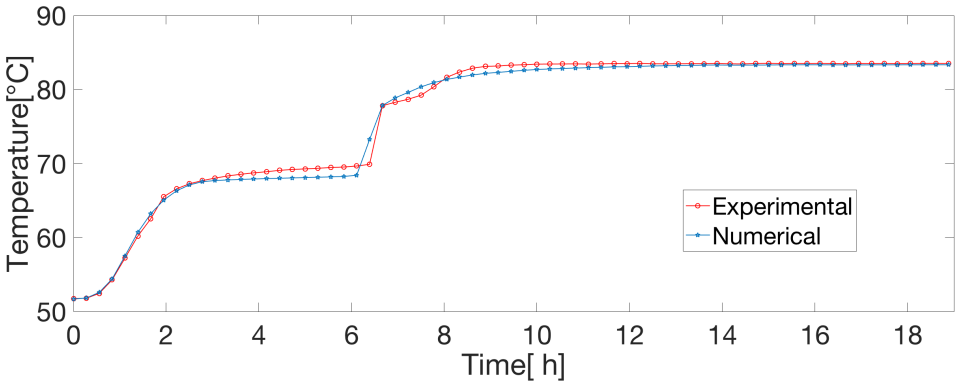

Figure 6.15. Charge temporal temperature curves obtained with the trade-off parameters

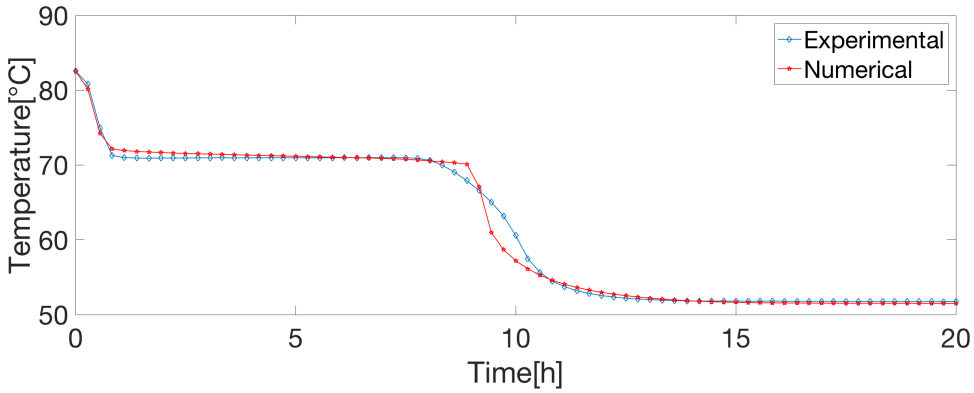

Figure 6.16. Discharge temporal temperature curve obtained with the trade-off parameters

Chapter 7

Water tank model

This chapter presents the development of a class of models for the simulations of charge and discharge of water tanks TES. In the first section, it is described the model for a water tank with an immersed coil, that alternatively charges and discharges the storage, while in the second part a similar model is presented for water tanks with two separated coils for charge and discharge. The models are implemented by means of Matlab and are both validated with experimental data. The numerical schemes used to solve the equations are the 1-D finite volumes for space discretization and the implicit backward Euler for time discretization to assure numerical stability.To avoid negative thermal gradients on the axis of the tanks, the reversion algorithm has been implemented in both models.

7.1 One-coil tank

Mongibello et Al. in 2017 [39] published a work about the implementation of a Simulink model for the simulation of water tank thermal energy storage with an immersed coil and validated it through an experimental test. In this thesis work a similar model has been implemented and validated through the same experiemntal results, as a starting point for a new model with two coils. The difference is that this one is fully implemented on Matlab instead of Simulink, however the equations and the approach are the same. This coil is characterized of two parts: a vertical one in the upper region of the tank and one inclined by 25 degrees in the lower region. The tank is not perfectly cylindrical, because of the presence of the two spherical ends, but it has been considered as a cylinder by assuming a different height in such a way that the total volume stays unchanged. Figure 7.1 shows the sketch of the water tank, while the parameters of the modified tank geometry are summarized in Table 7.1. The inlet and outlet sections of the coil are respectively placed at

Number of spires	13
Coil outer diameter	0.0334 m
Coil internal diameter	0.0301 m
Coil total length	18.1 m
Tank diameter	0.65 m
Tank height	1.27 m
PU foam layer thickness	0.05 m

Table 7.1. Geometrical parameters of tank and coil

0.73 m and 0.28 m from the bottom of the tank, so the heat transfer fluid enters from the higher

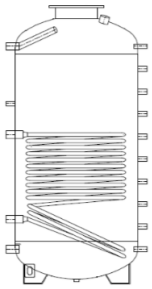

Figure 7.1. Sketch of the water tank without insulation

section and exits from the lower one in order to maximise the heat transfer with the water in the tank. The experiment is 5244 seconds long and concerns the charge phase of the TES. The heater circuit is characterised by a pump, controlled by a PID controller and an electrical heater. The mass flow of the heat transfer fluid in the heating circuit is set to 0.37 kg/s, while the temperature of at the inlet section of the coil starts from $20°C$ and arrives at more than $70°C$. The curve "inflow temperature vs time" is shown in Figure 7.2. The coil and the water tank are modelled

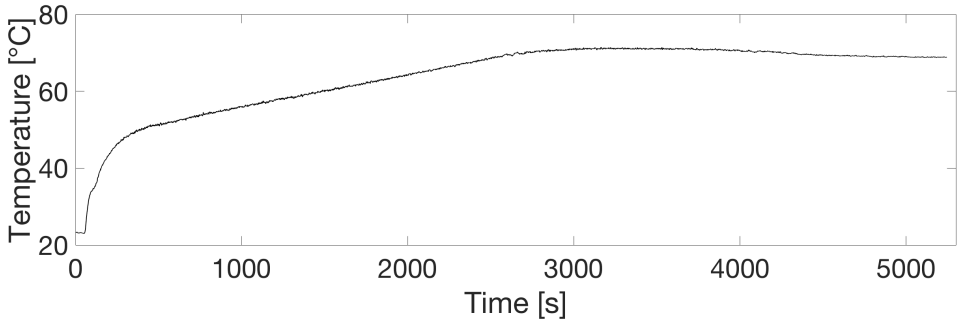

Figure 7.2. Inlet temperature of the heat transfer fluid

separately with 1D finite volumes , but since the systems are dependent, to solve the equations an iterative procedure is needed. The discretization for the tank is done on the vertical direction, while for the coil is done along its length. The discretization of the coil is dependent on the one of the tank, because for every node of the coil only one tank node must correspond. For every node of the coil at each time-step, the following equation is solved:

$$\rho c_p \frac{T^n_{coil,i} - T^{n-1}_{coil,i}}{\Delta t} = \frac{T_{tank,j} - T_{coil,i}}{R_{coil,i}} + \dot{m} c_p * (T^n_{coil,i-1} - T^n_{coil,i}) \tag{7.1}$$

where the subscript "i" refers to the ith node of the coil, while the subscript "j" refers to the corresponding node of the tank and $R_{coil,i}$ is the thermal resistance between the heat transfer fluid and the tank along the ith control volume of the coil. The up-scripts "n" and "n-1" refer to the present and previous time-step $\dot{m}$ is the mass flow and Δt is the width of each time step. The convective term is computed through the upwind scheme to guarantee numerical stability and limit the fluctuations to the solution. The following equation solves the water temperature inside the

tank at each node:

$$\rho c_p \frac{T^n_{tank,k} - T^{n-1}_{tank,k}}{\Delta t} = \sum \frac{T_{tank,k} - T_{coil,i}}{R_{coil,i}} + Q_{cond} + 1/R_{tank,k} * (T_{amb} - T^n_{tank,k}) \tag{7.2}$$

where "k" refers to generical kth node of the tank, $R_{tank,k}$ is the thermal resistance between the kth control volume and outer environment. Due to the presence of the inclined part of the coil, for some nodes of the tank, multiple coil nodes may correspond. For this reason one node of the tank is subjected to heat transfer with multiple coil nodes,therefore in the equation their sum is taken into account. Q_{cond} is the diffusive heat transfer between adjacent volumes and computed through central differences scheme.

$$Q_{cond} = \lambda \frac{T^n_{i+1} - 2T^n_i + T^n_{i-1}}{\Delta x} \pi D^2/4 \tag{7.3}$$

where λ is the water thermal conductivity, Δx is the length of a control volume and D is the diameter of the tank. The thermal resistance between the coil and the water tank is the sum of the internal thermal resistance between the heat transfer fluid and the coil inner wall, the conductive thermal resistance of the coil and finally the outer convective thermal resistance between the coil outer wall and the water tank.

$$R_{coil} = \frac{1}{h_i * A_i} + \frac{1}{h_{out} * A_{out}} + \frac{log(A_{out}/A_i)}{2 * \pi * L * \lambda} \tag{7.4}$$

where h_i and h_{out} are respectively the internal and outer heat transfer coefficients,A_i and $A_o ut$ are the heat transfer areas, λ is the thermal conductivity of the coil material and L is the total length of the coil. The internal heat transfer coefficient is computed through the Gnielinski correlation [40]:

$$Nu_{int} = 3.65 + 0.08 * (1 + 0.8 * (d/D)^{0.9}) * Re^m * Pr^{0.333} * (Pr/Prw)^{0.14} \tag{7.5}$$

where d is the tube diameter,D is the helix diameter, Re is the Reynolds number calculated considering the tube diameter as characteristic length, Pr is the Prandtl number and Prw is the Prandtl number at the wall temperature. The internal heat transfer coefficient is then computed as follows:

$$h_i = \frac{Nu_{int}\lambda}{d} \tag{7.6}$$

The outer heat transfer coefficient is computed with the Ali [41] and Prabhanjan [42] correlations for helical coiled tubes.

$$Nu_{out,Ali} = 0.106 * Ra_L^{0.335} \tag{7.7}$$

$$Nu_{out,Prabhanjan} = 0.009759 * Ra_L^{0.3972} \tag{7.8}$$

where Ra_L is the mean Rayleigh number computed using the total coil length as characteristic length. The outer heat transfer coefficient is then calculated as follows:

$$h_{out} = \frac{Nu_{out}\lambda}{L} \tag{7.9}$$

Concerning the tank thermal resistance, the internal heat transfer coefficient is computed with the correlation for natural convection heat transfer on vertical walls, while the outer heat transfer coefficient is considered equal to 5 W/m^2K. However the most important term is the resistance of the foam layer, which has a conductivity equal to 0.025 W/mK, that highly insulates the tank from the outer environment. The ambient temperature is fixed to 23°C. Since these coefficients

depend on the tank and coil temperatures, which vary with time and are non-linearly dependent on each other, they need to be computed iteratively at each time-step. To take into account of the natural convection, that causes the movement of hotter water from the bottom to the top of the tank, the reversion elimination algorithm [43, 44] is implemented. This algorithm is applied at the end of each time-step, after the the tank and coils thermal profiles are both solved. Perhaps it could happen that the numerical solution involves negative thermal gradients on the tank axis, therefore the regression elimination algorithm updates the water tank temperature in the following way:

- starting from the bottom, for every node, if the next one is at the same or at higher temperature, nothing changes, while if it is at a lower temperature, then the two temperatures are updated to their mean.
- From the top, for every node, if the one immediately after is at a higher temperature, the two temperatures are updated to their mean.
- these two procedures are alternatively applied until convergence is reached

This method is really useful, because it is able to solve the thermocline of the tank, without solving the velocity field through the buoyancy term in the Navier-Stokes equations.

7.1.1 Results

The tank has been discretized with 100 nodes equidistant from each others. The discretization of the helicoidal coil is dependent on the one of the tank, because for each coil node, only one tank node must correspond. Concerning the time discretization, the time-step has been fixed to 1 s, which is also the experimental sampling time. The inlet temperature and the mass flow are inputs of the model, so they are considered as boundary conditions for the coil system and their data are directly extracted from the experimental results. The outlet section is considered as adiabatic, as also the bottom and top sections of the water tank. As initial condition, the tank and the heat transfer fluid are uniformly at the ambient temperature. The simulations are performed using both Ali and Prabhanjan correlations and the results change significantly. On the other hand, they are both validated by the experimental results, because the root mean square relative to the tank mean water temperature and to the outlet coil temperature is small for both cases, as it is shown in Tables 7.2 and 7.3. Figure 7.3 shows the comparison between the experimental thermal profile and the two ones computed numerically at three different time instants. The Ali's correlation predicts very well the profiles along the whole height of the tank apart from lowest part of the tank, where the numerical temperature is much lower than the experimental one. The Prabhanjan correlation shows also good agreement,but there is a slight difference visible both graphically and from the statistics. The reason for which there is a significant difference between the experimental and numerical results in the lowest part of the tank is linked to the fact that the mixing is weaker in this region, while the measurements are taken on the tank axis, which is at the maximum distance from the coil walls, which are instead at higher temperature. Therefore the thermal measurements in this area are taken in the coldest points of the relative sections. On the other hand, at the top of the tank, water is very well mixed, therefore the temperature is uniform and, in fact the numerical model predicts the temperature accurately in this area.

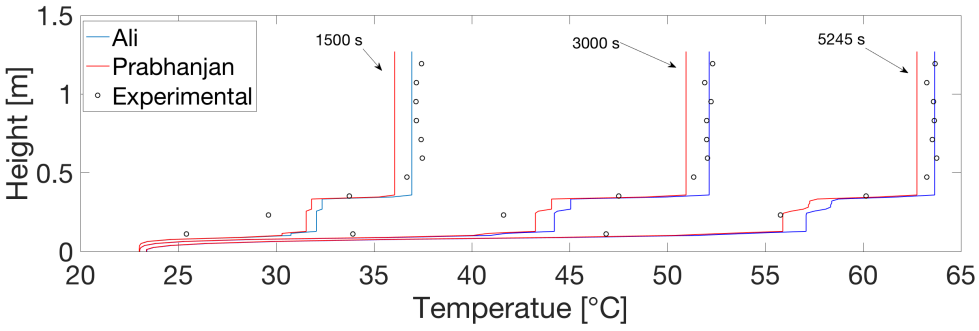

Figure 7.3. Temperature profile according to the two correlations at three different time instants

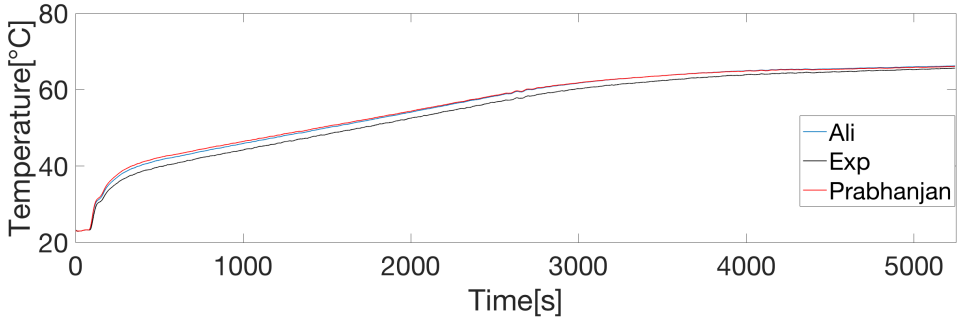

Figure 7.4. Evolution of the outlet coil temperature according to the two correlations and the experimental results

Correlation	RMSE[$°C$]
Ali	0.3576
Prabhanjan	1.068

Table 7.2. Root mean square error of the tank mean water temperature.

Correlation	RMSE[$°C$]
Ali	1.3376
Prabhanjan	1.5877

Table 7.3. Root mean square error of the coil outlet temperature.

7.2 Two-coil tank

The sketch of a tank with two separated coils for charge and discharge is presented in Figure 7.6. The characteristics of the tank are the same of the previous one , while the coils are different ,since they do not have the diagonal part. The lower one is the charge coil, while the upper one is the discharge coil. The heat transfer fluid enters warmer in the upper section and exits colder from the lower section of the charge coil, while for the discharge coil, the water enters from the bottom and exits from the upper section. This configuration is the best one to maximise heat transfer, since in this way the heat exchangers are characterized by countercurrent streams. The heat transfer(HTF) fluid that exits from the discharge coil is then directed to two fan-coils to

transfer the heat previously absorbed from the water tank storage to the user. After it is cooled down in the fan-coil, the HTF re-enters in the inlet section of the tank discharge coil. The pump control logic of the heating circuit is characterised by a cut in and a cut-off relative to the mean temperature of the tank. The cut-in temperature is $60°C$, while the cut-off is $80°C$, which means that the pump is switched on, when the tank mean temperature reaches $60°C$ and it is switched off, when it reaches $80°C$. The control logic of the user loop is based on the heat demand profile of a semi-detached house of 100 m^2, with an indoor set-point temperature of $20°C$. Figure 7.5 shows the whole system, characterized by two fan-coils, the electrical heater and the water tank thermal energy storage.

(a) Water tank

(b) Fan coils

Figure 7.5. Experimental facility

The experiment is three days long, but only the results of the third one are presented, because the system reaches a periodic condition after the second day. In the tanks there are nine thermocouples that measure the temperature at different heights on the axis. The problem is that there is no thermocouple below the charge coil, which means that thermocline that forms in the bottom part of the tank is not measured. For this reason, the energy variation in the tank is computed, by assuming that the bottom of the tank is at the temperature of the lowest thermocouple, while the top of the tank is at same temperature of the highest thermocouple.

7.2.1 Results

The mathematical model for this tank is very similar to the previous one, except that it is slightly more complex due to the presence of the second coil. On the other hand, the way the coils are discretized is exactly the same of the one-coil model, the difference stays in the coupling of the equations: more iterations are required to the reach the convergence. What is more in this model,

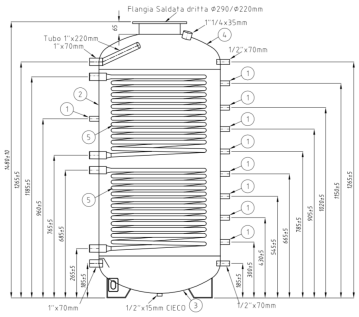

Figure 7.6. Sketch of the experimental water tank with two coils.

the inertia of the components is taken into account, because in some transients they play an important role. The tank has been discretized with 200 nodes, while the time-step is chosen equal to the measurement sampling time, which is not constant, but it is always around 1 second. For the forced and natural convection inside and outside the helicoidal charging tubes the Gnielisnki and Prabhanjan correlations have been considered. For the discharge coil , the Prabhanjan correlation tended to predict well the temperature in the coils, but not so accurately the temperature in the tank, therefore a new correlation was researched and found. Equation (7.10) presents the new correlation, in which the Nusselt number is dependent on the temperature difference with a quadratic law.

$$Nu_{ext} = 267.5567\Delta T^2 - 293.5599\Delta T \tag{7.10}$$

where ΔT is the temperature difference between the coil outer wall and the water inside the tank. Figure 7.7 shows the Nusselt number as a function of the temperature difference. In literature

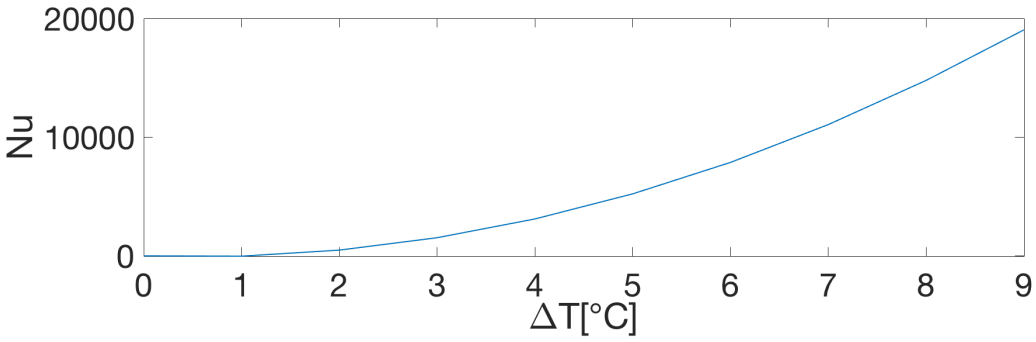

Figure 7.7. Nusselt number as function of temperature difference

the Nusselt number is function of the Rayleigh, which is not only function of the temperature difference, but depends also on the film temperature. For this reason a corresponding correlation can be computed for Nusselt function of Rayleigh, by considering a film temperature equal to 70°, which is approximately the mean temperature in the tank over the whole cycle.

$$Nu_{ext} = 1.0349 * 10^{-27} * Ra_L^2 - 5.7734 * 10^{-13} * Ra_L \tag{7.11}$$

The simulations are launched by using both versions of the correlation, but the first one is the most accurate, while the second one tends to underestimate the flux when the tank temperature

is below $70°C$. The results are obtained simulating three days of activity, in order to reach their daily periodicity, therefore only the results of the third days are taken into account in the statistics and in the plots. Figures 7.8-7.10 show the comparison between the numerical results obtained with both correlations and the experimental ones regarding the temperatures in the coils and in the tank. The shapes of the different numerical curve obtained with both Nusselt correlations are similar but differ when the temperatures are lower. As it was mentioned, the thermocouples do not measure the temperature in the bottom part of the storage, where there is a larger thermocline. For this reason, the comparison between the experimental and numerical results has been done only in the region of the tank comprised between the thermocouples. The curves relative to the outlet temperature of the charge coil are very close to the experimental one, except for the hours when the heating circuit is turned off. This happens because in those hours, the mass flow in the charge coil is close to zero, but the heat transfer fluid is not completely steady. In fact it flows slowly from colder part of the system to the inlet and outlet sections of the tank charge coil, where the thermocouples are placed. However in these hours, the heat transfer between the charging coil and the tank is negligible, due to the Reynolds number close to zero , so they are not of particular interest. Concerning the user coil, the results are also close to the experimental ones, but the temperature peaks are slightly larger. Overall the numerical temperatures of the heat transfer fluid in the coils are in good agreement with the experimental ones, on the other hand the model lacks of accuracy in the estimation of the water tank temperatures in the night-time.This could be explained by the fact that even small errors in the outlet temperatures of the coils produce larger errors in the exchanged thermal powers, because the experimental temperature difference between the inlet and the outlet is small. Therefore an error on the determination of the outlet temperature of few decimals of Celsius degree, actually produces a significant error. This can also be observed in Figures 7.12 and 7.13, that show the numerical and experimental results for the thermal power exchanged in the coils. Concerning the results obtained with the Nusselt dependent only on the temperature difference, these curves tend to follow quite well the experimental ones. On the other hand, with the Nusselt dependent on the Rayleigh number, the numerical model tends to underestimate the heat fluxes. This affects both charge and discharge coils result, while the shape of the tank energy variation curve in Figure 7.11 stays almost the same. Tables 7.4 and 7.5 report the statistical parameters relative to the temperature in the coils and in the tank, while table 7.6 7.7 report the statistics of the energy variation in the tank and the thermal power exchanged through the coils. Due to the fluctuations of the experimental results, all the statistics have been computed using a sampling time of 1000 s. As was already clear from the graph, the statistics show that the correlation dependent only on the ΔT, is more coherent with the experimental results. The determination coefficient relative to the power exchanged in the user coil is, in fact, 5% lower in the results obtained with the second correlation. On the other hand, the determination coefficients for the second correlation are still larger than 90%, except the one relative to the tank energy variation, which is lower than 90% also for the first correlation.

	MBE[$°C$]	RMSE[$°C$]	R2 [%]
Mean tank temperature	-0.8350	1.6154	92.21
$T_{out,u}$	-0.1	0.3676	99.67
$T_{out,g}$	-0.2397	0.3646	99.81

Table 7.4. Mean bias error, root mean square error and determination coefficient relative to the temperatures in the coils and in the tank according to the first correlation

Figure 7.14 shows the numerical and experimental thermal profile inside the water tank at three different time instants. The experimental thermal profiles do not present the thermocline at the bottom and at the top of the tank, because the thermocouples are placed too centrally.

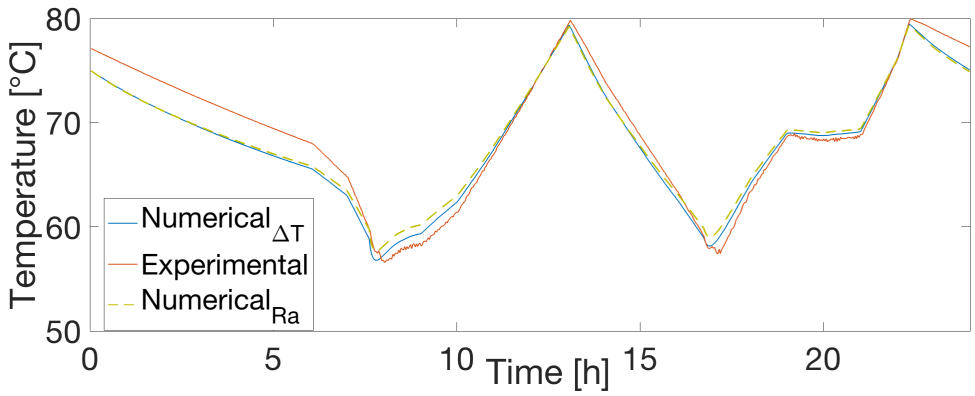

Figure 7.8. Numerical and experimental mean temperature of the water tank in the space between the nine thermocouples

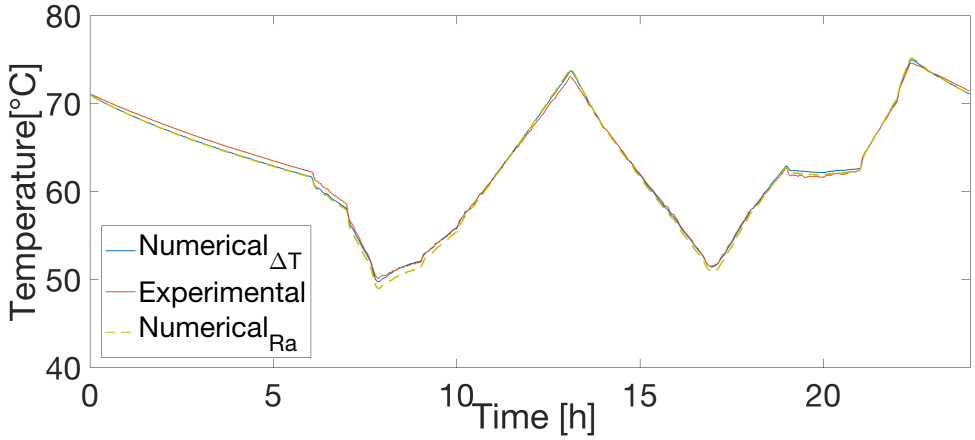

Figure 7.9. Numerical and experimental outlet temperature of the discharge coil

	MBE[$°C$]	RMSE[$°C$]	R2 [%]
Mean tank temperature	-0.57	1.6849	90.47
$T_{out,u}$	-0.2877	0.516	99.41
$T_{out,g}$	-0.0488	0.3528	99.83

Table 7.5. Mean bias error, root mean square error and determination coefficient relative to the temperatures in the coils and in the tank according to the second correlation

	MBE[W]	R2[%]
Tank energy variation	-40.39	89.48
Q_{user}	-66.99	96.77
Q_{charge}	339.70	97.47

Table 7.6. Mean bias error and determination coefficient relative to the energy variation in the tank and to the heat exchanged in the coils according to the correlation dependent only on temperature difference

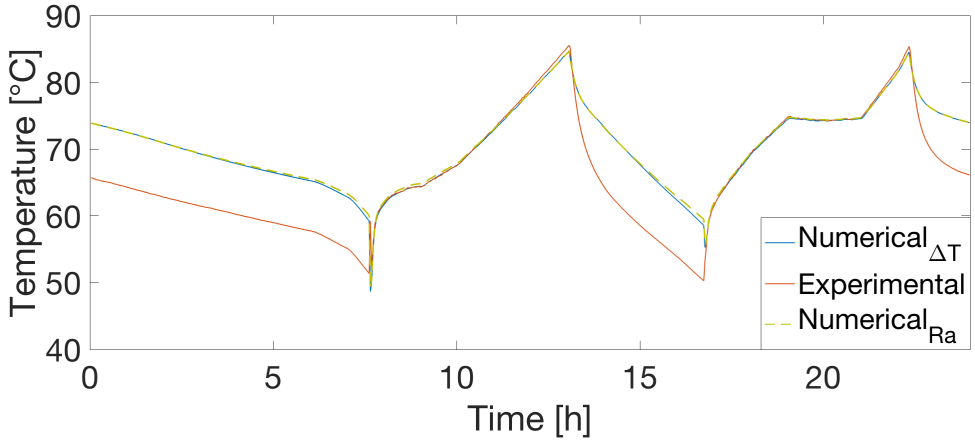

Figure 7.10. Numerical and experimental outlet temperature of the charge coil

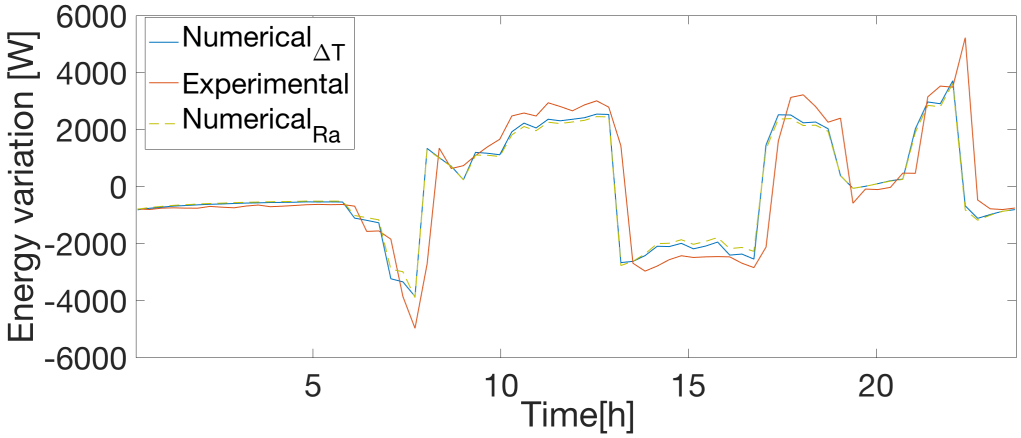

Figure 7.11. Numerical and experimental energy variation inside the water tank

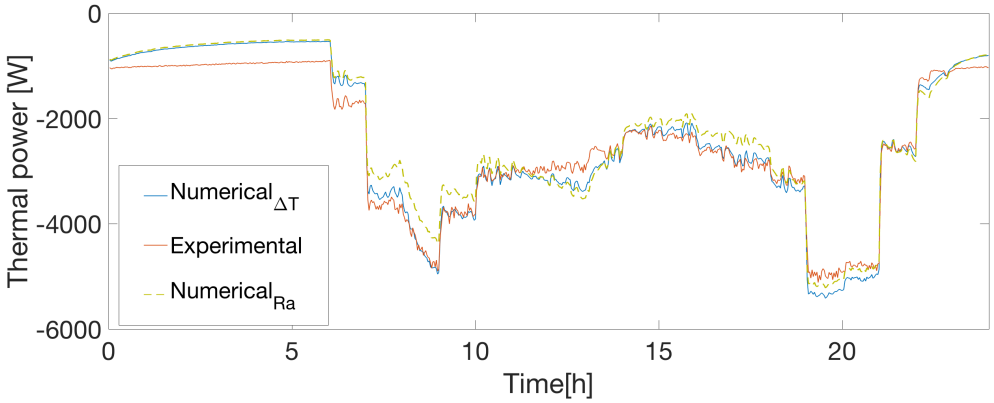

Figure 7.12. Numerical and experimental heat exchanged in the discharge coil

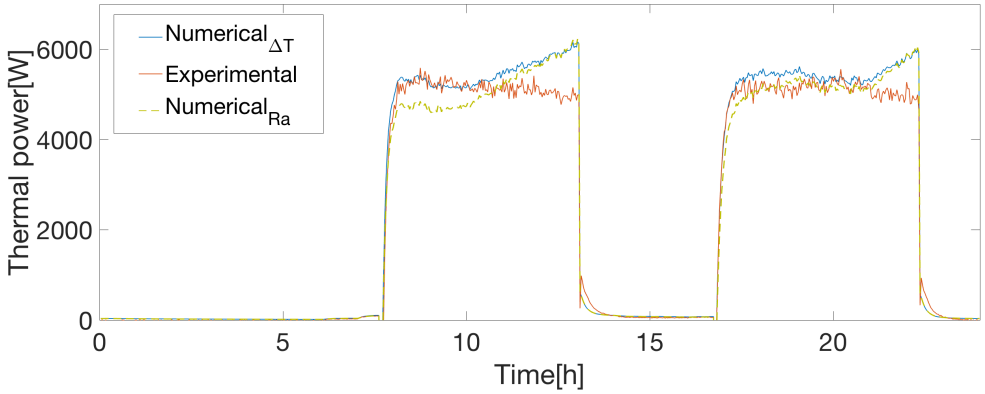

Figure 7.13. Numerical and experimental heat exchanged in the charge coil

	MBE[W]	R2[%]
Tank energy variation	-43.48	88.3
Q_{user}	195.84	92.88
Q_{charge}	60.26	97.15

Table 7.7. Mean bias error and determination coefficient relative to the energy variation in the tank and to the heat exchanged in the coils according to the correlation dependent on Rayleigh number

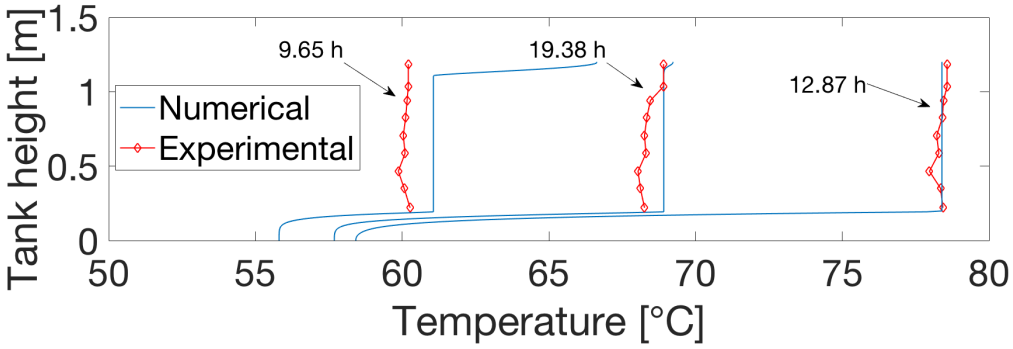

Figure 7.14. Thermal profiles of the water in the tank at three different instants

Chapter 8

Model of a commercial hot water tank storage filled with macro-encapsulated PCM

Due to the large latent heat, phase change materials could be used to increase the storage capacity of an existing hot water tank, without changing its size. In the previous chapter, the water tank had a temperature varying between 60 and 80 degrees, which means that with a volume of water of 400 lt, its capacity is about 9.3 kWh. If 100 lt of water are substituted with 100 aluminium bottles partially filled with 764 g of the PCM of chapter 5, the capacity could increase theoretically up to 32%. A higher capacity could bring benefits like satisfying the demand with a smaller heater and smaller number of daily on-off of the heating circuit. For the design and the optimization of an hybrid water-PCM storage, it could be useful to have a numerical model that simulates these kind of systems. In this chapter it is presented an experimental test and a model of a commercial hot water tank integrated with macro-encapsulated PCM. The tank is the same one with two immersed coils of the previous chapter. This model is therefore obtained by coupling the model that simulates the water tank in chapter 7 and the model of chapter 5 that simulates the single bottle of PCM.

8.1 Experimental test

The commercial hot water tank storage of 400 lt was filled with 94 bottles, each one containing 764 g of PCM having a phase change temperature of $68°C$, as it is shown in Figure 8.1. As a consequence 94 lt are occupied by the bottles, while water fills the remaining 306 lt. The whole tank is firstly taken at a temperature of $80°C$ in order to be sure that the all the PCM is initially liquid. After that, the experiment begins. The load curve is the same of chapter 7, so it refers to a semi-detached house of 100 m^2. The experiment is three days long and the results are shown in Figures 8.3-8.8. The resulting capacity of the storage seems to be smaller than in the case without phase change materials, since the electrical heater is turned on three times per day. This is due to a not complete melting-solidification of the PCM in the bottles,which means that less latent heat is available to the storage.

Figure 8.1. Top view of the tank integrated with macro-encapsulated PCM

8.2 Implementation of the model

The discretization of the tank is almost identical to the previous cases, but it differs in the volume occupied by the water. The discretization length of the tank is fixed to 1 cm, so the whole tank is characterized by 121 nodes. The 94 bottles are supposed to be perfect cylinders and to be placed vertically and homogeneously distributed along seven adjacent layers of the tank. Each bottle is 16 cm high, therefore each tank layer is characterised by 16 nodes. The heat transfer term between the PCM and the water is included in the equations for the tank model and it is equal to:

$$Q_{PCM-w} = h_{PCM-w} * A_{PCM} * (T_{PCM} - T_{water}) \tag{8.1}$$

where h_{PCM-w} is the heat transfer coefficient between the water and the bottle, A_{PCM} is the heat exchange area between the bottle and the PCM. T_{PCM} is the average surface temperature of the PCM unit. The heat transfer area takes into account the fact that the bottom surface is not adiabatic and that the effective height of bottle occupied by the PCM is lower than the height of the bottle. The heat transfer coefficient h_{PCM-w} is computed with the Churchill and Chu correlation for natural convection on a vertical wall [45]:

$$h_{PCM-w} = \frac{\lambda}{L}\left(0.825 + \frac{0.387 * Ra_L^{1/6}}{(1 + (0.492/Pr)^{9/16})^{8/27}}\right)^2 \tag{8.2}$$

where λ is the thermal conductivity of water, L is the height of a single bottle, Ra_L is the Rayleigh number referring to the height of the bottle and Pr is the Prandtl number. The reversion elimination algorithm in this case must consider that the volumes of the tank are not all equal, so it is slightly modified and a weighted average temperature is computed, rather than an arithmetical average. The top and bottom surfaces of the tank are considered adiabatic, while the lateral surface is subjected to natural convection with the ambient temperature,which is also in this case equal to $23°C$. Concerning the coils, the outlet sections are considered adiabatic, while to the inlet section Dirichlet time-dependent boundary conditions are applied. The temperature in these sections is the experimental one measured by the thermocouples. The Comsol model is almost the same of chapter 5, but differs in the boundary and initial conditions. The initial temperature in this case is equal to the initial tank temperature, while the heat transfer coefficient is imported from Matlab, but it is increased to balance the fact that in Comsol the bottom surface is considered as adiabatic,while in the reality it is not. Since only the bottom region of the tank is subjected to thermocline, the seven layers of bottles are modelled all together with a single simulation by considering the mean temperature of water along these layers.

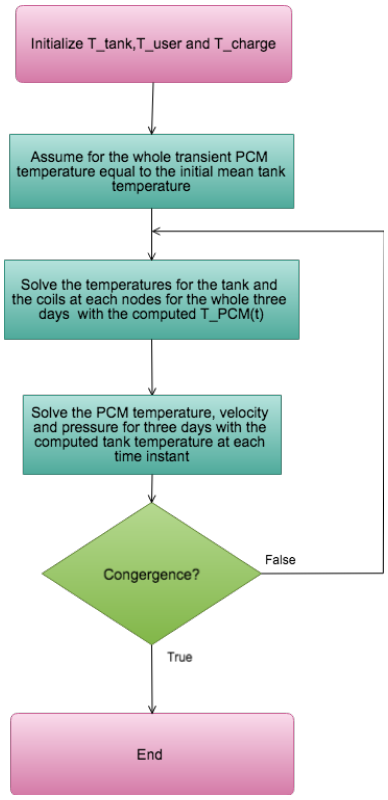

Figure 8.2. Flow diagram of the algorithm that couples the two models

The models are coupled with the approach explained in the flow diagram of Figure 8.2: This approach is computationally less expensive than a coupling made on the time-steps. In fact, the convergence is reached after only few iterations.

8.2.1 Results

Figures 8.3 and 8.4 show the numerical and experimental outlet temperature of the HTF in the charge and discharge coils. The curves are very similar for all the three days of simulation. In particular, the curves for the user coil appear almost overlapped. The numerical results regarding the outlet section of the charge coil are also very close to the experimental ones, except for the hours when the heating circuit is off. As it was already mentioned in the previous chapter, the results during these periods are too much influenced by the outdoor temperature. However,since the thermal power exchanged in the charge coil is so small during these periods, they are not worth being considered. Figure 8.5 shows the mean tank temperature during the three days according to experimental and numerical results. The numerical curve is very close to the experimental one, except from the night hours, when the heat transfer is lower. What is more for temperatures lower than $60°C$, the accuracy is lower, probably due to the correlation used for the heat transfer in the user coil, which is valid mostly at around 70°. However the mean square error is slightly larger than $1°C$ and the determination coefficient is larger than 90%, so the model overall predicts quite well all the temperatures. The statistics for the outlet sections of the coils and for the mean tank temperature are summarized in Table 8.1, which confirm the accuracy visible from the plots.
Concerning the thermal power exchanged in the coils, Figures 8.6 and 8.7 show the comparison

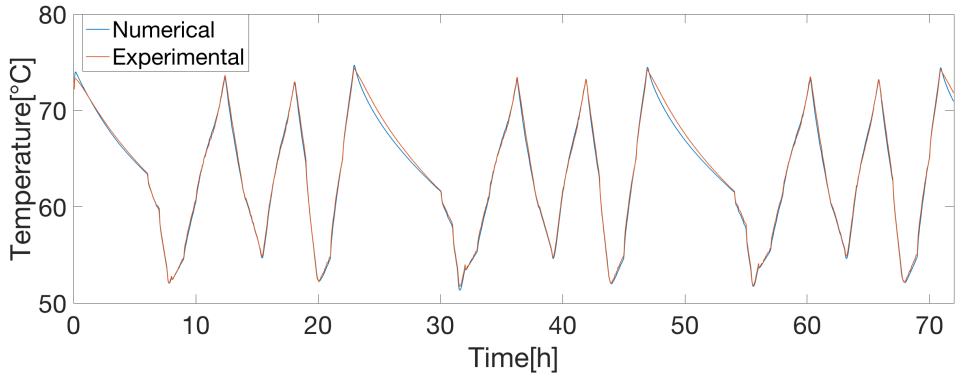

Figure 8.3. Outlet temperature of the discharge coil: Numerical vs Experimental

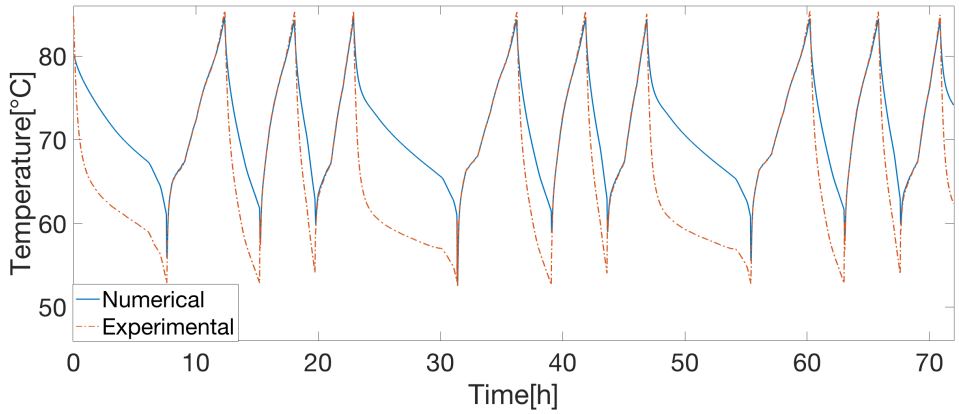

Figure 8.4. Outlet temperature of the charge coil: Numerical vs Experimental

between the numerical and experimental results. The behaviour of the curves is similar, with few differences in some particular periods. Regarding the power exchanged in the discharge coil, the numerical curve is very close to the experimental one, except some differences. In particular the model tends to underestimate the power exchanged in the user coil during the night. The numerical thermal power exchanged in the charge coil is sensibly larger than the experimental one in the afternoon hours. The general profile of the curve, however is still very similar to the experimental one, as it is also confirmed by the statistics in Table 8.2. In Figure 8.8 the numerical curve relative to the tank energy variation follows the same behaviour of the experimental one, but the differences are larger in the peaks. However, the determination coefficient for the energy variation in the tank is about 92%, which is synonym of a good correlation between the numerical and the experimental results.

Figure 8.9 shows the volume liquid fraction variation of the PCM in the three days. These data are only extracted from the simulations, since there was no way to compute the liquid fraction experimentally. At the beginning of the experiment the PCM is all melted and each day is subjected to three cycles of charge and discharge. At the end of each of these cycles, the PCM is never completely solidified or melted.This is mainly due to an insufficient heat transfer between the water and the PCM. What is more the system after three days of activity did not reach a complete

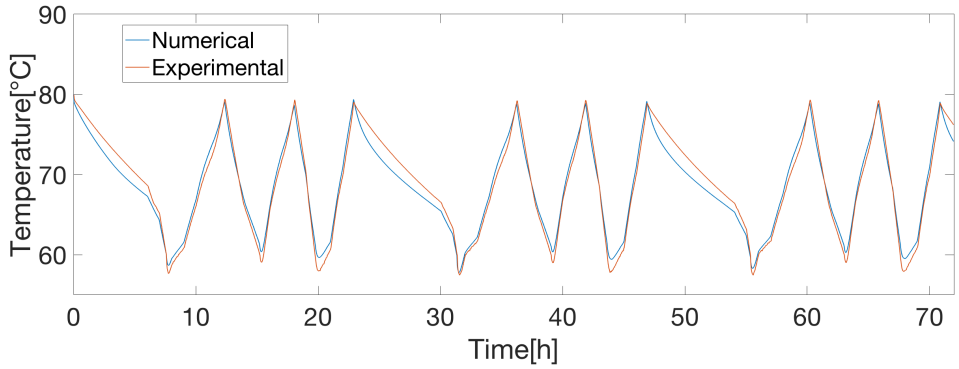

Figure 8.5. Water tank mean temperature: Numerical vs Experimental

	MBE[$°C$]	RMSE[$°C$]	R2 [%]
Mean tank temperature	-0.2089	1.21	95.21
$T_{out,u}$	-0.2309	0.3835	99.61
$T_{out,g}$	-0.0822	0.3646	99.80

Table 8.1. Statistics for the temperature in the tank and in the outlet sections

periodicity, since between the second and the third day there is still a difference of about 5% of liquid fraction. This happened because the initial condition of uniform temperature equal to $80°C$ is too far from the periodic working conditions,therefore more cycles are needed to reach daily periodicity of the results. This is also visible from Figure 8.10, that shows the energy variation of the PCM modules.

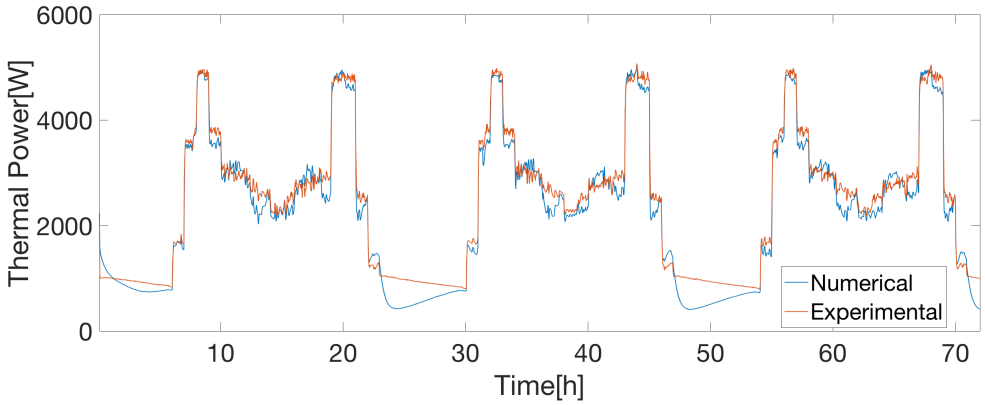

Figure 8.6. Thermal power exchanged between the discharge coil and the water tank

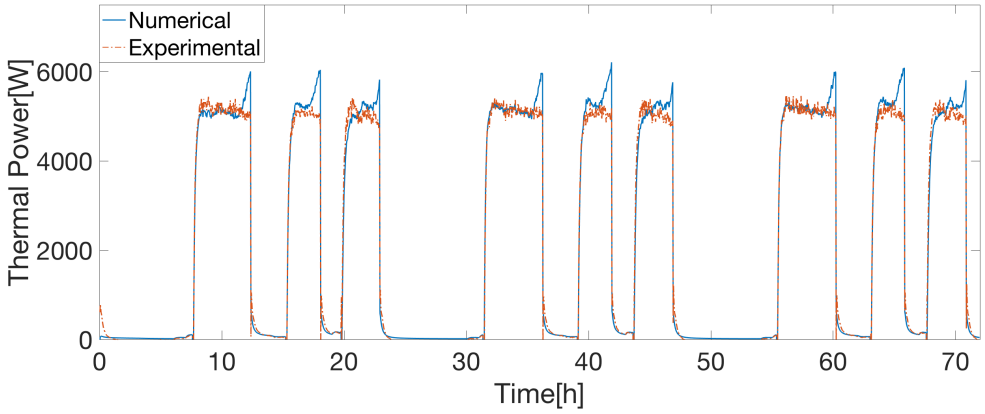

Figure 8.7. Thermal power exchanged between the charge coil and the water tank

Figure 8.11 shows the thermal energy stored or released by the PCM at each hour. Since periodicity of the results is not reached yet, the total daily energy released/stored by the PCM during the third day is not equal to zero, but the released energy is larger than the stored one. The thermal profiles of the PCM modules at four different instants are shown in Figure 8.12. These time instances correspond to relative maximum or minimum points on the liquid fraction curves. The division between the two phases is visible and in each of the plots the PCM is far from being fully solid or fully liquid, as Figure 8.9 pointed out.

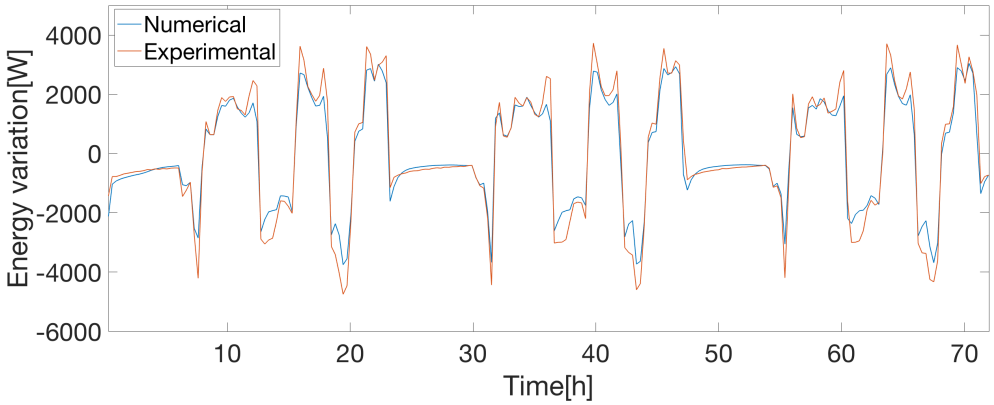

Figure 8.8. Water tank energy variation: Numerical vs Experimental

	MBE[W]	R2[%]
Tank energy variation	-11.68	92.19
Q_{user}	-155.48	96.38
Q_{charge}	130.82	96.72

Table 8.2. Statistics relative to the thermal power exchanged and the energy variation in the tank

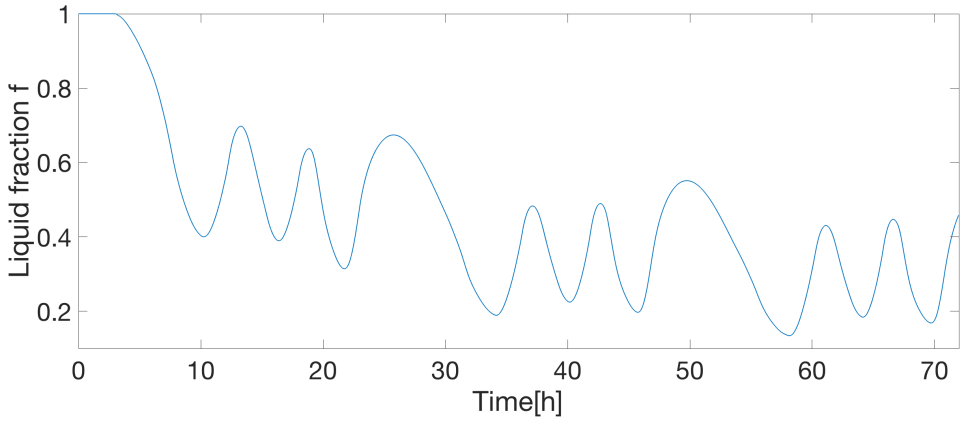

Figure 8.9. Liquid fraction of the whole PCM

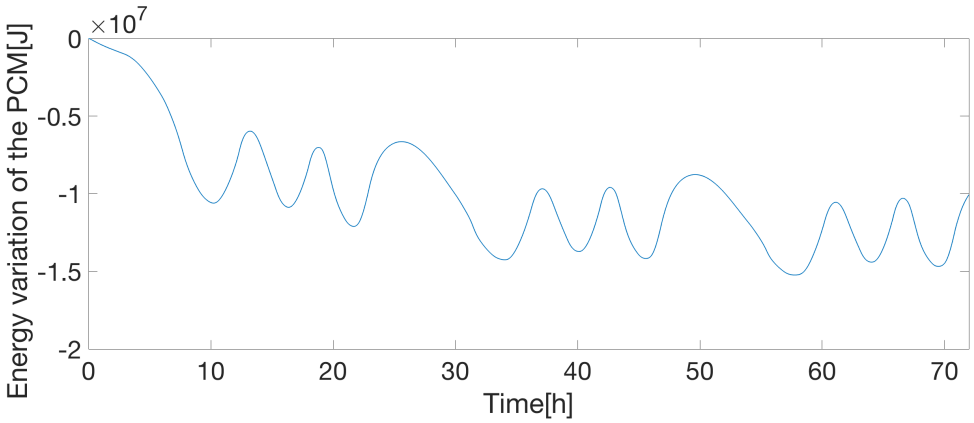

Figure 8.10. Total energy released by the PCM

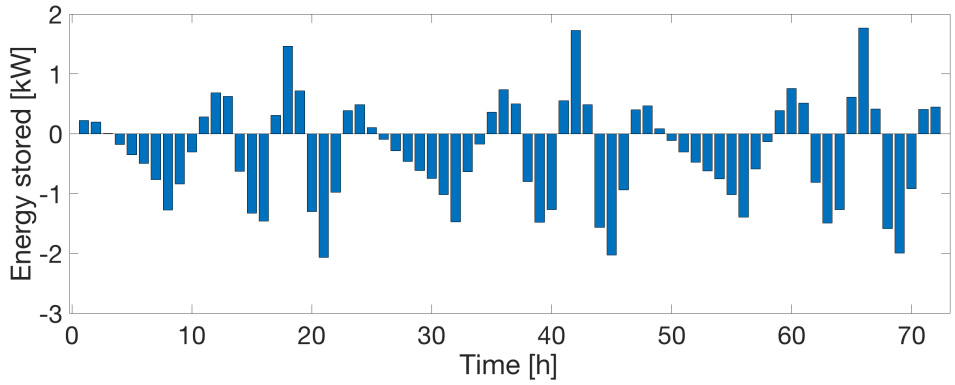

Figure 8.11. Energy stored each hour by the PCM

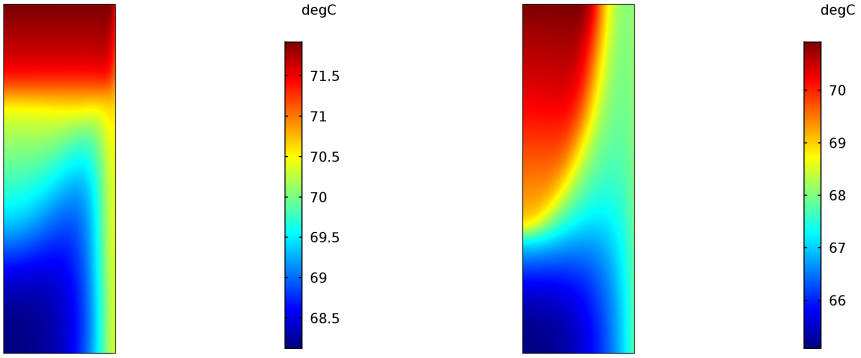

(a) 50 h (b) 58 h

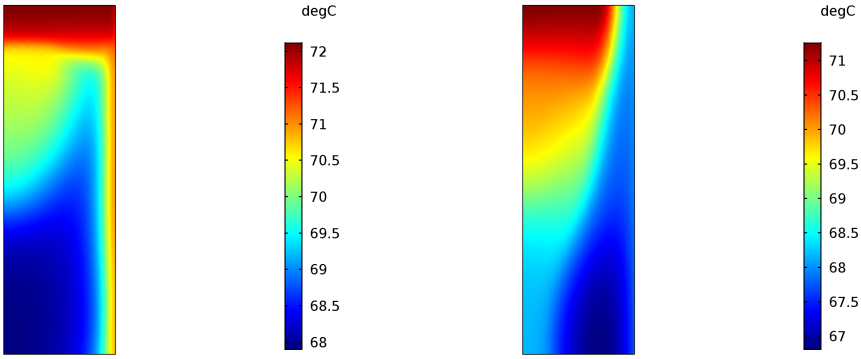

(c) 61 h (d) 64 h

Figure 8.12. Temperature profile of the PCM at four different instants

Chapter 9

Conclusions

In this thesis various methods for the modelling of phase change have been tested. The arbitrary Lagrangian-Eulerian method showed its limits due to the implementation difficulties and the impossibility of simulating complete melting/solidification of a whole geometry. Concerning the two enthalpy methods, they both presented good results for the solidification, but the apparent viscosity modelled with good accuracy also the melting phase. As a consequence, the modules of PCM to be integrated into the water tank have been modelled with the apparent viscosity method. What is more a sensitivity analysis on the empirical parameters that characterize this method. A large mushy zone temperature interval showed a phase change far from being isothermal and smoother temporal temperature curves in the zones close to the phase change temperature. On the contrary with smaller values of ΔT the curve tends to be horizontal at the phase change temperature, but it is sharper for temperatures close to the mushy zone. The temperature interval together with the mushy zone constant has an impact on the natural convection. In particular, larger values of mushy zone constant are responsible for weaker convection. Over a certain value there is not difference, because the model will tend to the pure conductive one. Due to the different kinetic phenomena in solidification and melting, the values of the empirical parameters differ from charge to discharge. However a trade-off set of parameters can be found and used to simulate an entire cycle of charge/discharge. Concerning the water tank model, needed to build the model of the hybrid PCM-water thermal storage, it has been validated through experimental data, showing accurate results for the outlet sections of the coils, but slight smaller accuracy for the mean temperature in the water tank. The reason is mainly due to small temperature difference between the inlet and outlet sections, which is of the order of few degrees. The maximum error of the thermocouples is of the order of one degree, therefore there is too much uncertainty on the experimental results. The model however showed good statistics and agreement with the experimental data. Lastly, the tank was integrated with 94 modules of PCM and the behaviour of this hybrid storage was tested for three days. The thermal capacity of the storage seemed to be decreased with respect to the case without PCM, due to the poor heat transfer properties of the material that did not let the PCM melt or solidify completely. The experiment was also simulated through a coupling of the models for the water tank and the PCM modules. The statistics showed a good agreement between the experimental and the numerical results, therefore the model can be considered validated and the main aim of this thesis is achieved. However the research about this system will not stop, because some techniques to enhance the heat transfer between water and PCM must be studied. One way would be increasing the heat transfer area/volume ratio of the PCM modules by reducing the diameter or by adding internal fins. The first technique is cheaper and more practical and the validated numerical model can be used to simulate smaller bottles before realizing new expensive

experiments. Therefore next step is to find a thermodynamic convenience of this system by reducing the diameter of the modules. After that, an economic analysis will be necessary to study the feasibility of such system to compute the payback time and to compare the cost to the one of an equivalent storage, but characterised by only sensible heat and therefore of bigger volume.

Bibliography

[1] Marcel Lacroix. Study of the heat transfer behavior of a latent heat thermal energy storage unit with a finned tube. *International Journal of Heat and Mass Transfer*, 36(8):2083 – 2092, 1993.

[2] Lei Yang and Xiao-song Zhang. Performance of a new packed bed using stratified phase change capsules. *International Journal of Low-Carbon Technologies*, 7(3):208–214, 2012.

[3] John Crepeau and Ali Siahpush. Approximate solutions to the stefan problem with internal heat generation. *Heat and Mass Transfer*, 44:787–794, 2008.

[4] A. Felix Regin, S.C. Solanki, and J.S. Saini. Heat transfer characteristics of thermal energy storage system using pcm capsules: A review. *Renewable and Sustainable Energy Reviews*, 12(9):2438 – 2458, 2008.

[5] Atul Sharma, V Veer Tyagi, CR Chen, and Dharam Buddhi. Review on thermal energy storage with phase change materials and applications. *Renewable and Sustainable energy reviews*, 13(2):318–345, 2009.

[6] C.E. Andraka, A.M. Kruizenga, B.A. Hernandez-Sanchez, and E.N. Coker. Metallic phase change material thermal storage for dish stirling. *Energy Procedia*, 69:726 – 736, 2015. International Conference on Concentrating Solar Power and Chemical Energy Systems, SolarPACES 2014.

[7] B Muñoz-Sánchez, Iñigo Iparraguirre-Torres, V Madina-Arrese, U Izagirre-Etxeberria, A Unzurrunzaga-Iturbe, and A García-Romero. Encapsulated high temperature pcm as active filler material in a thermocline-based thermal storage system. *Energy Procedia*, 69:937–946, 2015.

[8] Weiguang Su, Jo Darkwa, Georgios Kokogiannakis, Tongyu Zhou, and Yiling Li. Preparation of microencapsulated phase change materials (mepcm) for thermal energy storage. *Energy Procedia*, 121:95 – 101, 2017. Improving Residential Energy Efficiency International Conference, IREE 2017.

[9] J Stefan. Uber einge problem der theoric der warmeleitung, sb wein. *Acad. Mat. Natur*, 98:173–484, 1989.

[10] AC Boucíguez, RF Lozano, and MA Lara. About the exact solution in two-phase stefan problem. *Thermal Engineering*, 6(2):70–75, 2007.

[11] JA Mackenzie and ML Robertson. The numerical solution of one-dimensional phase change problems using an adaptive moving mesh method. *Journal of computational Physics*, 161(2):537–557, 2000.

[12] J Caldwell and YY Kwan. Starting solutions for the boundary immobilization method. *Communications in numerical methods in engineering*, 21(6):289–295, 2005.

[13] Nacer Sadoun, El-Khider Si-Ahmed, Pierre Colinet, and Jack Legrand. On the boundary immobilization and variable space grid methods for transient heat conduction problems with phase change: Discussion and refinement. *Comptes Rendus Mécanique*, 340(7):501–511, 2012.

[14] James Caldwell and Yuen-Yick Kwan. A brief review of several numerical methods for one-dimensional stefan problems. *Thermal science*, 13(2):61–72, 2009.

[15] J Crank. Two methods for the numerical solution of moving-boundary problems in diffusion and heat flow. *The Quarterly Journal of Mechanics and Applied Mathematics*, 10(2):220–231, 1957.

[16] V. Kumar, F. Durst, and S. Ray. Modeling moving-boundary problems of solidification and melting adopting an arbitrary lagrangian-eulerian approach. *Numerical Heat Transfer, Part B: Fundamentals*, 49(4):299–331, 2006.

[17] Comsol reference manual.

[18] John Crank. *Free and moving boundary problems*. Oxford University Press, 1987.

[19] Saleh Nasser AL-Saadi and Zhiqiang (John) Zhai. Modeling phase change materials embedded in building enclosure: A review. *Renewable and Sustainable Energy Reviews*, 21:659 – 673, 2013.

[20] A Andreozzi, F Ascione, A Bianco, M Caliano, and M Iasiello. Studio e individuazione di soluzioni tecniche per il miglioramento della trasmissione del calore in sistemi di accumulo termico basati sui materiali a cambiamento di fase (pcm) nell'ambito dell'accumulo del freddo. Technical report, University of Naples "Federico II", 2016.

[21] Lubomir Klimes, Pavel Charvat, and Milan Ostry. Challenges in the computer modeling of phase change materials. *Materiali in tehnologije*, 46(4):335–338, 2012.

[22] CR Swaminathan and VR Voller. On the enthalpy method. *International Journal of Numerical Methods for Heat & Fluid Flow*, 3(3):233–244, 1993.

[23] VR Voller and CR Swaminathan. Eral source-based method for solidification phase change. *Numerical Heat Transfer, Part B Fundamentals*, 19(2):175–189, 1991.

[24] M Cross, S Johnson, and P Chow. Mapping enthalpy-based solidification algorithms onto vector and parallel architectures. *Applied mathematical modelling*, 13(12):702–709, 1989.

[25] Comini Bonacina, G Comini, A Fasano, and M 1973 Primicerio. Numerical solution of phase-change problems. *International Journal of Heat and Mass Transfer*, 16(10):1825–1832, 1973.

[26] Minwu Yao and Anion Chait. An alternative formulation of the apparent heat capacity method for phase-change problems. *Numerical Heat Transfer, Part B Fundamentals*, 24(3):279–300, 1993.

[27] Faruk Civan. Limitation in the apparent heat capacity formulation for heat transfer with phase change. In *Proceedings of the Oklahoma Academy of Science*, volume 67, pages 83–88, 1987.

[28] Mohamad Muhieddine, Edouard Canot, and Ramiro March. Various approaches for solving problems in heat conduction with phase change. *International Journal on Finite Volumes*, page 19, 2009.

[29] EC Lemmon. Phase-change techniques for finite element conduction codes. Technical report, Idaho National Engineering Lab., Idaho Falls (USA), 1979.

[30] K Morgan et al. An improved algorithm for heat conduction problems with phase change, internat. *J. Numer. Meths, Engrg*, 12, 1978.

[31] V R Voller and C Prakash. A fixed grid numerical modeling methodology for convection diffusion mushy region phase-change problem. *International Journal Heat Mass Transfer*, 30(9):1709–1719, 1987.

[32] A. D. Brent, V. R. Voller, and K. J. Reid. Enthalpy-porosity technique for modeling convection-diffusion phase change: Application to the melting of a pure metal. *Numerical Heat Transfer*, 13(3):297–318, Apr 1988.

[33] Gunduz Caginalp and Xinfu Chen. Phase field equations in the singular limit of sharp interface problems. In Morton E. Gurtin and Geoffrey B. McFadden, editors, *On the Evolution of Phase Boundaries*, pages 1–27, New York, NY, 1992. Springer New York.

[34] Y. Zhao, C.Y. Zhao, and Z.G. Xu. Numerical study of solid-liquid phase change by phase field method. *Computers and Fluids*, 164:94 – 101, 2018. Special Issue devoted to The Asian

Symposium on Computational Heat Transfer and Fluid Flow 2015 (ASCHT 2015) held in Busan, Korean on November 22-25, 2015.

[35] Alvaro de Gracia and Luisa F Cabeza. Numerical simulation of a pcm packed bed system: a review. *Renewable and Sustainable Energy Reviews*, 69:1055–1063, 2017.

[36] K.A.R. Ismail and R. Stuginsky Jr. A parametric study on possible fixed bed models for pcm and sensible heat storage. *Applied Thermal Engineering*, 19(7):757 – 788, 1999.

[37] Luigi Mongibello, Nicola Bianco, Martina Caliano, and Giorgio Graditi. Numerical simulation of an aluminum container including a phase change material for cooling energy storage. *Applied System Innovation*, 1(3):34, 2018.

[38] Hans Dieter Baehr and Karl Stephan. *Heat and Mass Transfer*, volume 6. Springer, 1994.

[39] Luigi Mongibello, Nicola Bianco, Marialaura Di Somma, and Giorgio Graditi. Experimental validation of a tool for the numerical simulation of a commercial hot water storage tank. *Energy Procedia*, 105:4266–4273, 2017.

[40] V Gnielinski. Heat transfer and pressure drop in helically coiled tubes. *Heat Transfer, Proceedings of the International Heat Transfer Conference*, 6:2847–2854, 01 1986.

[41] Mohamed E Ali. Free convection heat transfer from the outer surface of vertically oriented helical coils in glycerol-water solution. *Heat and mass transfer*, 40(8):615–620, 2004.

[42] Devanahalli G Prabhanjan, Timothy J Rennie, and GS Vijaya Raghavan. Natural convection heat transfer from helical coiled tubes. *International Journal of Thermal Sciences*, 43(4):359–365, 2004.

[43] J. Cadafalch, D. Carbonell, R. Consul, and R. Ruiz. Modelling of storage tanks with immersed heat exchangers. *Solar Energy*, 112:154 – 162, 2015.

[44] D.W Mather, K.G.T Hollands, and J.L Wright. Single- and multi-tank energy storage for solar heating systems: fundamentals. *Solar Energy*, 73(1):3 – 13, 2002.

[45] Stuart W. Churchill and Humbert H.S. Chu. Correlating equations for laminar and turbulent free convection from a vertical plate. *International Journal of Heat and Mass Transfer*, 18(11):1323 – 1329, 1975.